Convectively Generated Gravity Waves and Convective Aggregation in Numerical Models of Tropical Dynamics
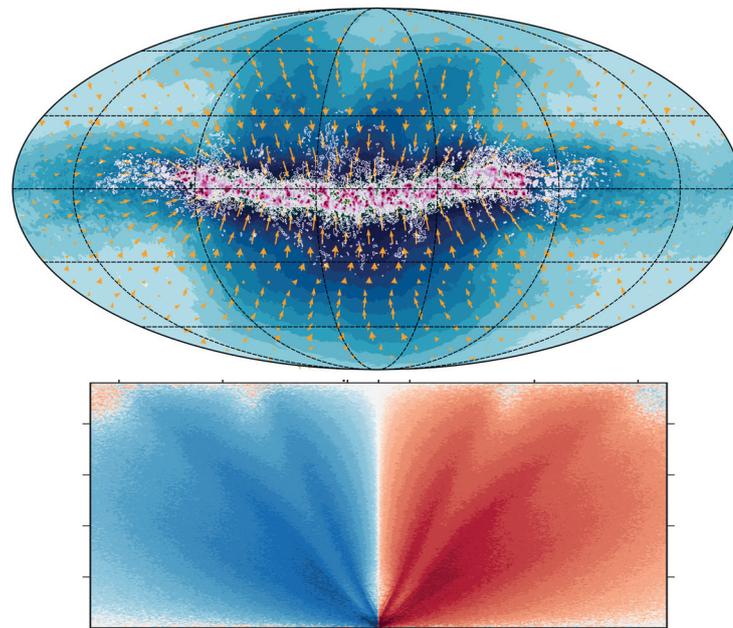

Sebastian Karl Müller

Hamburg 2019

Convectively Generated Gravity Waves and Convective Aggregation in Numerical Models of Tropical Dynamics

Sebastian Karl Müller

Hamburg 2019

Sebastian Karl Müller

Max-Planck-Institut für Meteorologie
The International Max Planck Research School on Earth System Modelling
(IMPRS-ESM)
Bundesstrasse 53
20146 Hamburg

Universität Hamburg
Geowissenschaften
Meteorologisches Institut
Bundesstr. 55
20146 Hamburg

Tag der Disputation: 16.11.2018

Folgende Gutachter empfehlen die Annahme der Dissertation:

Prof. Dr. Stefan Bühler
Dr. Elisa Manzini

Abstract

In this dissertation I investigate two phenomena, which both arise from atmospheric moist convection: on the one hand, the gravity waves emanated from convection and on the other hand convective aggregation.

Convectively generated gravity waves are investigated on novel spatial and temporal scales. We use numerical models that display the transition of global climate modeling from coarse grids, at which convection and gravity waves are parameterized, towards finer resolutions, where both are treated explicitly. Gravity waves generated by deep, tropical convection are examined by means of spectral analysis. We make use of the models' different setups to discuss the impacts of spatial resolution, the treatment of moist convection and the complexity of boundary conditions, on convectively generated gravity waves.

We find that in the stratosphere substantially more gravity wave momentum flux is resolved by models with fine horizontal grid spacing, as the spectral slope is almost flat in zonal wavenumber space ($\sim k^{-1}$), until scales at which numerical diffusion sets in. However we also find that, when a well-organized tropical storm system of large scale, is simulated with convection permitting resolution, the gravity wave variance may be enhanced at scales up to 250 km and the spectral slope may be even flatter. We find an explanation for this in the representation of dynamical overshooting of convective updrafts that is expected to mechanically generate gravity waves.

Further we find that a parameterization of convection drastically reduces gravity wave momentum flux associated with tropical convection, as deep modes of latent heating and gravity waves are underestimated. Thus its application is expected to have consequences for wave mean-flow interaction in the middle atmosphere and so an additional parameterization of gravity wave drag is required.

Spectra in zonal wavenumber, vertical wavenumber and frequency space reveal the universal properties of the gravity wave spectrum in the middle atmosphere. These are successfully reproduced in realistic simulations of tropical dynamics.

Convective aggregation is studied in novel boundary conditions. We use a convection permitting model of radiative convective equilibrium on a spherical domain and impose sea surface temperature (SST) profiles that are characterized by a meridional gradient and zonal symmetry. With this experimental design we allow for convective aggregation to occur both as a result of the forcing through the SST gradient as well as through

convective self-aggregation.

We study the sensitivity of the convective evolution and aggregation to the steepness of the SST gradient: we find that the steeper the gradient the more stable is the convergence line, that manifests in convection along the model's equator, where SSTs peak, and the longer it takes for zonal self-aggregation to occur. However, as soon as the convergence line breaks and a strong enough zonal circulation develops, zonal self-aggregation occurs. The cloud cluster then contracts rapidly and this process occurs equally rapid for the differently steep SST gradients studied.

The emerging cloud clusters are zonally elongated and in that property they are different to the radially symmetric cloud clusters seen in traditional RCE studies of self-aggregation. By this asymmetry these cloud clusters force a more complex circulation pattern, by which the environment is affected. The shallow circulation is found to export moisture from the cloud cluster to the originally dry polar regions. By that a shortcoming of traditional RCE studies, too dry non-convecting regions, is overcome. We find that the shallow moist outflow only occurs in the meridional dimension, at the elongated side of the cluster, above cool SSTs. The zonal low-level inflow at the equator is deeper and shows no shallow outflow. Eventually here the moisture that was exported is recycled into the cluster, as the meridional flow crosses the pole and reaches back to the equator. As of this we draw analogies to atmospheric rivers.

Zusammenfassung

In der vorliegenden Dissertation erforsche ich zwei Phänomene, die beide ihren Ursprung in feuchter atmosphärischer Konvektion haben: einerseits, Schwerewellen, die durch Konvektion erzeugt werden, und andererseits, konvektive Aggregation.

Konvektiv generierte Schwerewellen werden auf neuartigen räumlichen und zeitlichen Skalen erforscht. Wir verwenden numerische Modelle die den Übergang globaler Klimamodelle von groben Gittern, für welche Konvektion und Schwerewellen parameterisiert werden, hin zu feinen Gittern, bei denen beide Prozesse expizit dargestellt werden, abbilden. Ich untersuche die von tiefer, tropischer Konvektion ausgelöste Schwerewellen mit Analysen im spektralen Raum. Wir nutzen die spezifischen Unterschiede der Modelle um die Auswirkungen von räumlicher Auflösung, der Darstellung von feuchter Konvektion und der Komplexität von Randbedingung auf konvektiv generierte Schwerewellen zu untersuchen.

Wir zeigen, dass in der Stratosphäre substanziell mehr Schwerewellen-Impulsfluss von Modellen mit feinem Gitterabstand aufgelöst wird, weil die Steigung im horizontalen Wellenzahl-Raum gering ist ($\sim k^{-1}$), bis hin zu Skalen bei denen die numerische Diffusion einsetzt. Zudem beobachten wir dass, wenn ein stark organisiertes, groß-skaliges tropisches Sturmsystem auf einem Konvektion auflösenden Gitter simuliert wird, Schwerewellen mit Skalen bis 250 km verstärkt auftreten und die Steigung sogar noch flacher sein kann. Eine Erklärung dafür finden wir in der ermöglichten Darstellung von überschießenden Wolkenobergrenzen, womit die mechanische Auslösung von Schwerewellen zu erwarten ist.

Im weiteren zeigt sich, dass die Verwendung einer Parametrisierung von Konvektion den Schwerewellen-Impulsfluss stark reduziert, da tiefe Moden von latenter Wärme unterrepräsentiert und damit tiefe Moden von Schwerewellen fehlen. Deswegen muss erwartet werden, dass ihre Anwendung Auswirkungen auf die Wechselwirkung von Wellen und Zirkulation hat und somit ist dann eine zusätzliche Parametrisierung von Schwerewellen notwendig.

In Spektren im horizontalen und vertikalen Wellenzahl-Raum, und im Frequenz-Raum, zeigen sich die universellen Eigenschaften des Schwerwellenspektrums der mittleren Atmosphäre. Diese werden in den untersuchten Modellen, die Konvektion explizit darstellen, erfüllt.

Konvektive Aggregation erforsche ich in neuartigen Randbedingungen. Ich verwende ein Konvektion auflösendes Modell in Strahlungs-Konvektions-Gleichgewicht (RCE) auf einem

sphärischen Gitter und untersuchen verschiedene Profile von Meeresoberflächentemperaturen (SSTs), die durch einen meridionalen Gradienten und zonale Symmetrie auszeichnen. Mit diesem experimentellen Aufbau erlauben wir, dass konvektive Aggregation sowohl als Folge des SST-Gradienten also auch durch Selbstaggregation, auftritt.

Wir untersuchen die Sensitivität der konvektiven Entwicklung und Aggregation hinsichtlich der Steigung des SST-Gradienten: wir zeigen dass ein stärkerer Gradient eine stabilere Konvergenzlinie bewirkt, die sich in Konvektion entlang des quators, wo SSTs maximal sind, manifestiert. Sobald jedoch die Konvergenzlinie aufbricht und eine ausreichend starke zonale Zirkulation sich entwickelt, setzt konvektive Selbt-Aggregation ein. Das System konvektiver Wolken zieht sich dabei rasch zusammen und wir beobachten, dass dieser Prozesse gleich schnell für unterschiedliche starke SST-Gradienten abläuft.

Die sich entwickelnde Anhäufung konvektiver Wolken ist verlängert in ihrer zonalen Ausdehnung und unterscheidet sich darin von radial symmetrischen Wolkenanhäufungen, wie sie in traditionallen Konvektion auflösenden RCE Studien von Selbst-Aggregation auftreten. Durch ihre Asymmetrie erzeugen die Wolkenanhäufungen eine komplexe Zirkulation, durch welche die großskalige Umgebung beeinflusst wird. Wir zeigen, dass die flache Teil der Zirkulation Feuchtigkeit aus dem Wolkensystem exportiert und in ursprünglich trockene, polare Regionen transportiert. Dadurch wird ein Manko traditioneller RCE Studien von Selbst-Aggregation, die zu trockenen wolkenfreien Regionen, überwunden. Wir zeigen, dass die feuchte Ausströmung ausschließlich in der meridionalen Dimension, entlang der verlängerten Seite der Wolkenanhäufung auftritt, und über kühleren SSTs, auftritt. Die zonale Anströmung ist tiefer und es tritt keine feuchte Ausströmung auf. Schließlich wird hier die exportierte Feuchtigkeit zurück in die Wolkenanhäufung geführt, da die meridionale Zirkulation die Pole umspannt und die äquatorialen Regionen wieder erreicht. Im weiteren diskutieren wir Analogien dieser Strömung zu Atmosphärischen Flüssen.

Contents

Contents

CHAPTER 1

INTRODUCTION

Atmospheric moist convection (Stevens, 2005) lies at the core of this dissertation and links two emerging phenomena that are specifically studied: firstly, gravity waves generated by convection in the tropics and secondly, convective aggregation. Clouds naturally illustrate moist convection, as seen in the photograph shown in Figure 1.1, and the appreciation of their beauty might come along with the fascination for their physics.

Within a convective cloud saturated moist air rises, as a response to a thermal instability of air mass in the planetary boundary layer with respect to the free troposphere. This ascending motion is driven by the buoyancy force, that is generated through the latent heat release during the phase changes of water vapor into liquid cloud droplets and cloud ice particles. By the presence of different phases of water and of latent heat moist convection is distinguished from dry convection, which mixes heat within the planetary boundary layer.

As a form of heat transfer convection plays, along with radiation, a central role in the fundamental tropical heat budget: radiative-convective equilibrium (RCE). In short, RCE describes the statistical equilibrium of convective heating and net radiative cooling of the atmosphere. The closely related circulation pattern is referred to as a thermally direct overturning circulation (Emanuel et al., 1994), meaning that air rises in convective plumes,

Figure 1.1.: Tropical convective cloud system composed of the three prevalent modes of convection (Johnson et al., 1999): shallow convective clouds, congestus and deep convection. The stratiform outflow below the tropopause forms an anvil cloud aloft the convection. Photo taken from the International Space Station at 2.2°S 122.6°E on 5th of December 2009.[1]

diverges below the tropopause and subsides over large areas. This system is schematically illustrated in Figure 1.2. The prime example of such a circulation is the Hadley Cell, which mediates the meridional heat and moisture transport in the tropics and leads us to one of the phenomena studied here, convective aggregation. The associated Intertropical Convergence Zone (ITCZ) constitutes a basic form of convective aggregation, meaning that convection is spatially organized to form large-scale clusters, as the line of convergence of trade winds and the peaks of sea surface temperatures (SSTs) control the location of convection.

As briefly introduced before, the response of a thermally unstable atmospheric layer to a perturbation is a flow in form of convection. In contrast to that, the response of a stably stratified atmosphere to a perturbation is gravity wave motion. One such perturbation may be the thermal and dynamical anomaly within a deep convective cloud, and the stably stratified atmosphere the stratosphere (and also the surrounding troposphere, which is only unstable with respect to an air parcel rising from the boundary layer). In fact, atmospheric moist convection is the primary source of atmospheric gravity waves in the tropics and these convectively generated gravity waves (CGGWs) contribute significantly to the stratospheric momentum budget (Fritts and Alexander, 2003). By that CGGWs have a major influence on wave-driven circulations, most prominently on the Quasi-Biennial

---

[1]to be found at `https://eol.jsc.nasa.gov/SearchPhotos/` using Photo-ID ISS022-E-6488. Downloaded in July 2018.
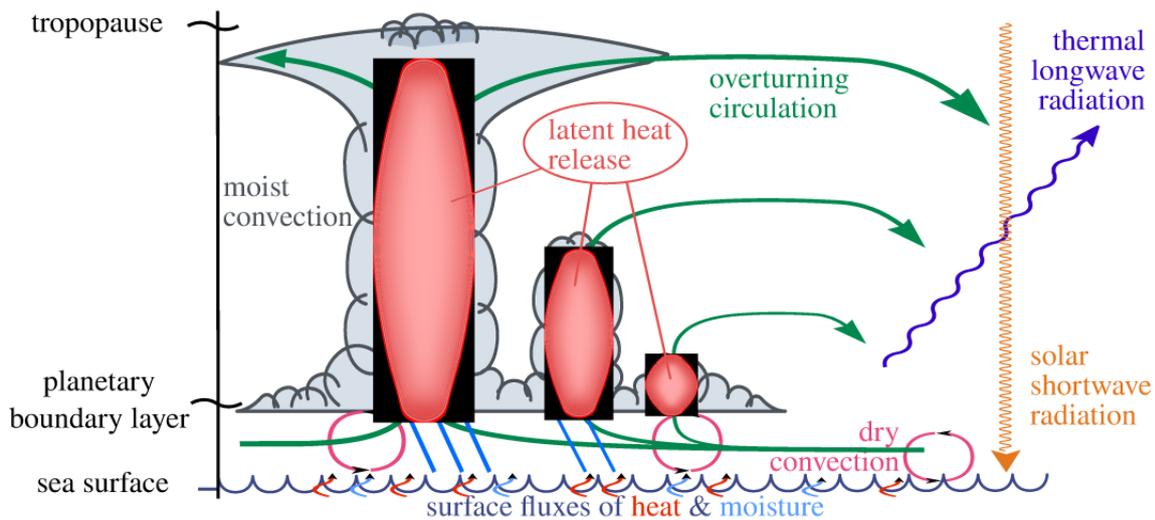
Figure 1.2.: Schematic of a thermally direct overturning circulation associated with RCE: Solar shortwave radiation is absorbed within the mixed layer of the ocean, while the free troposphere cools through the emission of thermal longwave radiation, thereby destabilizing with respect to the planetary boundary layer (PBL), where sensible and latent heat from the ocean is intruded into the atmosphere and mixed by dry convection. Moist convection then transports the latent heat from the PBL and releases it in the free troposphere. The associated overturning circulation comprises: boundary layer convergence, ascent in convective clouds, divergence below the tropopause or inversion layers, and subsidence over large-scale cloud-free areas. Inspired by Manabe and Strickler (1964) and Emanuel et al. (1994).

Oscillation (QBO).

As for moist convection, gravity wave motion in the troposphere may be visualized through clouds. The photograph in Figure 1.3 (a) shows a flow over islands, whose lifting effect excites gravity wave motion. The clouds seen as arcs on the lee side of the islands form at the waves' ridges. In the stratosphere polar stratospheric clouds, forming at extremely low temperatures ($<$-85$°C$) in the polar regions, can be observed at dusk or dawn, when only the middle atmosphere receives sunlight. They then may also visualize wave motion, as seen in Figure 1.3 (b).

The representation of atmospheric moist convection, gravity waves and convective aggregation, in numerical models requires high numerical resolution, which for large spatial and temporal scales comes along with high computational costs. Thus, for global circulation models (GCMs), as used for climate studies, and numerical weather prediction (NWP), parameterizations of these processes are still used, sacrificing on their underlying dynamical and physical complexity. For this dissertation I developed an idealized model of tropical dynamics and took advantage of a modern super-computer. With this I achieved to conduct simulations with an explicit representation of tropical convection, the gravity waves emanated, and convective aggregation, on spatial scales large enough to cover the scale of typical tropical circulation systems, and on temporal scales long enough to capture the temporal evolution of these systems.

(a):

(b):
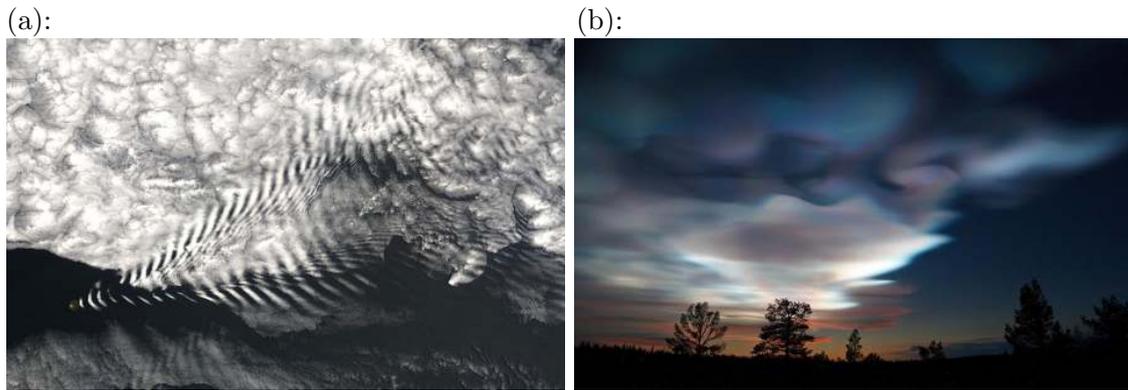
Figure 1.3.: (a): NASA satellite image (MODIS imager on board the Terra satellite) of a wave cloud forming off of Amsterdam Island in the far southern Indian Ocean. Image taken on December 19, 2005.[2] (b): Photograph of polar stratospheric clouds illustrating wave motion.[3]

In the following sections 1.1 and 1.2 I will introduce the studied phenomena in greater detail, present the current state of research on the respective fields and explain how our research approach is designed to meet our objectives. In sections 1.1.4 and 1.2.4 I phrase guiding research questions on the two topics. Ultimately, in section 1.3 I outline the structure of the dissertation.

---

[2]from `https://en.wikipedia.org/wiki/Wave_cloud`, downloaded in July 2018

[3]photo taken by Oliver Lemke, to be found at `https://img838.imageshack.us/img838/7888/psc110127full.jpg` as well as at `http://www.crystalinks.com/lenticular.html`, downloaded in July 2018

1.1. Convectively Generated Gravity Waves

Waves in the atmosphere result through the action of restoring forces on air parcels when displaced from an equilibrium position (Holton and Hakim, 2012). For a gravity wave the restoring force is the buoyancy force that is generated through adiabatic vertical displacement.

The gravity wave dispersion relation can be derived by applying linear theory, meaning that wave perturbations are only small departures from a stable background, on a set of equations describing the inviscid dynamics and thermodynamics of the fluid, as done in Fritts and Alexander (2003)

$$\hat{\omega}^2 = \frac{N^2(k^2 + l^2) + f^2(m^2 + \frac{1}{4H^2})}{k^2 + l^2 + m^2 + \frac{1}{4H^2}} \tag{1.1}$$

, where H is the scale height of the atmosphere. The dispersion relation, relating frequency $\hat{\omega}$ to wavenumbers k, l, m, underlies the environmental stratification, described by the Brunt-Vaisala-Frequency N, and planetary rotation, described by the Coriolis parameter f. Here, the focus is on gravity waves of medium scales, for which the frequency is $N \gg \hat{\omega} \gg f$. The dispersion relation then simplifies to

$$\hat{\omega} = N|\frac{k_h}{m}| \tag{1.2}$$

where $k_h = \sqrt{k^2 + l^2}$. The vertical wavenumber is then inversely proportional to the horizontal phase speed $\hat{c}_h = c_h - u_h$, where u_h is the mean background wind, and reads as

$$|m| = \frac{N}{\hat{c}_h}. \tag{1.3}$$

Atmospheric gravity waves have various sources. The most relevant of them are topography, fronts and jet streams, and as investigated here, convection. Due to this great variety of sources gravity waves are omnipresent in the atmosphere.

The propagation of gravity waves is affected by the environmental properties, given by stability, background flow and vertical shear, as well as it is dependent upon the generation mechanism. Ultimately the life cycle of gravity waves, starting from generation and propagation, ends with their dissipation, that is again affected by the environmental conditions.

Certainly upward propagation into the middle atmosphere and wave breaking are outstanding in their effect on the general circulation. At a critical level, where the background wind speed approaches the horizontal phase speed and $m \to \infty$, the wave breaks and its

momentum is deposited and by that the circulation is affected. Likewise the propagation of gravity waves is altered by the background flow. These processes are generally referred to as wave-mean flow interaction and play an important role for the circulation in the middle atmosphere.

1.1.1. The Universal Properties of the Gravity Wave Spectrum

Stratospheric gravity waves were first identified and their properties described in observational studies (Smith et al., 1985; Tsuda et al., 1989; Sato, 1992; Tsuda et al., 1994), using lidar and radar to obtain vertical profiles of wind and temperature fluctuations. Universal properties of the power spectral densities were found, analogously to gravity waves in the ocean (Garrett and Munk, 1972; 1975). These findings inspired theories, based upon analytical gravity wave models, for their explanation (Weinstock, 1985b; Dewan and Good, 1986; Smith et al., 1987; Hines, 1991; Sato and Yamada, 1994).

The spectrum, illustrated in Figure 1.4, thus consists of an unsaturated and a saturated regime, with the latter having a spectral slope proportional to m^{-3}. At a peak of power spectral density the two regimes are separated at the dominant vertical wavenumber. Towards smaller scales, at the buoyancy vertical wavenumber, the type of the motion turns from gravity waves to atmospheric turbulence, with a characteristic spectral slope of $m^{-5/3}$. The properties of gravity wave spectra, in vertical and horizontal wavenumber and in frequency space, are summarized in Gardner et al. (1993). In this dissertation we present an extensive test of modern atmospheric models in reproducing the universal spectral properties of gravity waves.
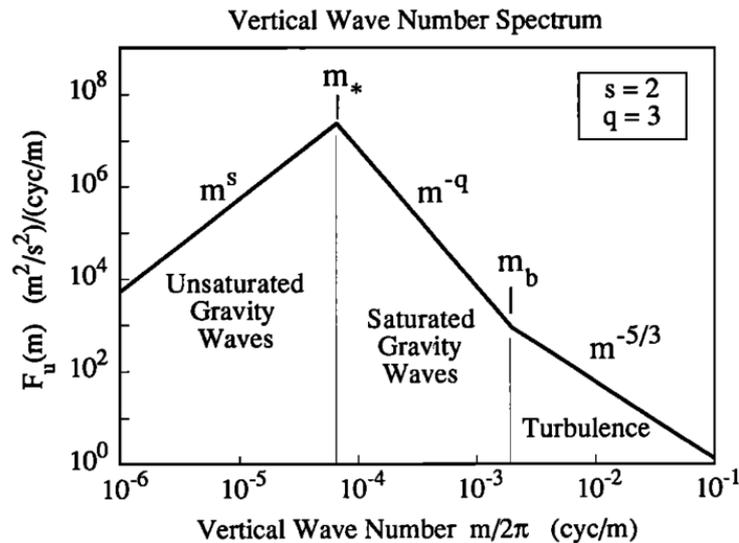
Figure 1.4.: The universal gravity wave spectrum for zonal velocity fluctuations u in vertical wavenumber space. F_u is the power spectral density of u, m_* and m_b denote the dominant vertical wavenumber and buoyancy vertical wavenumber, respectively. Adapted from Gardner et al. (1993).

1.1.2. Generation Mechanisms of CGGWs

Convective clouds generate gravity waves in the first place as a consequence of the release of latent heat. This mechanism is referred to as thermal forcing (Fritts and Alexander, 2003) and is used for parameterizations of CGGWs. In linearized models (Holton, 1973; Salby and Garcia, 1987) it was found that the latent heating profile in convective storms controls properties of the generated waves. Through the doubling of buoyancy frequency from the troposphere to the stratosphere the dominant vertical wavelength is expected to be equal to twice the vertical depth of the heating. This relation has been confirmed in observations (McLandress et al., 2000) and numerical modeling studies (Alexander et al., 1995). It is referred to as the *projection response*. Still, as shown in Holton et al. (2002), the response of gravity waves to a diabatic heat source is complex, and involves all spatial and temporal scales of diabatic heating.

Along with the thermal forcing two other convective gravity wave generation mechanisms, referred to as mechanical oscillation and transient mountain effect (Fritts and Alexander, 2003), have been discussed. Clark et al. (1986) describe the excitation of gravity waves through the oscillation of convective updrafts below a stably stratified layer. This mechanism was confirmed in numerical model studies of squall lines by Fovell et al. (1992) and Alexander et al. (1995). It is challenging to disentangle the generation mechanisms, as latent heating and vertical motion in convective clouds are intrinsically coupled. By means of a gravity wave source term analysis applied to a numerical model simulation of maritime sea-breeze convection, Lane et al. (2001) found that for these conditions the mechanical oscillator effect is the dominant convective gravity wave generation mechanism. However, in a related study, Song et al. (2003) showed that the mechanical generation is less efficient, as it is confined by the vertical propagation condition, and that the effectivity of mechanical (non-linear) and thermal (diabatic) forcing are of comparable magnitudes. The transient mountain effect only comes into play when there is flow across a convective cloud's top. Within the cloud latent heating lowers the potential temperature surface and air parcels flowing along the surface are displaced vertically like in flow over orography.

1.1.3. Numerical Modeling of CGGWs

Alexander and Holton (1997) and Piani et al. (2000) showed in numerical model studies of tropical deep convection that the small-scale gravity waves excited by deep convection can contribute significantly to the wave forcing necessary for driving the QBO (Baldwin et al., 2001). Sato and Dunkerton (1997) confirmed with observations that the momentum flux associated with gravity waves is much larger than those of Kelvin waves and Rossby-gravity waves. Here we investigate CGGWs with wavelengths of 10 to 1000 km, which were found to contribute most of the gravity wave momentum flux throughout the middle atmosphere (Preusse et al., 2008). We for this use numerical models of tropical dynamics,

and assess their sensitivity to spatial resolutions and model configurations. Convectively triggered gravity waves can hardly be resolved in current climate models and to this end (non-orographic) gravity wave parameterizations, accounting for underlying convective activity in the tropics, were introduced (Beres et al., 2005; Richter et al., 2010). Here we explore how the explicit treatment of both, convection and its gravity waves, will impact both their statistical and spectral properties. In doing so we can in advance assess how the convection-gravity wave links are realized in future generations of high-resolution climate models.

In the last two decades convection-permitting numerical model simulations became a leading tool in research on convectively generated gravity waves. Lane and Moncrieff (2008) describe characteristics of horizontal wavenumber and frequency spectra, in particular three dominant modes of the wave spectrum. They use a model solving non-hydrostatic anelastic equations of motion (Clark et al., 1996) for idealized simulations of tropical convection with similar, although two-dimensional, domain size and grid spacing as our high-resolution simulations and as such their study constitutes an important reference. Piani et al. (2000), Piani and Durran (2001) and Beres et al. (2002) used 3D models of squall lines and focused on the wave mean-flow interaction of CGGWs, that contributes to the QBO and mesospheric QBO. Another motivation concerns the representation of gravity waves in a numerical model itself, with Lane and Knievel (2005) and Watanabe et al. (2015) investigating the dependency of the gravity wave fields on spatial resolution and Stephan and Alexander (2014) on microphysical parameterizations. While the horizontal as well as the vertical grid spacing have a strong impact on the spectral characteristics and absolute momentum flux of gravity waves, microphysical parameterizations were shown to have little influence on gravity wave characteristics.

Along with continuously increasing computational resources, mesoscale-resolving general circulation models have become feasible. Liu et al. (2014), using a 0.25°-horizontal-resolution model, reveal that gravity waves become increasingly dominant with altitude and find a flattening of the slope of horizontal wavenumber spectra of kinetic energy with altitude. Holt et al. (2016) used a 2-year, 7-km-horizontal-resolution GCM to investigate tropical waves and the QBO. They found in their simulation, which still employed a parameterization of convection, that the zonal wave-forcing is still too low and a gravity wave parameterization is still needed to drive a QBO-like oscillation. These results raise questions on how spatial resolution impacts the stratospheric wave forcing in a general circulation model, and can still not estimate the numerical resolution at which gravity wave drag parameterizations become obsolete.

Eventually numerical modeling enables for numerous ways of visualizing gravity waves. An example for this are the plots of vertical velocity of Liu et al. (2014), at different altitudes, shown in Figure 1.5. At 206 hPa vertical velocity illustrates tropical convection, among that a tropical cyclone east of Australia. For higher altitudes the gravity waves
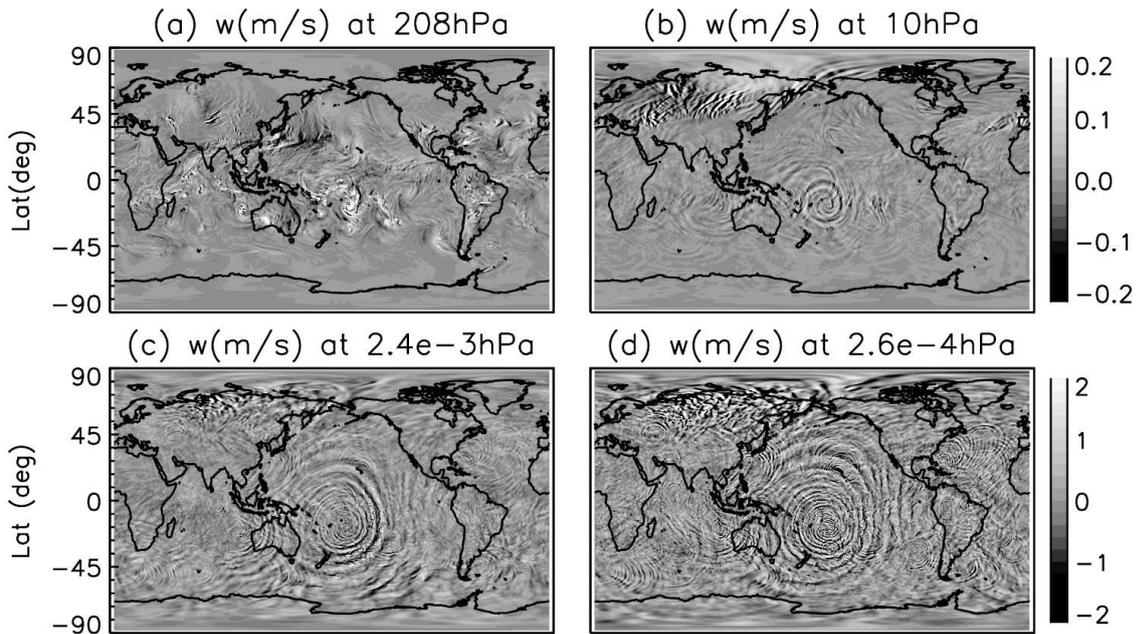
Figure 1.5.: From Liu et al. (2014): vertical velocity w $[\mathrm{ms}^{-1}]$ at different altitudes.

emanated by convection become evident and are seen to spread concentrically from the convection below. Also orographically triggered gravity waves are present, in particular above the Himalayas.

1.1.4. Research Questions and Objectives

I will investigate CGGWs by focusing on the following research questions:

1. **What are the spectral properties of gravity waves generated by a naturally evolving large-scale system of tropical convection?**
   In contrast to previous model studies, that mostly investigated a single convective event (Fovell et al., 1992; Alexander et al., 1995; Lane et al., 2001), I here aim at covering spatial scales up to the largest of tropical circulation and cloud systems, and the gravity wave spectrum emanated. In this way I explore the potential of convection to generate gravity waves at novel scales, from a few 1000 to a few 10 kms. To meet this goal I constructed a model of idealized tropical dynamics (the Spherical Limited Area Model (SLAM), introduced in Chapter 2). It uses a spherical domain, with a radius of an eighth of the Earth's, and by that the circumference of the domain is 5004 km. The high-resolution version has a horizontal grid spacing of 2.5 km, by which it fits into the class of "deep convection-permitting" models (Prein et al., 2015). Moreover I will explore convection and gravity waves in a range of numerical models of tropical dynamics, which allows me to study the second question:

2. **How are properties of CGGWs in numerical models affected by their numerical resolution, representation of convection and complexity of boundary conditions?**

   To answer this question, I use SLAM on a coarser horizontal grid, with a grid spacing of 20 km. At such resolution the application of a parameterization of convection is plausible, but not necessary. Thus I investigate one simulation with and the other without the use of a parameterization of convection. In addition to the idealized SLAM simulations I analyze two numerical simulations in realistic conditions of the tropical atmosphere, that also consider planetary rotation. The first is conducted on a global domain, where I focus on a region over the tropical Pacific ocean. The other is obtained from a numerical weather prediction model, at deep convection-permitting resolution, on a domain over the tropical Atlantic ocean. With this set of simulations I will investigate the sensitivity of both, convection and the gravity waves generated, to the models' specific differences.

1.2. Convective Aggregation in idealized simulations with SST gradients

1.2.1. Convective Aggregation in Nature

Atmospheric moist convection is found in organized structures and aggregates states throughout a large variety of scales.

At small scales there are cloud streets, formed from lines of horizontal shallow convective rolls (Etling and Brown, 1993). Deeper, precipitating convective clouds begin to interact with their cold pools, which form from evaporatively cooled downdrafts and propagate as density currents, and may then organize to form squall lines (Houze Jr, 1977; Rotunno et al., 1988).

At large scales the ITCZ, dynamically forced from low-level convergence of the trade winds, and thermally from peaking SSTs around the Equator, may be seen as a form of convective aggregation. Also the Madden-Julian-Oscillation (MJO), which is in many regards still an open challenge for tropical meteorology, manifests as a cluster of convective clouds with a horizontal scale on the order of thousands of kilometers, propagating from the Indian into the Pacific Ocean (Zhang, 2005). Ultimately tropical cyclones form from aggregated cloud clusters (e.g. Wing et al., 2016). Equatorial waves, such as Rossby-gravity, inertia-gravity and Kelvin waves, are observed to be coupled to convection and by that organize convection in the tropics (Kiladis et al., 2009).

1.2.2. Convective Self-Aggregation in Numerical Models of RCE

The principle heat budget of the tropical atmosphere is radiative-convective equilibrium (RCE) and it means the statistical equilibrium of convective heating and net radiative cooling. On the one side, longwave radiative emission renders the troposphere unstable to convection, on large spatial scales and relatively long temporal scales, and tries to force the atmospheric temperature profile towards that of radiative equilibrium. On the other side, deep convection reacts to the destabilization and then heats the atmosphere locally and quickly, i.e. within a diurnal cycle. An important role in here is played by gravity waves: they distribute the heat horizontally (Bretherton and Smolarkiewicz, 1989) and maintain the weak temperature approximation of the tropical atmosphere (Sobel et al., 2001).

First numerical models of RCE were single column models (Manabe and Strickler, 1964; Manabe and Wetherald, 1967), where atmospheric radiative transfer was solved and convective heating parameterized. It was found to be an accurate model of the tropical atmosphere and allowed for pioneering studies of the Earth's climate, reviewed in Ramanathan and Coakley (1978). These models can be extended by a second column and allow then to yield estimates of precipitation and circulation (Sobel and Bretherton, 2000).
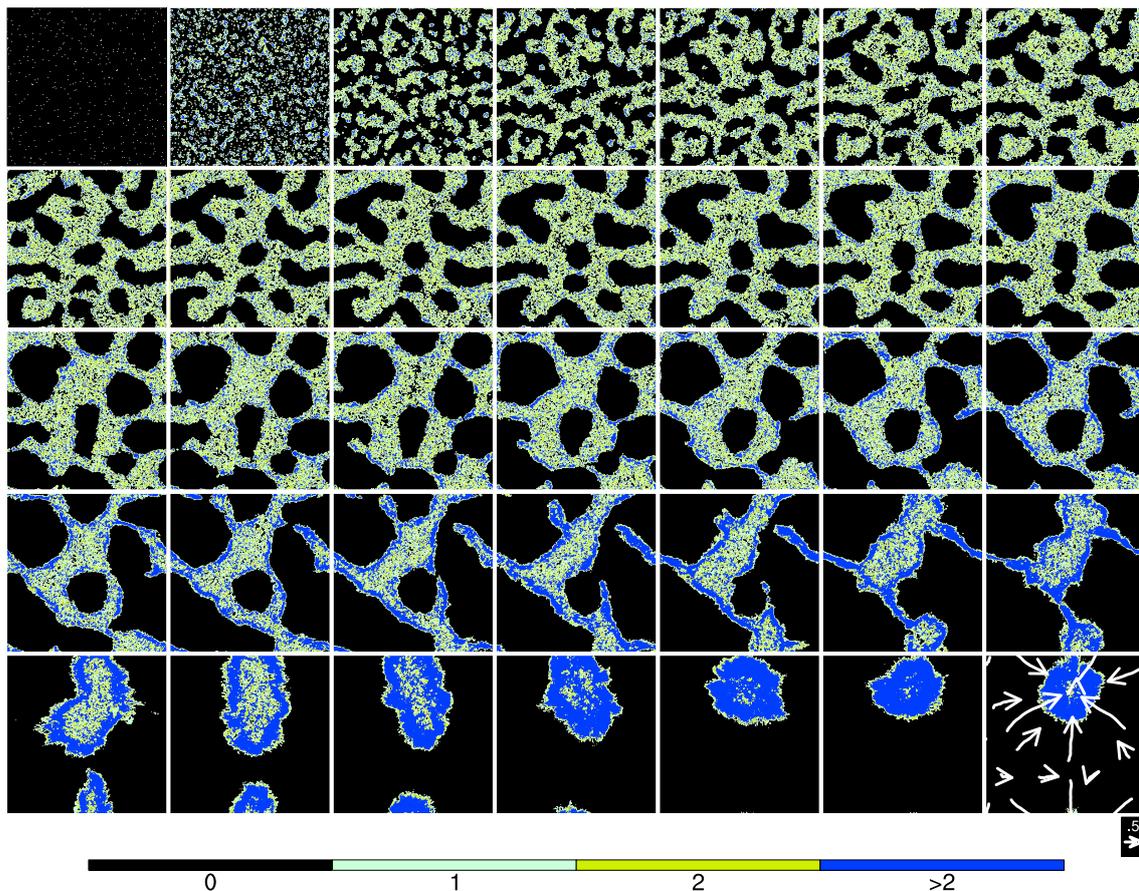
Figure 1.6.: Convective evolution in a typical convection-permitting RCE simulation of Hohenegger and Stevens (2016). Each panel shows one day and illustrates the spatial distribution of convective updraft occurrence per day.

Two-dimensional (e.g. Held et al., 1993) and three-dimensional (e.g. Tompkins and Craig, 1998) convection-permitting limited area models of RCE, as well as global models with convective parameterizations (e.g. Held et al., 2007), introduce the spatial variability of moist convection in RCE and eventually led to the discovery of convective self-aggregation (e.g. Held et al., 1993; Bretherton et al., 2005).

Convective self-aggregation constitutes the basic form of convective organization, as it occurs independently of any external forcing. It describes the clustering of convective clouds despite homogeneous boundary conditions and forcing.

The classical model setup of convection-permitting numerical simulations of RCE showing self-aggregation has a square domain and is characterized by horizontally uniform boundary conditions, with fixed SSTs and solar insolation (reviewed in Wing et al., 2018), in absence of background wind and planetary rotation. From initially randomly scattered convective clouds deeper cells form, and ultimately one moist region emerges, containing all convective clouds. This convective evolution is illustrated in Figure 1.6.

Wing et al. (2018) present a review on convective self-aggregation. They summarize physical processes that have been identified to be relevant in convective self-aggregation. Those are longwave radiation (e.g. Bretherton et al., 2005; Holloway and Woolnough, 2016), shortwave radiation (Wing and Emanuel, 2014), surface fluxes (e.g. Bretherton et al., 2005; Wing and Cronin, 2016) and moisture feedbacks (e.g. Tompkins, 2001), advective processes (e.g. Bretherton et al., 2005; Muller and Bony, 2015), and eventually also buoyancy bores (Mapes, 1993). The relative importance of these processes was found to change with SSTs and also depends upon whether the cloud cluster is in a stage of transient development or quasi-equilibrium.

Still it was identified that cloud-radiative effects may play a crucial role in generating a shallow overturning circulation. By that the overturning circulation associated with convective aggregation was found to be distinctly two-celled (Bretherton et al., 2005). The shallow branch promotes aggregation by importing moist static energy into the cluster and many studies show that it is mainly driven by longwave radiative cooling near low-level cloud tops (Muller and Held, 2012; Muller and Bony, 2015). Further evidence for the importance of cloud-radiative effects are given by simulations with homogenized longwave radiation, where it is found that convection is inhibited (Hohenegger and Stevens, 2016). For these reasons the overturning circulation of an aggregated system is referred to as *radiatively driven.*

Not only the clouds but also their environment plays an important role in convective self-aggregation. The cloud cluster forms within a "moist bubble", reducing entrainment efficiency and preventing updraft buoyancy reduction (Becker et al., 2018), whereas the rest of the domain is exceptionally dry. This contrast in moisture distribution means that convective self-aggregation manifests in the spatial variance of, e.g. the water vapor path. Furthermore the dry environment can be interpreted as a "radiatively driven cold pool" (Coppin and Bony, 2015). In that area the clear-sky conditions promote longwave radiative cooling, which in turn promotes subsidence and drying, and by that the dry area is stabilized against moist convection. Thus the dry cloud-free area is not only a result but also a driver of convective self-aggregation.

The tendency of numerical RCE models to develop an aggregated cluster was found to be dependent upon prescribed SSTs (Wing and Emanuel, 2014), domain size and grid spacing (Muller and Held, 2012) and the model-specific representation of convection, such as a convective parameterization (Becker et al., 2017) and entrainment (Tompkins and Semie, 2017). The Radiative-convective equilibrium model intercomparison project (RCEMIP) (Wing et al., 2018) aims at evaluating the robustness of convection-permitting RCE models in terms of convective self-aggregation and its drivers.

Studies on convective self-aggregation also suggest the phenomenon's relevance for the mean state and sensitivity to climate change. Held et al. (1993) have found that the occurrence of convective self-aggregation is sensitive to the specified SST, simulating the

impact of climate warming on self-aggregation. This is of great interest as convective self-aggregation was found to come along with a decrease in anvil cloud fraction (Bony et al., 2016) and a domain-mean drying of the atmosphere (e.g. Tobin et al., 2012). Both of these changes mean an increase in outgoing longwave radiation and thus cause a cooling of the troposphere.

If convective self-aggregation was favored above warm SSTs this would constitute a negative feedback on climate warming, a mechanism referred to as the "iris effect" (Mauritsen and Stevens, 2015). For that reason an improvement of the representation of tropical convection and convective aggregation in climate simulations attains great importance. Still a convection-permitting numerical resolution remains illusive in general circulation models on decadal time scales. For this reason until now idealized modeling frameworks are used to improve upon the basic understanding of the phenomenon. On the same line the World Climate Research Programme (WCRP) Grand Challenge Initiative on Clouds, Circulation and Climate Sensitivity recognized the importance of the phenomenon and encourages the scientific community by phrasing the question "What role does convective aggregation play in climate?" (Bony et al., 2015).

Mapes (2016) assesses the topic critically and reminds that the transfer of understanding on convective self-aggregation onto the real atmosphere and its climate may be limited. Still the lessons learnt from convection-permitting RCEs are expected to facilitate the understanding of full-complexity Earth System models. As an intermediate step towards understanding models of full complexity, I here introduce a convection-permitting model of RCE in not purely homogeneous boundary conditions.

1.2.3. Atmospheric Rivers

The simulations conducted for this study raised our interest in looking at the transport of moisture associated with atmospheric rivers (ARs).

ARs are narrow, elongated, synoptic-scale streams, rich of water vapor, that play a crucial role in the global water cycle and also for regional weather. Newell et al. (1992) were first to identify the filamentary structure of the meridional daily global water vapor flux, from the tropics across mid-latitudes, in NWP model output. Already then it was found that an individual "tropospheric river" could carry about as much water as the Amazon. Zhu and Newell (1998) proposed a detection algorithm, accounting for the ARs' typical dimensions, low altitudes, moisture content and moisture flux characteristics. It was found that in mid-latitudes ARs mediate almost the entire meridional moisture transport though spanning only a tenth of the longitudinal length at a given latitude. ARs originating from the tropics were found to precede cold fronts, and are thus located within the warm sector of extra-tropical cyclones and and exhibit characteristics of a low level jet and warm advection in their vertical shear (Ralph et al., 2004; 2005).
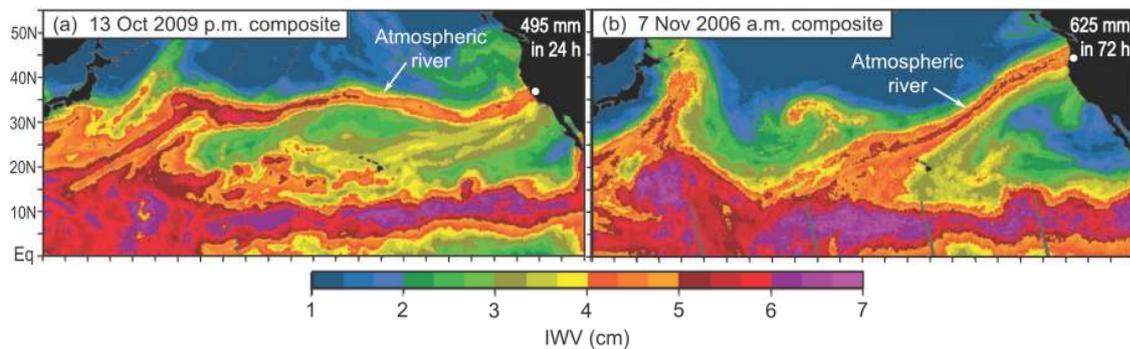
Figure 1.7.: From Ralph et al. (2010): Composite SSM/I satellite images of integrated water vapor IWV [*cm*] of an AR emanating from the tropical (a) western Pacific on the afternoon of 13 Oct 2009 and (b) central Pacific on the morning of 7 Nov 2006 (see Neiman et al. (2008) for a detailed summary).

The relevance of ARs, in weather and extreme events, was again demonstrated by Lavers et al. (2012) who found ARs to be associated with the majority of winter floods in Great Britain. Likewise Eiras-Barca et al. (2018) identified the concurrency of explosive extra-tropical cyclogenesis and ARs. But also when making landfall solely, like prominently at the west-coast of California, ARs may cause extreme precipitation and flash floods (Neiman et al., 2008). Guan and Waliser (2015), using another detection algorithm, present a climatology of the spatial and temporal distribution of ARs, of their precipitation, the location of their landfall and their relation to the El-Nino Southern Oscillation (ENSO) and to the MJO.

In a case study of a landfalling AR (Ralph et al., 2010) show the environment's multi-scale complexity. Figure 1.7 illustrates the AR by the field of precipitable water. The characteristic scales of an AR and the moisture export, from the tropics into the mid-latitudes, are evident. They revealed that an extra-tropical wave packet established a direct connection of an AR with the tropical moisture pool. Further the authors make links to the equatorial conditions, that were dominated by a MJO event, with eastward propagating pulses of convectively coupled Kelvin waves. Eventually the duration of the event was seen to be increased by the presence of a mesoscale frontal wave. Nevertheless, they emphasize that the environmental conditions of ARs may vary, and thus may be less complex as well. In contrast to that, we in our simulations find the occurrence of an atmospheric river-like flow in a basically unperturbed environment.

1.2.4. Research Questions and Objectives

Aside from tropical cyclones, large-scale tropical convective systems are predominantly zonally elongated. Reasons for this are found in the equatorial wave guide (Kiladis et al., 2009) and, as seen in the ITCZ, in SST distributions and in the line of convergence of the trade winds. Convection-permitting RCE simulations on convective self-aggregation were

traditionally conducted on square domains with uniform SSTs and show the development of a cloud cluster with circular shape.

In this study of convective aggregation, I investigate simulations with boundary conditions characterized by a gradient in SST and focus on the following research questions:

1. **How does a meridional SST gradient affect the convective evolution and convective aggregation? In particular, how does it influence the zonal dimension, and does zonal convective self-aggregation occur?**
   I again use my idealized model of tropical dynamics, SLAM, a convection-permitting RCE simulations on a spherical domain (introduced in Chapter 2). Differently to previous studies I impose a SST profile, characterized by a meridional gradient and zonal symmetry. This means that convective aggregation is forced in the meridional dimension to form a convergence line at the parallel of maximum SSTs. However, boundary conditions are homogeneous in the zonal dimension, and thus in principle permit convective self-aggregation to occur. Two simulations with differently steep SST gradients are conducted and allow to study their effect on the convective evolution and mean-state characteristics of the emerging cloud clusters.

2. **How does the asymmetry of a cloud cluster affect the environment?**
   Convection-permitting RCE simulations using a long-channel geometry (e.g. Posselt et al., 2012; Wing and Cronin, 2016) find that, due to advective processes, the domain-mean moisture is greater than in RCE simulations using a square domain. This setup I may identify as most closely related to mine. Likewise, in my simulations the shortcoming of traditional simulations of convection self-aggregation, their very dry non-convecting regions, is overcome as well. In my simulations cloud clusters of zonally elongated shape emerge, for which we refer to them as "asymmetric". We will study how these clusters behave differently to ones in radial symmetry. In particular I will show how the shallow circulation moistens originally dry areas and how this circulation feature relates to atmospheric rivers.

In general we want to introduce which changes are to be expected when convection-permitting RCE studies are conducted in not purely homogeneous boundary conditions. The simulated cluster and its associated circulations naturally become more complex and their understanding becomes more challenging. Still these simulations may overcome shortcomings of the traditional RCE simulations and a transfer of understanding into more realistic models of the tropical atmosphere could be facilitated.

1.3. Thesis Outline

The thesis presented here is structured in the following way. In chapter 2 we introduce and describe basic properties of the idealized model of tropical dynamics, SLAM, we developed.

In chapters 3 and 4, SLAM is used to investigate convectively generated gravity waves and convective aggregation, respectively, and to address the research questions outlined above. Finally, in chapter 5, I summarize results and conclusions, answer the research questions and present a scientific outlook.

.

THE SPHERICAL LIMITED AREA MODEL - SLAM

For this work a new configuration of the ICOsahedral Non-hydrostatic atmosphere model ICON-A was developed - the Spherical Limited Area Model (SLAM). The aim was to conduct simulations of moist convection, its associated circulations leading to convective organization and the atmospheric gravity waves emanated by convection, for tropical conditions, close to the Equator, where rotation can be neglected. We have therefore developed SLAM as a model of the atmospheric radiative-convective equilibrium on a spherical domain and without planetary rotation.

2.1. ICosahedral Non-hydrostatic Model- ICON

ICON is a joint development by MPI-M and the German weather service (DWD). It is a unified numerical model of the atmosphere, developed for application in both research and numerical weather prediction as well as for operation on both global and regional scales. An explicit representation of small scale weather phenomena, like convection and gravity waves, requires a non-hydrostatic dynamical core and fine grid spacing, which increases computational costs. For this reason unified models are designed to still be computationally efficient when massively parallelized on modern super-computers. In order to avoid resolution clustering and singularities at the poles, detrimental to their numerical scalability, unified models use new types of grids, many of them based upon platonic solids. These are summarized in Staniforth and Thuburn (2012). For ICON the

horizontal grid is derived from an icosahedron, which is refined by the subdivision of its equilateral triangles into smaller cells (Wan et al., 2013).

The SLAM is based upon the ICON-A version, which is developed for an application in climate modeling and described in (Giorgetta et al., 2018). ICON-NWP is operated by DWD for global and regional numerical weather prediction, and ICON-LEM is designed for Large-Eddy simulations (Dipankar et al., 2015). All of these versions share the same non-hydrostatic dynamical core, briefly described in Section 2.1.1, but they differ in their representation of physical processes. In SLAMs, as in ICON-A, the physics parameterizations of the ECHAM6 model are used and described in Section 2.1.2.

2.1.1. Dynamical Core

ICON's dynamical core is described in detail in Zängl et al. (2015). A set of compressible non-hydrostatic equations of the atmosphere, based upon the prognostic variables suggested by Gassmann and Herzog (2008), is used. The horizontal grid is an unstructured icosahedral-triangular Arakawa C grid. The grid-specific discretizations of basic mathematical operators were developed in Wan et al. (2013). The vertical grid follows the smooth level vertical (SLEVE) coordinate, described in Leuenberger et al. (2010). A two-time-level predictor-corrector scheme is implemented for time integration. Time splitting is done between the dynamical core on the one hand and tracer advection, physics parameterizations and horizontal diffusion on the other hand. The latter consists of a flow-dependent second-order Smagorinsky diffusion of velocity and potential temperature in combination with a background fourth-order Laplacian diffusion of velocity. In addition, the dynamical core contains a fourth-order divergence damping term for numerical stability. At the model top a Rayleigh damping layer, following Klemp et al. (2008), may be defined, in order to prevent wave-reflection at the model top.

2.1.2. Physical Parameterizations

The physical parameterizations of ICON-A are adopted from the ECHAM6 model and described in detail in Giorgetta et al. (2013) and Stevens et al. (2013).

For all SLAMs we use parameterizations of cloud microphysics, radiation and a numerical diffusion scheme. Parameterization schemes for orographic and non-orographic gravity waves are available but not used in this work. The cloud-microphysical scheme solves prognostic equations for water vapor, liquid, and ice and is described in detail in Lohmann and Roeckner (1996). The radiative transfer model PSrad of Pincus and Stevens (2013) is used to derive the solar shortwave and terrestrial longwave radiative heating. Vertical diffusion is parameterized by a total turbulent energy scheme, that was first formulated by Mauritsen et al. (2007) for stable and neutrally stable conditions. It was extended for unstable conditions by Angevine et al. (2010) and implemented and evaluated for its

impact on the general circulation in ECHAM6 by Pithan et al. (2015).

For one low-resolution simulation moist convection is parameterized with a mass-flux scheme based on Tiedtke (1989) with updates following Nordeng (1994).

2.2. From Aqua Planet Simulations towards Radiative Convective Equilibrium

Here we describe how, driven by the aim of isolating tropical dynamics and convection, the Spherical Limited Area Model is built through modifications of the Aqua Planet Experiment (APE) (Neale and Hoskins, 2000b;a) in ICON-A. Aqua Planet Experiments are performed on global domains without orography and only water as their lower boundary. They are characterized by prescribed and fixed idealized sea surface temperature profiles. Their initial state, in terms of the zonal-vertical distribution of potential temperature, pressure and zonal circulation, follows that of the Jablonowski-Williamson testcase (Jablonowski and Williamson, 2006). They constitute an idealization of both mid-latitude and tropical dynamics of the earth's atmosphere. Within an hierarchy of models of the atmosphere the APE is seen as a bridge in between models of idealized physics and idealized dynamics (Blackburn and Hoskins, 2013).

The field of application of this idealization of the atmospheric circulation is vast. Due to its simplicity the APE was used to approach cloud-resolving numerical resolution on a global domain (Tomita et al., 2005). It was used to study mid-latitude storm tracks (Brayshaw et al., 2008; Lu et al., 2010), but still, for its water surface, the APE is ideal for studying tropical convection (Nasuno et al., 2007), equatorial waves (Lin et al., 2008), the MJO (Grabowski, 2003) and to test sensitivities to the representation of convection.

2.3. Development of the Spherical Limited Area Model

The two main modifications to the APE setup are (1) to set planetary rotation to zero and (2) to scale the radius of the spherical domain. By neglecting Coriolis effects the dynamics of the equatorial atmosphere are isolated, as the development of baroclinic waves, representing mid-latitude dynamics, is prevented. By setting planetary rotation to zero we then may arbitrarily change the radius of the sphere, as we avoid complications with the ratio of gravity and Coriolis acceleration and of buoyancy acceleration and vertical advection (Bechtold et al., 2016). At last, by changing the sphere's radius, not only the domain size, but in combination with the choice of the grid, also the grid spacing is controlled.

In summary, SLAM is a model of the atmospheric radiative-convective equilibrium on a spherical domain.
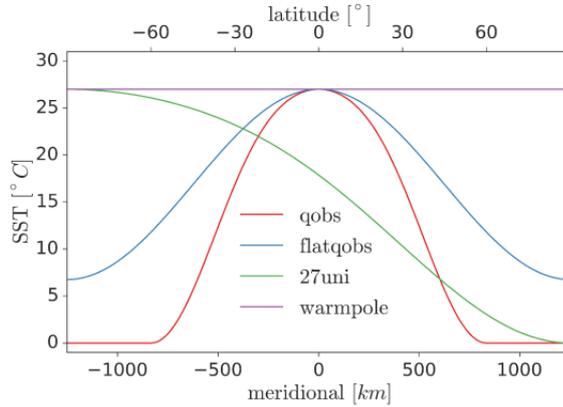
Figure 2.1.: Zonally uniform sea surface temperature profiles applied to SLAMs of this thesis.

2.3.1. Boundary Conditions and Initialization

The boundary conditions chosen depend upon the purpose of the experiment. The sea surface temperature profiles used in the SLAM originate from the APE setup and are zonally symmetric. The SSTs, through surface fluxes of heat and moisture, basically determine the location of convection and its associated overturning circulation. The profiles investigated for this study are shown in Figure 2.1. For Chapter 3 the imposed solar insolation is homogenized in the zonal dimension, but still varies meridionally. By that zonally traveling tides in the middle atmosphere, driven by short wave heating, are prevented. For Chapter 4 the solar insolation is uniform for the entire domain. For both setups the insolation has a diurnal cycle, incidents perpendicular and the solar constant is set to 1360.875 W m^{-2}. The ozone profile used is that designed for the Aqua Planet Experiment[1]. We use the initialization following the Jablonowski-Williamson testcase, but set zonal wind speeds to zero, as westerly jets are not of interest. [1]

2.3.2. Domain Properties and Grids

For all SLAM simulations in this thesis the domain is a sphere with a radius of an eighth of the Earth's. This results in a circumference at the central parallel of 5004 km and a domain area of 8 million km^2. We identified this scale to be large enough for resolving large-scale tropical overturning circulations.

We use the grids R2B4 and R2B7, which are derived from refinements of the icosahedron. On R2B4 SLAM has a horizontal grid spacing of 20 km and this configuration is hereafter referred to as the coarse version "coSLAM". On R2B7 SLAM has a horizontal grid spacing of 2.5 km, which constitutes our high-resolution version referred to as "hiSLAM". The grids' properties are summarized in Table 2.1. The vertical grid used for studying convectively generated gravity waves was chosen to have a top at 83 km with

---

[1]see http://www.met.reading.ac.uk/~mike/APE/ape_ozone.html

	n_c	$\bar{a}$ [km^{-2}]	$\overline{\Delta x}$ [km]
R2B4	20480	389.15	19.73
R2B7	1310720	6.08	2.44

Table 2.1.: Details on the horizontal grids used in this study, for a scaling by a factor of 0.125. n_c is the number of grid cells, $\bar{a}$ is mean grid cell area, $\overline{\Delta x} = \sqrt{\bar{a}}$ is the mean grid spacing.
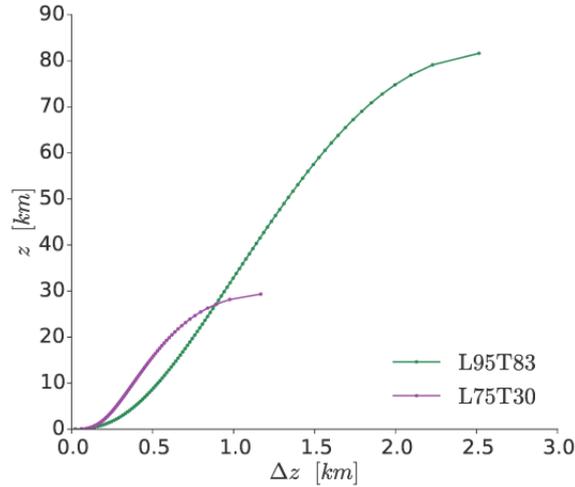
Figure 2.2.: The two vertical grids used in SLAMs of this thesis, described by the grid spacing at the respective altitudes.

95 levels and is referred to as L95T83. For the investigation of convective aggregation on SLAMs a vertical grid with a top at 30 km and 75 levels is used and is named L75T30. The grids are illustrated in terms of the grid spacing at the respective altitudes in Figure 2.2. Rayleigh damping is applied above 50 km for L95T83 and above 25 km for L75T30. All the simulations conducted for this thesis are summarized in Table 2.1.

2.3.3. SLAM simulation summary

For this thesis we conducted 7 different simulations using SLAM. They differ in their horizontal and vertical grids and SST profiles and one is conducted using a parameterization of convection. The simulations are summarized in Table 2.3.3.

2.4. SLAM characteristics and model evaluation

Here we describe typical characteristics of SLAMs. We test the models through a comparison of the thermally driven overturning circulation to that of reanalysis data and of precipitation to observations. Further descriptions of the models' circulation and convective evolution are given in Sections 3.2 and 4.3.1.

name	horizontal grid	vertical grid	SST profile	insolation
hiSLAM	R2B7	L95T83	qobs	meridionally varying
coSLAM-xc	R2B4	-"-	-"-	-"-
coSLAM-pc convection parameterized	-"-	-"-	-"-	-"-
hiSLAM_qobs	R2B7	L75T30	qobs	uniform
hiSLAM_flatqobs	-"-	-"-	flatqobs	-"-
hiSLAM_27uni	-"-	-"-	27uni	-"-
hiSLAM_warmpole	-"-	-"-	warmpole	-"-

Table 2.2.: Summary of all SLAM simulations studied in this thesis.

2.4.1. Meridional Circulation and Latent Heating

Figure 2.3 illustrates the thermally driven overturning circulation of simulations hiSLAM and hiSLAM-qobs by the zonal and temporal mean of latent heating rate and of the meridional mass-stream function Ψ_M. At the central parallel, where SSTs peak, latent heat is released in convective clouds and the air ascends. Below the tropopause the air diverges and flows polewards. However, a large fraction of the domain, as of the tropics, is cloud-free and there is slow descending motion, driven by longwave radiative cooling. Apart from the lack of easterly trade winds, this circulation resembles the Hadley Cell. It contains another shallower circulation reaching up to altitudes ~ 5 km. This circulation is driven by shallow and congestus convection not reaching the freezing level. For both simulations the strength of the circulation as a whole is weaker than seen in reanalysis data (Stachnik and Schumacher, 2011). They find for different reanalyses a maximum magnitude of the temporal mean of Ψ_M of $\sim 10 \times 10^{10}$ kg s^{-1}, whereas hiSLAM reaches $\sim 2.5 \times 10^{10}$ kg s^{-1}. This difference may be explained by the smaller meridional extent of our circulation in combination with the shallower troposphere. (Stachnik and Schumacher, 2011) show that the Hadley Cell, with both southern and northern branch, spans 65° in latitude, which is about 7200 km. In comparison to that our circulation spans from pole to pole over about 2500 km.

We also find that the thermal overturning circulation, as quantified by Ψ_M, is weaker in hiSLAM-qobs than in hiSLAM. The simulations only differ in their vertical grid and solar insolation, as outlined in Section 2.3.3. The spatially uniform solar insolation used in hiSLAM-qobs means also that there is a greater incoming shortwave radiative flux. Through absorption by water vapor the troposphere is heated. By that longwave radiative cooling and the associated thermal destabilization of the free troposphere are opposed. As a consequence the meridional overturning circulation is weakened. spacing
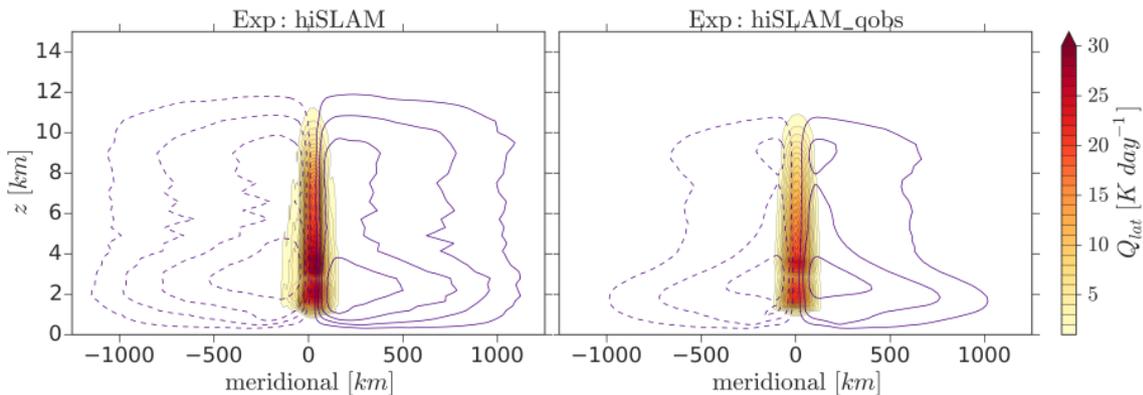
Figure 2.3.: For experiment hiSLAM on the left, and experiment hiSLAM-qobs on the right: meridional-vertical cross-section of the temporal and zonal mean of latent heating, Q_{lat} [K day^{-1}], and the mean meridional mass-stream function Ψ_M in contours with intervals of $5*10^9$ kg s^{-1}.

2.4.2. Initial and equilibrium temperature profile

Figure 2.4 shows the initial temperature profile of hiSLAM on L95T83, which is uniform over the whole domain. The equilibrium temperature profiles at the central parallel and at the pole are also shown. They hardly differ, except for the lowest layers, where they are impacted by surface heat fluxes. Above that, the profiles are very similar. This shows that temperature gradients are weak when the Coriolis force is small. The reason for this is that gravity waves efficiently distribute horizontally heat away from convection (Bretherton and Smolarkiewicz, 1989) and by that erase temperature gradients. This property is used in analytical models of the tropical atmosphere in form of the weak temperature gradient (WTG) approximation (Sobel et al., 2001). In the stratosphere, radiative equilibrium with the prescribed ozone field is reached.

2.4.3. Temporal Evolution of Precipitation and Moisture

Panels (a) and (b) of Figure 2.5 show the temporal evolution of the domain mean and daily mean of precipitation for all SLAMs, for a period of *Tropical Rainfall Measuring Mission* (TRMM) observations over the equatorial region of the Pacific and of an Aqua Planet Experiment conducted with ICON on the grid R2B7 (APE: unscaled radius, $\Rightarrow$ $\overline{\Delta x}$ = 19.73 km). The comparison of SLAMs to TRMM and APE by precipitation can give an estimate of how comprehensive our idealization of tropical dynamics is. This is because of the proportionality of precipitation to the total amount of heating through convection. In turn that means that also the thermally induced overturning circulations, that result from the convective heating can be related to the real atmosphere through the comparison of SLAMs' precipitation to TRMM and APE. We find that the time mean of precipitation, shown in the legend of Figure 2.5 (a), is for all models but hiSLAM_warmpole only slightly less than for TRMM. We see this as a convincing evidence for the reasonable
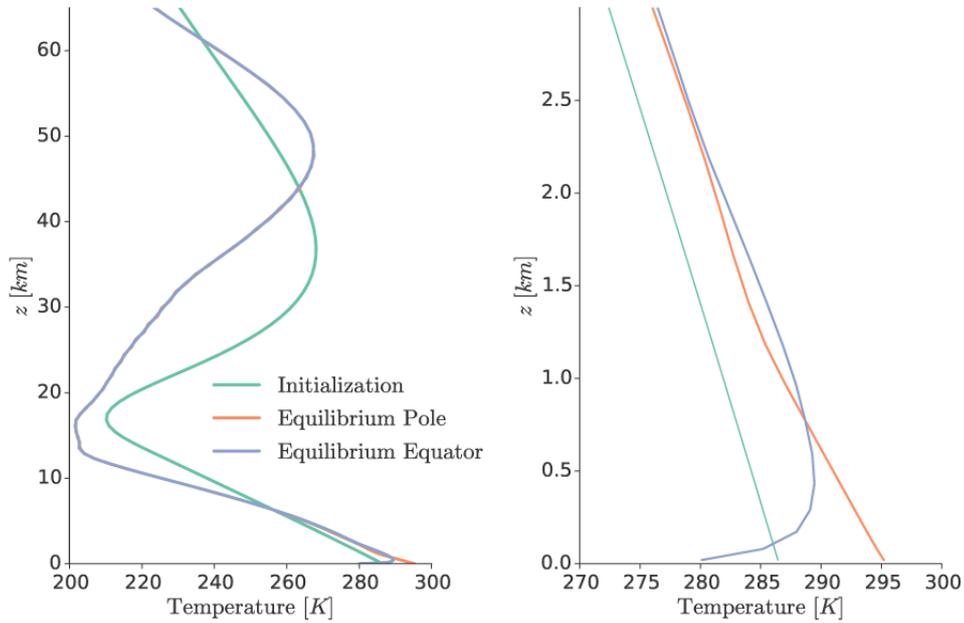
Figure 2.4.: Representative for all SLAMs, derived from experiment hiSLAM: Vertical temperature profiles at initialization and as a temporal mean over the last month of integration, at a pole and at the central parallel (Equator), respectively.

idealization of tropical dynamics in SLAMs. However the APE has a greater temporal mean in tropical precipitation, suggesting that the underlying model, as SLAMs, is slightly overestimating precipitation. The difference seen of APE to SLAMs is explained through the activity of equatorial waves and tropical cyclones, that may enhance precipitating convection compared to a non-rotating RCE simulation.

Figure 2.5 (c) is a display of the diurnal variability of the domain mean precipitation for SLAMs. The diurnal cycle of solar insolation and its impact on convection is reflected. Notably the APE shows a far weaker diurnal cycle than SLAMs. Again we explain this by the presence of equatorial waves and tropical cyclones, that are, because of their underlying dynamics, less affected by the solar forcing.

Figure 2.5 (d) shows the temporal evolution of the domain mean precipitable water for SLAM. At first in all SLAMs the atmosphere gets dryer. After ~30 days in all simulations but SLAM_warmpole the atmospheres moisten again. Still also hiSLAM_warmpole is not drying out completely and like all other simulations attains a stable state regarding its moisture content eventually. Sea surface temperatures, shown in Figure 2.1, are on average highest in hiSLAM_27 and lowest in hiSLAM_warmpole and as a consequence of that these simulations develop the moistest and driest atmospheres, respectively. In their mean moisture content and mean precipitation hiSLAM, coSLAM-xc and hiSLAM_qobs differ only slightly, showing no significant impact of the chosen horizontal or vertical grids. Also the parameterization of convection, as used in coSLAM-pc, is of little impact
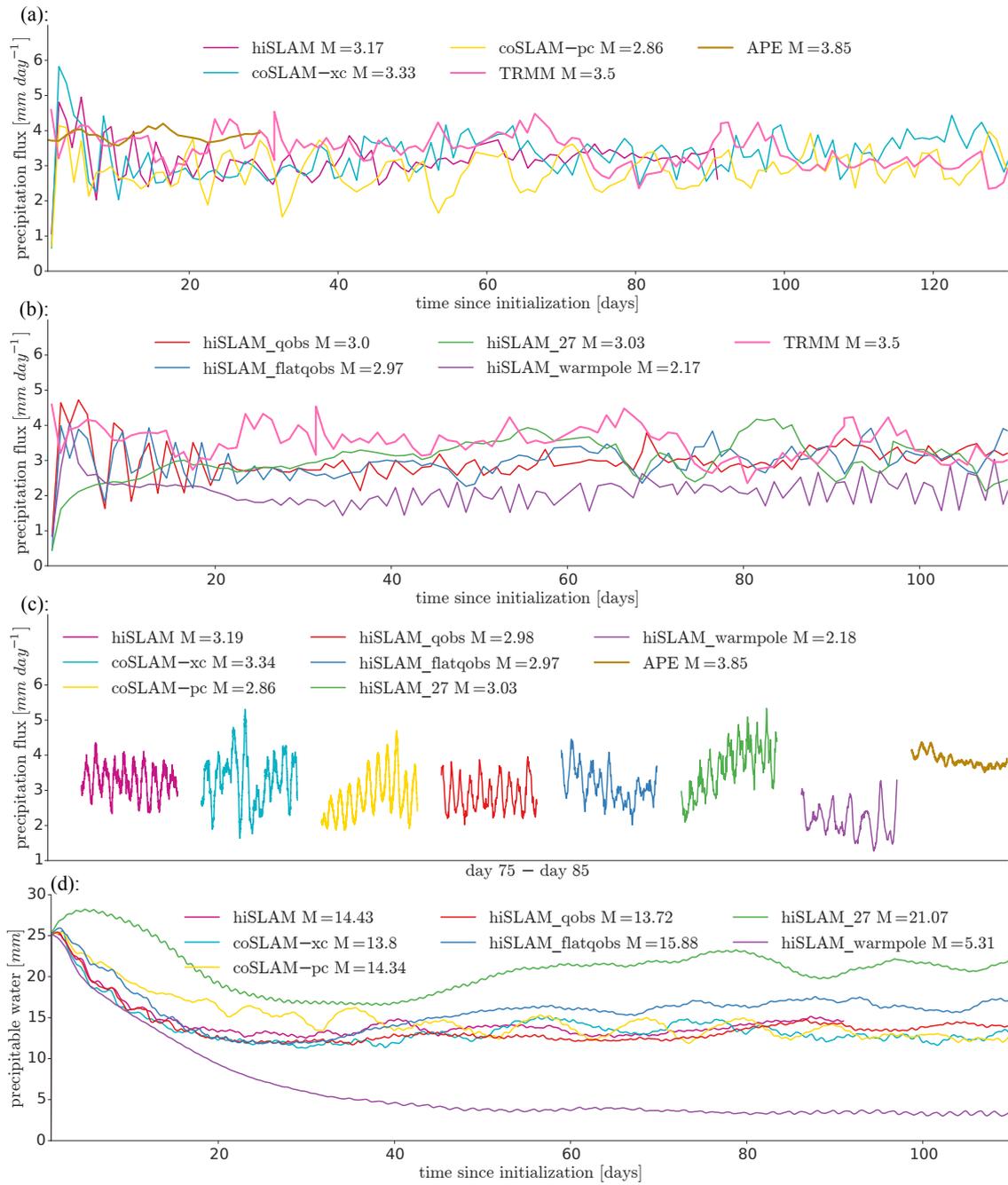
Figure 2.5.: Panels (a) and (b): Domain mean of the daily mean of precipitation flux [mm day^{-1}] of SLAMs, an Aqua Planet simulation (APE) and TRMM observations over the Pacific [120°E-280°E;30°S-30°N] for the time period 2003/01/01-2003/04/21. The temporal mean, of the whole period shown, is given in the legend. Panel (c): Domain mean precipitation flux [mm day^{-1}], for days 75 to 85 respectively (days 15-25 for APE). Panel (d): Vertically integrated water vapor (precipitable water) [mm].

on moisture and precipitation.

CONVECTIVELY GENERATED GRAVITY WAVES IN HIGH-RESOLUTION MODELS OF TROPICAL DYNAMICS

Here we investigate the realization of convectively generated gravity waves in a range of numerical models of tropical dynamics. These are SLAM simulations of idealized tropical dynamics and two numerical simulations with realistic global initial and boundary conditions of the tropical atmosphere. The simulations display the evolution of global circulation models towards convection-permitting resolutions, by covering grid spacings from 20 to 2.5 km. In particular with hiSLAM we resolve deep tropical convection on large spatial and long temporal scales and investigate CGGWs on scales of a few 1000 to a few 10s of kilometers, that were until now neither resolved nor parameterized.

The study is structured in the following way: the simulations, as well as the methodology of their statistical and spectral analysis, are introduced in section 3.1. Section 3.2 describes the simulations' large-scale circulation and cloud distribution. Then the statistical and spectral properties of properties of tropical convection are analyzed to estimate their ability to generate gravity waves. Section 3.3 provides a thorough analysis of convectively generated gravity waves in spectral space and tests the simulations for the realization of universal properties of the gravity wave spectrum. We discuss the results in Section 3.4 and summarize conclusions in Section 3.5.

3.1. Methods

3.1.1. Numerical Models and Simulations

As our primary tool we used the idealized model of tropical dynamics, SLAM, introduced in Chapter 2, to conduct a set of three well-comparable simulations. Further we investigate a simulation performed with the Nonhydrostatic ICosahedral Atmospheric Model (NICAM, Satoh et al. (2008), Satoh et al. (2014)), jointly developed at the Japan Agency for Marine-Earth Science and Technology, the Atmosphere and Ocean Research Institute, the University of Tokyo, and the RIKEN Advanced Institute for Computational Science, in Japan. We took the chance of analyzing also a simulation that accompanied the measurement campaign *NARVAL2*. As SLAM this simulation uses the ICON model, but here in a numerical weather prediction setup with a domain located in the tropical Atlantic. Both, ICON and NICAM, use icosahedral grids and a non-hydrostatic dynamical core, and are capable of performing simulations on a large variety of grids.

ICON - Spherical Limited Area Models

The domain of ICON-SLAM is a sphere with a scalable radius. By the choice of this scaling the domain area and, in combination with the choice of model grid, the grid spacing are affected. A similar modeling approach has been undertaken by Reed and Medeiros (2016). They used a range of scaling factors (1 - 1/16) and by that outlined the transition from global RCE to cloud-resolving RCE. For our study we aimed to simulate tropical convection up to its largest characteristic scales, given by large-scale circulations such as the Hadley Cell. Thus we chose the radius to be an eighth of the Earths, resulting in a circumference of 5004 km and an area of $\sim 8 \times 10^6\,\mathrm{km}^2$. Note also that the scaling does not affect the curvature of the spherical domain, which does not exist due to the model equations using a *shallow atmosphere approximations*. The bottom boundary contains no orography and only water at fixed (sea) surface temperatures (SSTs), with the profile *Qobs*, designed for Aqua Planet Simulations (Neale and Hoskins, 2000a;b). There is no planetary rotation and thus there are no baroclinic or equatorial waves. We use a zonally symmetric but meridionally varying solar insolation, which pulsates with a diurnal cycle. In this way, we constructed a zonally symmetric, idealized model of tropical dynamics.

We performed three simulations using ICON-SLAM, that was introduced in Chapter SLAM. hiSLAM was conducted on an icosahedral grid with 1310720 cells and 2.5 km nominal grid spacing, a resolution typical for "deep convection permitting" models (Prein et al., 2015). The other two simulations were performed on a grid of 20480 cells with 20 km nominal grid spacing (coSLAMs), one of them (coSLAM-pc) with the use of the Nordeng cumulus convection parameterization scheme (Nordeng, 1994), the other without (coSLAM-xc). All simulations share a stretched, vertical grid with 95 levels and the model

top is at 83 km. Also the integration time step is equal for all experiments and set to 20s. Rayleigh damping Klemp et al. (2008) is applied for the levels in between 50 to 83 km height for preventing wave reflection at the model top. The output frequency is 15 minutes for 3D variables and 5 minutes for 2D variables. The integration period is 90 days for hiSLAM and 150 days for coSLAMs. For spectral analyses we interpolated the model output onto Gaussian grids, with grid spacing of 4.88 and 39.1 km at the Equator, for hiSLAM and coSLAMs, respectively.

NICAM - ICSOM1

For the Interhemispheric Coupling Study by Observations and Modeling (ICSOM, see http://pansy.eps.s.u-tokyo.ac.jp/icsom/) a combination of observations and NICAM model simulations is used. The simulation investigated here is performed on a global domain, defined on a icosahedral mesh with 14 km grid spacing, and covers the time period from 31/01/2016 to 06/02/2016 0000UTC. The vertical grid consists of 128 levels and the model top is at 38 km. Moist processes are explicitly calculated using a single-moment bulk cloud microphysics scheme (Tomita, 2008), and no cumulus convection parameterization scheme is used. In NICAM's dynamical core, as used for the ICSOM1 simulation, there are two kinds of numerical diffusion schemes (linear and non-linear) used to handle computational instability (Satoh et al., 2008). These diffusion operators also efficiently damp waves towards the model top and no explicit sponge layer is required. The Mellor-Yamada-Nakanishi-Niino level-2 turbulent scheme (Mellor and Yamada, 1982; Nakanishi and Niino, 2006; Noda et al., 2010) is applied as a parameterization of atmospheric turbulent processes. The model atmosphere was initialized using interpolated ERA-Interim data and sea surface temperatures were given by an interpolation of NCEP final analyses surface temperature. The simulation was run on the Earth Simulator at JAMSTEC. The analyses presented in this paper focus on a region covering the tropical Pacific, from 120°E to 80°W and from 30°S to 30°N (number of grid points: $1138\times426=484788$, area covered: 17791 km$\times$6671km=119×10^6 km^2). All variables are output every 15 minutes.

ICON - NARVAL2

For the NARVAL2 campaign a wide range of airborne and ground-based measurements were taken and complemented with high-resolution numerical model simulations, using ICON (see also Klocke et al. (2017)). Different to ICON-SLAM simulations, the DWD physics package is used, with parameterizations of radiative transfer, sub-grid scale orography and microphysics. There is no parameterization of convection or non-orgraphic gravity waves in use. While SLAMs and NARVAL2 share the diffusion schemes of their common dynamical core, unresolved turbulent fluxes are parameterized differently. For NARVAL2 the turbulence parameterization is similar to the level-2.5 scheme of Mellor and

Table 3.1.: Model Overview

Model	simulation name	grid spacing	vertical levels	model top	Integration period	output frequency 3D / 2D
ICON	hiSLAM	2.5 km	95	83 km	90 days	15 min / 5 min
ICON	coSLAM-xc	20 km	95	83 km	150 days	15 min / 5 min
ICON	coSLAM-pc (parameterized convection)	20 km	95	83 km	150 days	15 min / 5 min
NICAM	ICSOM1	14 km	128	38 km	7 days	15 min / 15 min
ICON	NARVAL2	2.5 km	75	30 km	30 × 1 day	60 min / 30 min

Yamada (Mellor and Yamada (1982) and described in Baldauf et al. (2011). We analyze simulations on a domain covering the tropical Atlantic from 15°E to 68°W and from 10°S to 20°N and an area of ∼31×10^6 km^2. The model's horizontal grid consists of 4887488 cells with a grid spacing of 2.5 km. The remap of the model grid, that we use for spectral analysis, has 3281×1161=3809241 points. The vertical grid consists of 75 levels and the model top is at 30 km. The Rayleigh damping scheme is here applied for levels above 25 km altitude. The integration period, matching that of the observations, starts 26/07/2016 and ends 31/08/2016. 3D variables are output one-hourly and 2D variables half-hourly. At each day the simulation was re-initialized with ECMWF forecasts and integrated for 36 hours. Lateral boundary conditions and SSTs origin also from ECMWF and are updated every 3 hours. We neglect the first 12 hours of each simulation, to omit numerical artifacts arising from the interpolation at initialization.

Model Summary

For our study of convectively generated gravity waves we use high-resolution models (hiSLAM and NARVAL2) and compare them to models with coarser resolutions (coSLAMs and ICSOM1). Also we are also able to analyze the impacts of a parameterization of convection, when comparing coSLAM-xc and coSLAM-pc. The idealized SLAM experiments serve to analyze the convection and CGGWs in simplified circumstances, compared to convection and CGGWs in the realistic and more complex circumstances of NARVAL2 and ICSOM1. None of the simulations uses a gravity wave drag parameterization. All simulations studied herein are summarized in Table 3.1. Figure 3.1 shows the vertical resolution in the different simulations.

3.1.2. Statistical Analysis of Clouds

In Section 3.2.2 we discuss probability distributions of vertical velocity w_{cld}, perturbation temperature T'_{cld} and latent heating rate Q_{lat} for samples of cloudy grid cells. At any
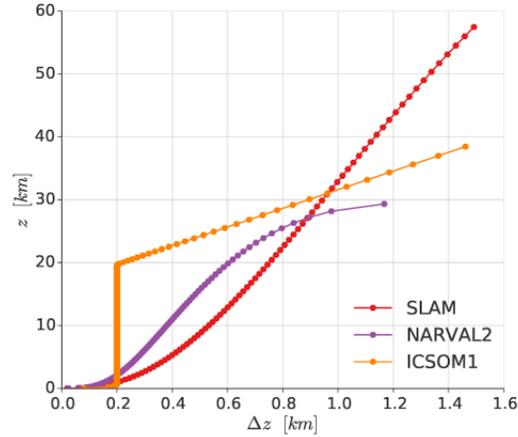
Figure 3.1.: Vertical grid spacing, Δz, with height z.

height, a grid cell is defined to be cloudy if its total cloud condensate mass mixing ratio q_{T} is greater than 0.1 g kg^{-1}.

The perturbation temperature in a cloudy grid cell with a horizontal coordinate c, at a given height z and time t is computed as

$$T'_{\mathrm{cld}}(c,z,t) = T_{\mathrm{cld}}(c,z,t) - \bar{T}(z) \tag{3.1}$$

, with $\bar{T}(z)$ denoting the mean at level z over all grid cells and over time.

The probabilities presented in Figures 3.6, 3.7 and 3.8 are computed through binning the respective quantity as for a histogram, with a normalization given through the absolute number of cloudy cells of each level. Thus the sum of each level's probabilities equals 1 (100%). The bin size is the same for all simulations: $0.1\mathrm{ms}^{-1}$ for w_{cld}, $\frac{1}{3}\mathrm{K}$ for T'_{cld} and $\frac{1}{3}10^{-3}\mathrm{Ks}^{-1}$ for Q_{lat}. The bin size in the vertical is 150 m, given by an interpolation from the stretched vertical grid of the model onto a uniform vertical grid.

To the probability distribution we add the mean vertical profile. Further we show the temporal means of the 10th and 90th percentiles, and of the minima and maxima, of each level. Their respective spreads give an estimate of the quantity's variability within a cloud.

3.1.3. Spectral Analysis

We investigate gravity wave characteristics by means of spectral analysis. The spectral power P estimates the variance of a variable, like vertical velocity $w(x,t)$ (x being the zonal coordinate and t being time), in spectral space of zonal wavenumber k (or zonal wavelength λ) and frequency ω. It is given by the product of the discrete Fourier transform $F_w(k,\omega)$

of w with its complex conjugate $F_w{}^*(k, \omega)$. In general it reads as

$$P_{ww}(k, \omega) \; = \; F_w(k, \omega)F_w(k, \omega)^*. \tag{3.2}$$

For a co-variant property, like zonal momentum flux uw, we compute the cross-spectral power, which is given by the real part (denoted with Re) of the product of the Fourier transform of u times the complex conjugate of the Fourier transform of w:

$$P_{uw}(k, \omega) \; = \; \mathrm{Re}(F_u(k, \omega)F_w(k, \omega)^*). \tag{3.3}$$

The finite character of our time series and non-cyclic lateral boundaries (NARVAL2 and ICSOM1) introduce biases to the periodogram. These we reduce with a split-cosine taper, covering an eighth of each side of the time series, as well as of the zonal dimension. To reduce the uncertainty of the periodogram in time, we smooth the spectra using the "Chunk Spectral Estimator", i.e. subdividing the time series into subsamples, so-called chunks, and taking their average. Further the chunks are overlapping by half of their length, meaning that we use every time step in our spectral analysis twice. Along with the time periods used for spectral analyses, the number of chunks used is given in Table 3.2. We average all spectra over zonal bands, ranging from 10°S to 10°N for SLAMs and ICSOM1, and from 5°N to 15°N for NARVAL2, accounting for the location of the ITCZ. Thus the spectra are averaged over 8 parallels for coSLAMs, over 58 for hiSLAM, over 142 for ICSOM1 and over 400 for NARVAL2. Note that the scaling applied to the radius of SLAMs means also a reduction of the meridional length in SLAMs, when compared to NARVAL2 and ICSOM1. The meridional variation of the circumference is considered through multiplying the spectrum of each zonal band by the cosine of latitude.

The wavenumber-frequency spectra presented in Section 3.3.2 are computed from two-dimensional discrete Fourier Transforms, following Equation 3.3. They are normalized for the simulations' respective maximum value, as we are interested in their characteristics in a qualitative sense.

For testing the gravity wave spectra for their universal properties we use one-dimensional spectra, in zonal wavenumber and frequency space (Section 3.3.1), as well as in vertical wavenumber space (Section 3.3.3). The one-dimensional discrete Fourier Transforms are computed, either in the zonal dimension, with an average over time, for a zonal-wavenumber spectrum, or in time with an average over all zonal grid points, for a frequency spectrum. For spectra of zonal momentum flux uw, we take the absolute value of the cross-spectral power, as it can take negative values. We then compute the power spectral density, p, accounting for the sample length in space/time and its resolution, as well as for the mean air density at the respective altitude.

For spectra in vertical wavenumber space we interpolated the model output onto a linearly spaced vertical grid (from 15 km to 55 km for SLAMs, to 27.5 km for NARVAL2

Table 3.2.: Time periods used for cloud statistics and spectral analyses.

simulation	Cloud Statistics - Figures 3.6, 3.7 and 3.8	Zonal Wavenumber Spectra - Figures 3.9 and 3.10	Wavenumber-Frequency Spectra - Figure 3.11	Frequency Spectra - Figure 3.10
hiSLAM	271 time steps	[20;90] days	[20;90] days / 10 chunks	[20;90] days
coSLAM-xc	1098 time steps	[10;150] days	[10;150] days / 20 chunks	[20;150] days
coSLAM-pc	1098 time steps	[10;150] days	[10;150] days / 20 chunks	[20;150] days
ICSOM1	-	[0;6] days	[0;6] days / 0 chunks	[0;6] days
NARVAL2	72 time steps	[0;30] days	[0;30] days / 4 chunks	[0;30] days

and 38 km for ICSOM1), which then allows for the computation of Fourier transforms. The non-cyclic character of the vertical profile requires tapering and the three smallest wavenumber, due to their biases, are excluded. Also an average is taken over a large sample of columns. The normalization for power spectral density is equivalent to that of the other one-dimensional spectra.

3.2. Tropical Dynamics and Convection

In this section we describe the general characteristics of convection and dynamics of the simulations. In subsection 3.2.1 we describe their mean states, as well as characterteristics of circulations and convective activity. For interpreting differences in the models' representation of convective clouds, the statistics of cloud vertical velocities, temperature perturbations and latent heating rates are analyzed in subsection 3.2.2. For estimating the thermal forcing of CGGWs and relating that to spectra of gravity wave properties in the stratosphere (Section 3.3), we present a spectral analysis of precipitation flux and upper-tropospheric vertical velocity and kinetic energy in subsection 3.2.3.

3.2.1. Circulation, Clouds and Moisture

Figure 3.2 shows the temporal and zonal means of the meridional and zonal wind, as well as of vertical velocities. The temporal and zonal means of SSTs are shown in panel (f) of Figure 3.2. For SLAMs they peak sharply at the central parallel and force deep convection there. This drives a thermally direct, overturning meridional circulation, with ascent only around the central parallel and subsidence, along with radiative cooling, towards higher latitudes. Consistent with that, a low-level convergence zone occurs along the central parallel. No zonal circulation is present in SLAMs, as planetary rotation is absent.

In ICSOM1 and NARVAL2 circulations are more complex and not symmetrical. There is stronger meridional low-level inflow from the winter hemisphere, whereas convection is more active in the summer hemisphere. In ICSOM1 and NARVAL2 an easterly trade

wind regime and a zonal circulation in the stratosphere, associated with the QBO, can be identified. The vertical velocity contours, representing vertical motion forced through convective clouds, indicate that convection is reaching higher altitudes in ICSOM1 and NARVAL2 than in SLAM simulations.

Figures 3.3 and 3.4 show snapshots of the distribution of moisture and clouds, as well as of the surface wind field, taken at the simulations' last time step. They illustrate the cloud fields of the convergence zone and the low-level flow. In hiSLAM and coSLAM-xc, where convection is treated explicitly, the convergence zone is broken up and the clouds aggregate zonally. The large-scale circulation is thus not solely given through the meridional cell, but also a zonal component of low-level inflow at the central parallel is found. This behavior is not found in coSLAM-pc, where high moisture and convection is present all along the central parallel. From this we conclude that a parameterization of convection inhibits convective self-aggregation, a result in line with Becker et al. (2017).

In ICSOM1 and NARVAL2 the ITCZ forms along the line of meridional air mass and moisture convergence and manifests in convective cloud systems of large scales in the zonal dimension. In ICSOM1 and NARVAL2 vertically integrated water vapor and cloud water condensate are notably higher, indicating a sensitivity to cloud microphysical parameterization.

Figure 3.5 (a) shows cloud cover as a function of height for SLAMs and NARVAL2. It is computed as the sum of the area of cloudy cells of each level, divided by the area of columns that contain at least one cloudy grid cell. A grid cell is defined to be cloudy, if $q_\mathrm{T} > 0.1$ g kg^{-1}. In all models the three modes of tropical convection (Johnson et al., 1999), shallow, congestus and deep convection are present. Still the models are different with respect to each other. SLAMs show two peaks at low levels below 4 km, with similar altitudes, making it hard to distinguish shallow and congestus clouds. In coSLAM-pc deep convection's anvil clouds can be identified as a sharp peak in cloud fraction at an altitude of 8 km. In hiSLAM and coSLAM-xc this peak occurs at a higher altitude and is smoother, indicating greater variability in deep convection's cloud depth. hiSLAM and coSLAM-xc have very similar profiles, suggesting that spatial resolution, in the range of 2.5 to 20km, does not matter for the vertical structure of tropical, convective clouds.

In NARVAL2 shallow and congestus clouds are clearly separated, with peaks in cloud fraction at ∼1.5 km and 5 km. There is no clear peak for deep convection's anvil clouds but a significant amount of cloud fraction reaches up to ∼14 km, confirming the presence of deep convective clouds. We find that the models with explicit convection exceed coSLAM-pc in cloud top height significantly, by about 2 km, suggesting that the depth of deep convection is reduced through the use of a parameterization.
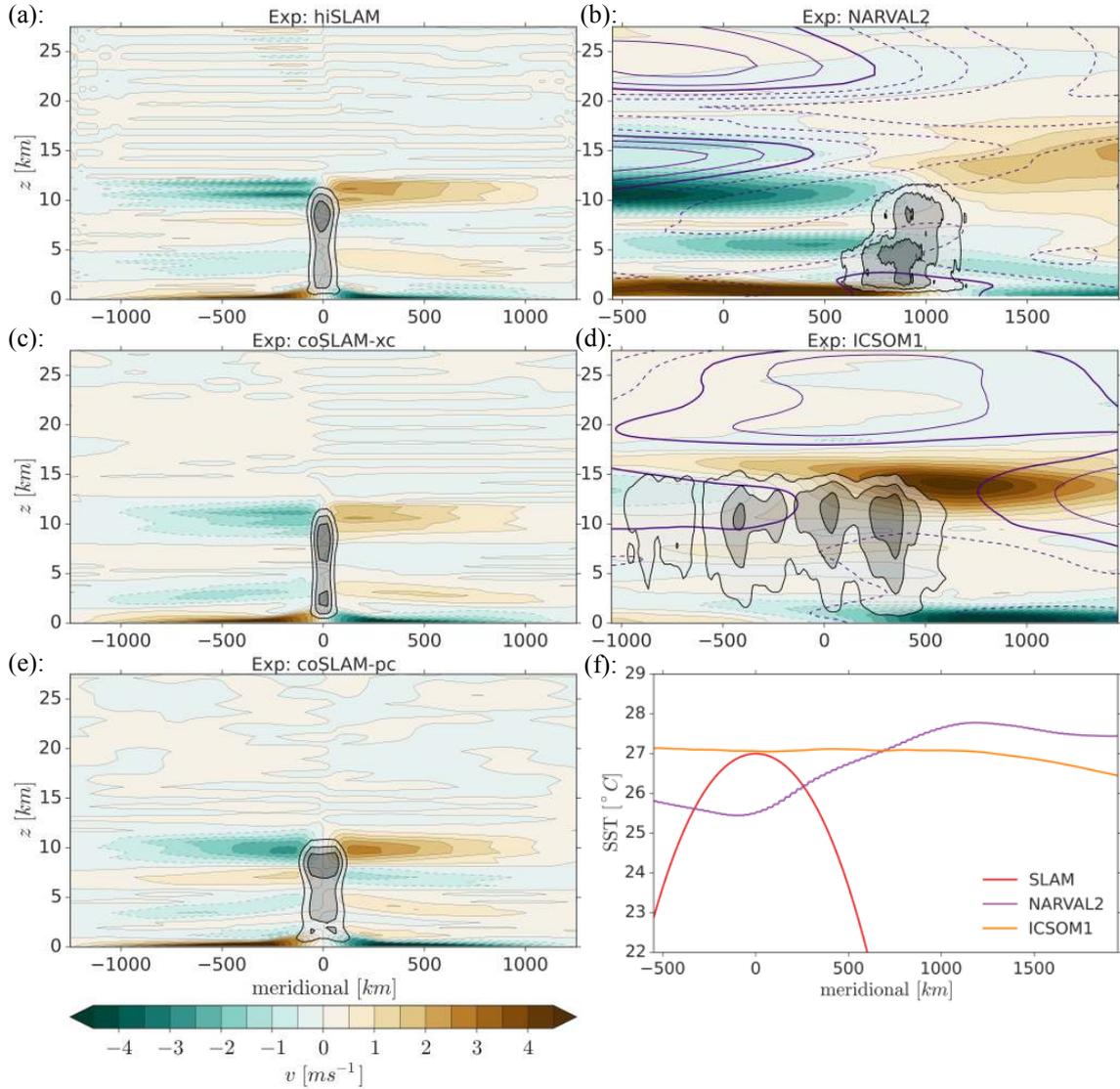
Figure 3.2.: Panels (a)-(e): Temporal and zonal mean of the meridional wind, v $[ms^{-1}]$, in colored shading, and of the zonal wind indicated by purple and vertical velocity indicated by black contours. For zonal wind, the thick solid contour indicates the zero-line, the contour interval is 5 ms^{-1} and negative values are dashed. For SLAMs this is omitted as there is no zonal circulation. The horizontal axis shows the distance in km from pole to pole, with 0 denoting the Equator in NARVAL2 and ICSOM1, and the central parallel for SLAMs. For NARVAL2 only the central part of the Atlantic, from 45°W to 20°W is considered. For vertical velocity the three contours refer to one, two and three quarter's of the simulation's maximum vertical velocity. The maxima have magnitudes of 0.08 ms^{-1} for hiSLAM, 0.02 ms^{-1} for NARVAL2, 0.08 ms^{-1} for coSLAM-xc, 0.03 ms^{-1} for ICSOM1 and 0.06 ms^{-1} for coSLAM-pc. Panel (f) shows the temporal and zonal mean of sea surface temperature (SST). For all simulations the temporal means are taken over the whole integration period.
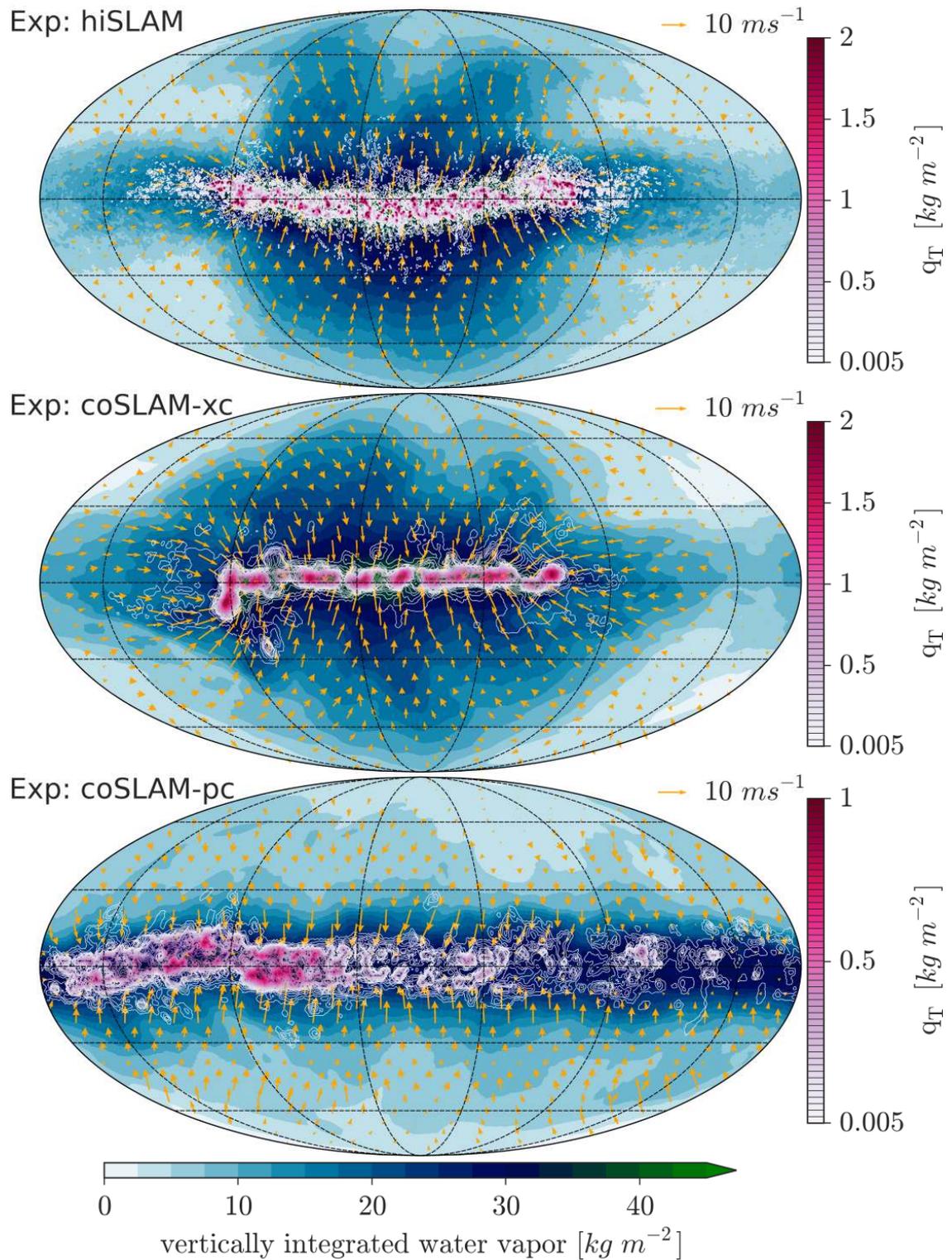
Figure 3.3.: Full domain snapshots of SLAMs at their last integration time step: Vertically integrated water vapor $[kg\ m^{-2}]$ is shown blueish filled contours, vertically integrated total cloud condensate is illustrated in white-to-pink contours with a linear spacing from 0.005 to 2 $kg\ m^{-2}$ for hiSLAM and coSLAM-xc, and to 1 $kg\ m^{-2}$ for coSLAM-pc. Orange arrows represent surface wind vectors.
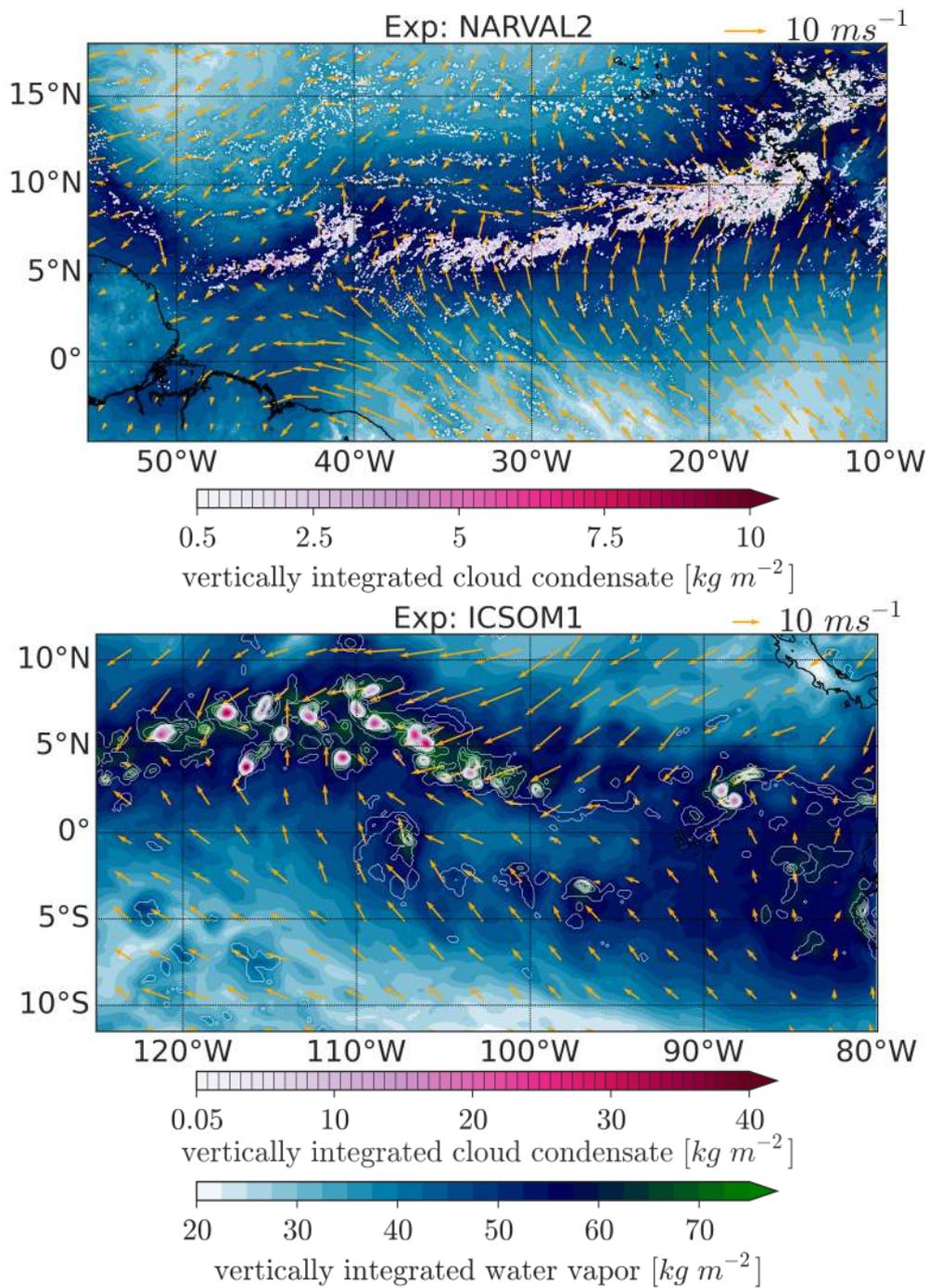
Figure 3.4.: Like Figure 3.3, but for experiments NARVAL2 and ICSOM1. The plotted areas are chosen such that their zonal and meridional extents are equal to SLAM's circumference and to its distance from pole to pole. The contours of vertically integrated total cloud condensate are linearly spaced from 0.5 to 10 $kg\ m^{-2}$ for NARVAL2 and from 0.05 to 40 $kg\ m^{-2}$ for ICSOM1.
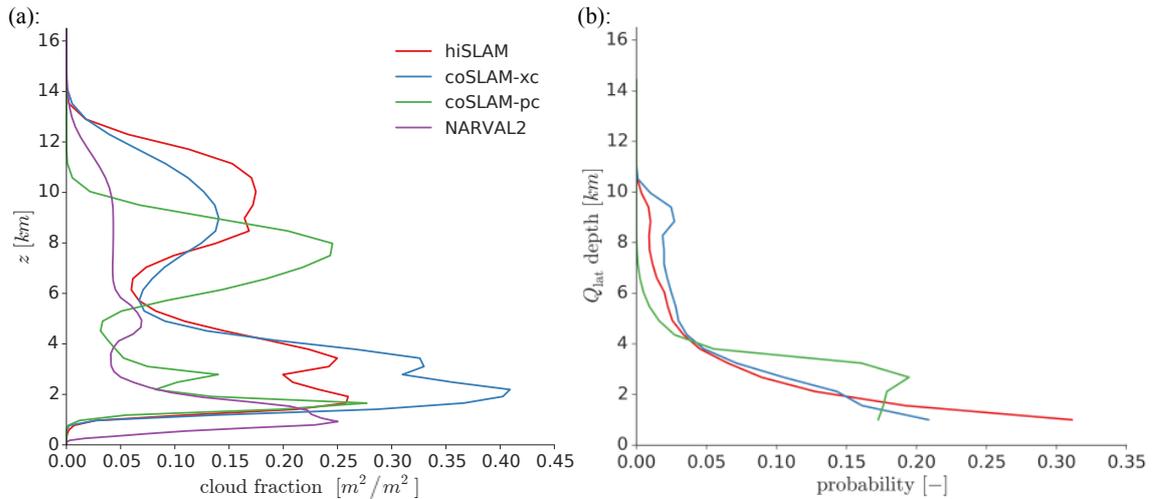
Figure 3.5.: (a): Mean vertical profile of cloud fraction and (b): the probability distribution of the latent heating depth.

3.2.2. Cloud Statistics

We here characterize the models' representation of convective clouds through a statistical analysis of their dynamic and thermodynamic properties, following the methodology described in subsection 3.1.2. In-cloud vertical velocity w_{cld}, perturbation temperature T'_{cld} and latent heating rate Q_{lat} are analyzed. These properties do not only characterize convective clouds themselves but also relate to their mechanical (w_{cld}) and thermal (T'_{cld} and Q_{lat}) forcing of gravity waves.

For the cloud statistics of SLAMs we pre-sample the model output for grid cells in between 10 degrees north and south of the central parallel. For NARVAL2 we compute cloud statistics only for the central part of the Atlantic ITCZ, from 35°W to 16.5°W, and over ocean only. We miss the variables of cloud condensate for ICSOM1, so we could not compute its cloud statistics.

Vertical Velocity

Figure 3.6 shows the probability distribution of w_{cld} for all heights, computed over several time steps.

In numerical models of explicit convection the vertical motions in convective clouds, updrafts and downdrafts, are affected by the horizontal grid spacing. We see this from the differences in magnitude of w_{cld} among the high-resolution models hiSLAM and NARVAL2 and low-resolution model coSLAM-xc. Nevertheless these three models agree on a peak in magnitude of w_{cld} at high levels above 10 km, due to latent heat release by freezing, accelerating updraft speeds still above the freezing level. In these models with explicit convection there are negative magnitudes of w_{cld} present above ∼9 km. These

reflect the oscillation of cloudy air mass around their level of neutral buoyancy, which can be interpreted as evidence for mechanical gravity wave generation. Only coSLAM-pc shows exclusively positive w_{cld} around the cloud top. The parameterization of convection parameterizes the overshooting of convective clouds beyond their level of neutral buoyancy and thus does not explicitly simulate the dynamical "overshooting" of updrafts, along with the oscillation around it. As a consequence the mechanical generation of gravity waves is expected to be inhibited by a parameterization of convection.

At lower levels negative magnitudes of w_{cld} relate to downdrafts, driven by evaporative cooling of precipitation. While hiSLAM has greater updraft velocities, downdrafts are more intense in NARVAL2.

In Figure 3.6 panel (e) the 50th, 90th and 99th percentiles of each time step at each level are shown for hiSLAM. A similar analysis was done by Khairoutdinov et al. (2009), who used a Large-Eddy-Simulation of tropical convection with a horizontal grid spacing of 100 m, also in a non-rotating framework. The statistics of hiSLAM compare well with the average updraft speeds shown in Figure 8b) of Khairoutdinov et al. (2009), both in their structure and magnitudes. For this reason we find that hiSLAM is deep-convection permitting, meaning that it, in a statistical sense, represents deep convection realistically.

Temperature Anomalies

The probability distributions of T'_{cld} as a function of height are shown in Figure 3.7. In our models clouds below the freezing level (∼6 km) are mostly colder than their environment, and only warmer above the freezing level. The cool anomalies relate to downdrafts, shallow and congestus cloud tops, while the warm anomalies represent buoyant updrafts.

The parameterization of convection used in coSLAM-pc does, in terms of the mean vertical profile, represent T'_{cld} in clouds similarly to simulations with explicit convection. However the spread of T'_{cld} is, compared to coSLAM-xc, slimmer, meaning a reduced variability of in-cloud temperature anomalies. Thus a parameterization of convection affects the dynamical representation of convection much more strongly than the thermodynamical representation.

In comparison to hiSLAM, NARVAL2 shows cooler T'_{cld} at low levels. This indicates drier low- and mid-level environmental conditions and inversion layers, causing more evaporation and cooler downdrafts, along with a greater variety of lifting mechanisms. At ∼5.5 km, where cloud fraction shows a local maximum (see Figure 3.5 (a)), the mean of T'_{cld} turns positive and there is a localized increase in variability, both in the positive and negative. The mean of T'_{cld} stays positive up to ∼12 km. Above that overshooting tops and radiative cooling cause clouds being cooler than their environment again.

Both, hiSLAM and NARVAL2 differ from coSLAMs in that T'_{cld} does not converge towards the cloud tops. Instead the spread of the distribution of T'_{cld} widens there. We interpret this signal, like for w_{cld}, as gravity waves and oscillations around the level of

Figure 3.6.: Panels (a)-(d): Probability distributions of w_{cld} as a function of height. The mean is shown by the red line, the time-mean of the minimum and maximum are shown in yellow and the time-mean 10th and 90th percentiles are shown in orange lines. Panel (e) shows the 50th, 90th and 99th percentiles of each time step of hiSLAM's probability distribution of w_{cld}.

Figure 3.7.: Panels (a)-(d): Probability distributions of T'_{cld} as a function of height. The mean is shown by the red line, the time-mean of the minimum and maximum are shown in yellow and the time-mean 10th and 90th percentiles are shown in orange lines.

neutral buoyancy.

Latent Heat

Latent heating in clouds is used in current gravity wave parameterizations as a measure of convective activity in order to compute gravity wave drag (Richter et al., 2010). Cloud microphysical parameterization estimate the heat release of the relevant processes, condensation, evaporation and freezing. A parameterization of convection, as used in coSLAM-pc, introduces a heating tendency that adds to the latent heating.

The probability distributions of latent heating rates Q_{lat} are presented in Figure 3.8. For hiSLAM and coSLAM-xc the mean of Q_{lat} peaks at ~ 6 km, which is approximately the freezing level. Also for coSLAM-pc a local maximum appears there. At higher levels the models behave similarly. Only in hiSLAM we find cooling above ~ 6 km, which can be explained by the melting of cloud ice. In coSLAM-xc there are two spikes at ~ 1 and ~ 3.5 km. Those are expected to be caused by the under-resolved character of convection in the model, owing to the abrupt release of large latent heat of condensation once the grid cell is saturated. For all models the distribution converges towards the cloud tops. This is in line with our interpretation of the temperature perturbations at cloud tops seen in hiSLAM (Figure 3.7(a)). They do not appear to be a result of latent heating, but rather of an vertical oscillation of overshooting tops or gravity waves.
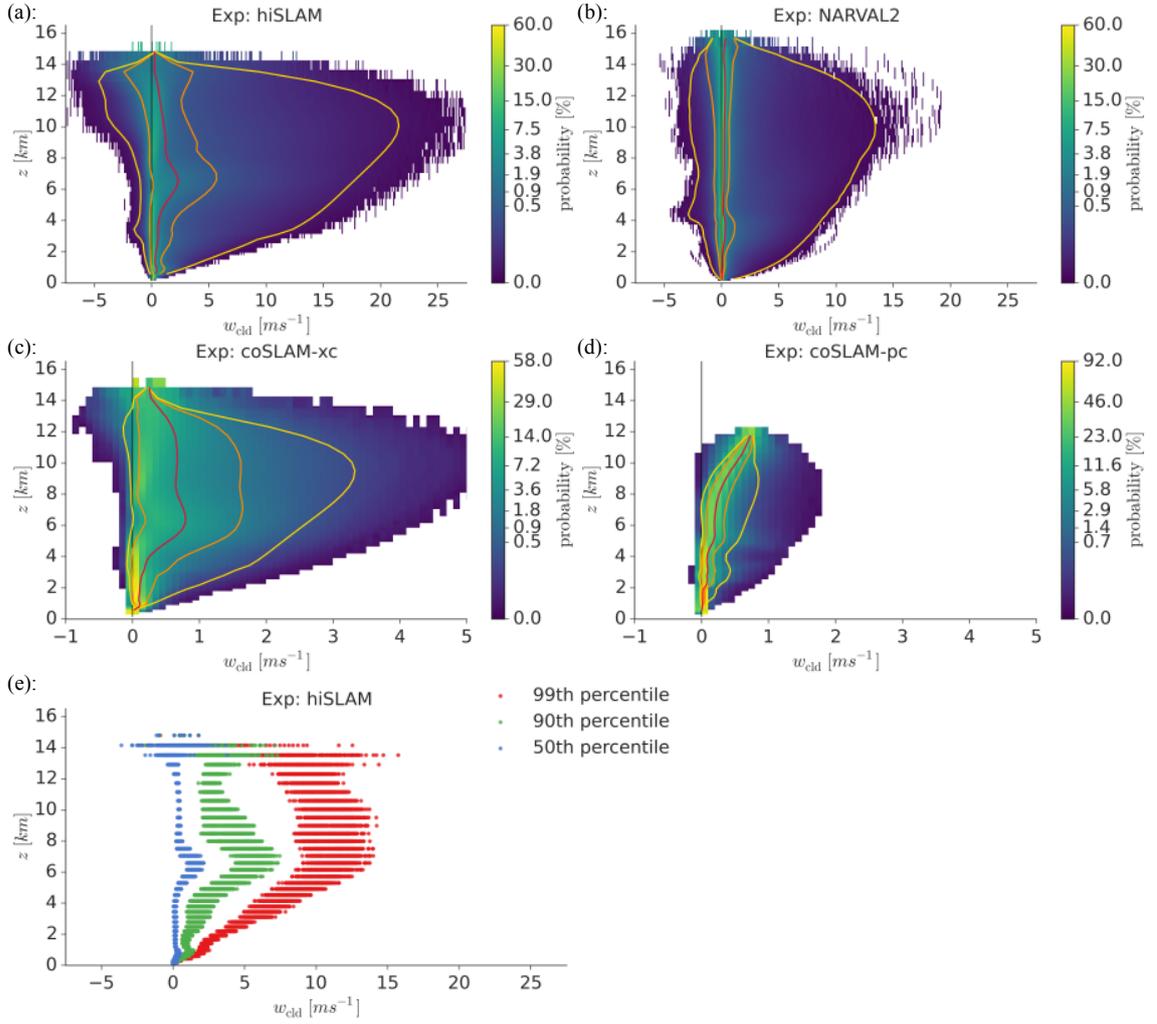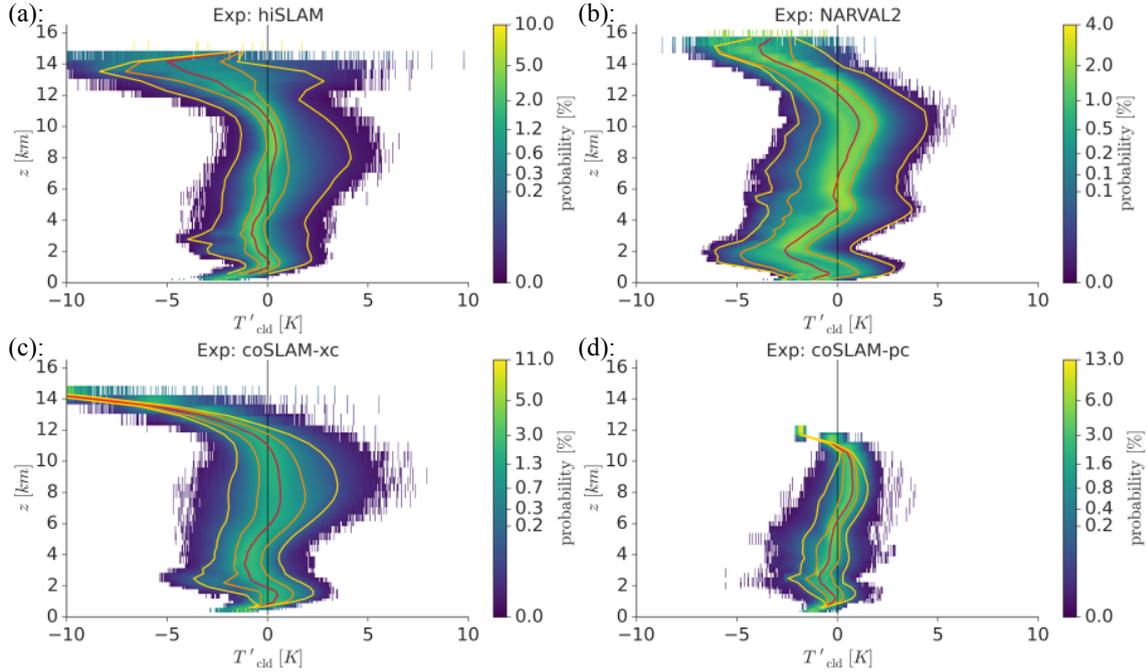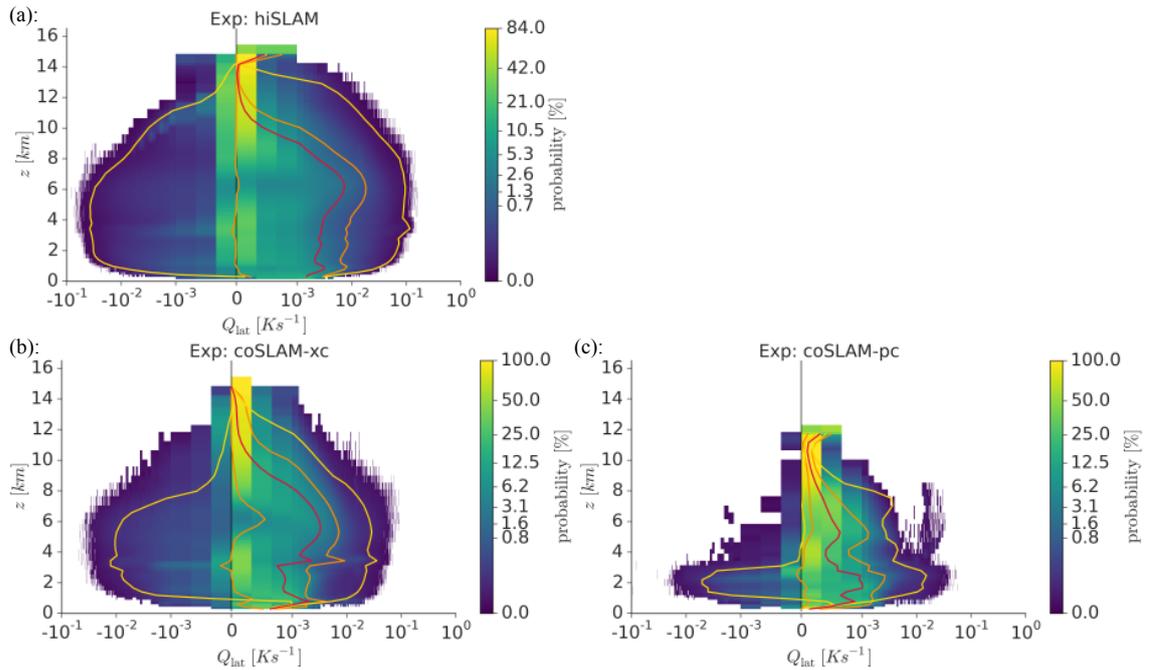
Figure 3.8.: Panels (a)-(c): Probability distributions of Q_{lat} as a function of height. The mean is shown by the red line, the time-mean of the minimum and maximum are shown in yellow and the time-mean 10th and 90th percentiles are shown in orange. Note that the x-axis is only linear within $\pm 0.001 \ K \ s^{-1}$ and logarithmic everywhere else.

In coSLAM-pc the spread of the probability distribution and the magnitude of Q_{lat}, in terms of its mean and its time-mean maximum, is less than in the models with explicit convection, in particular for altitudes greater than 3 km.

We see from the vertical profiles of the time mean and of the time means of the 90th percentile and maximum, that the latent heating is stronger in hiSLAM than in coSLAM-xc. Thus the latent heating, as expected, correlates with the updraft velocities shown in Figure 3.6, where we also find that hiSLAM is more intense than coSLAM-xc.

We will further examine the spatial variability of latent heating through a spectral analysis of its proxy precipitation (see subsection 3.2.3).

3.2.3. Spectral Analysis of Precipitation Flux, Vertical Velocity and Kinetic Energy at 9.5km

In the tropics precipitation is a natural proxy for deep convective clouds, as these precipitate and produce the most of it. Thus precipitation fits well for discriminating between deep convection, the main source of CGGWs, and non-precipitating shallow convection. Furthermore, precipitation is proportional to the net heating of a cloud, and thus also estimates the thermal forcing of gravity waves.

In Figure 3.9 panel (a) the zonal wavenumber spectra of precipitation flux defined

as the mass of precipitation per unit area and time, is shown. hiSLAM and coSLAM-xc are similar, for scales commonly resolved. Compared to them, coSLAM-pc misses a lot of variance for common scales and shows a steeper spectral slope. ICSOM1 and NARVAL2 exhibit larger precipitation flux variance than SLAMs, which is consistent with their greater magnitudes of vertically integrated water vapor and cloud water. Only hiSLAM contains more variance for scales smaller than 20 km. For all models but coSLAM-pc, the zonal wavenumber spectrum of precipitation flux is flat until scales at which numerical diffusion sets in.

Figure 3.9 panel (b) shows the zonal wavenumber spectrum of vertical velocity at 9.5 km. Through the buoyancy force, the latent heating and vertical motion in the tropical troposphere are intrinsically coupled. For this reason the similarities in their spectra are not surprising. Unlike the spectrum of precipitation, the vertical velocity variance of hiSLAM here exceeds that of NARVAL2. This is another indication for the high intensity of updraft velocities in hiSLAM and for the efficient translation of heating into vertical motion in the absence of a background flow.

We will refer back to these spectral properties, that characterize the forcing of gravity waves, to explain differences among the simulations' spectra of gravity wave momentum flux in the stratosphere (see subsection 3.3.1).

For upper-tropospheric kinetic energy a spectral slope proportional to $k^{-5/3}$ was proposed for tropical dynamics (going back to Kraichnan (1967)), where the flow is mostly divergent, and has been confirmed in observations (Nastrom et al., 1984) and numerical model studies (e.g. Koshyk and Hamilton (2001)). Figure 3.9 panel (c) shows the power spectral density of kinetic energy in zonal wavenumber space at altitudes of ∼9.5 km. The characteristic spectral slope is reproduced by all models except hiSLAM, for the scales unaffected by numerical diffusion. We find that hiSLAM's spectrum is flatter than $k^{-5/3}$ and thus contains an excess of kinetic energy at small scales. Quantitatively ICSOM1 resolves the least kinetic energy of all experiments, and coSLAM-pc resolves the least energy among all SLAMs. hiSLAM resolves most kinetic energy at scales less than ∼250 km and exceeds NARVAL2, with equal grid spacing, significantly, due to its flatter slope.

3.3. Spectral Analysis of Convectively Generated Gravity Waves

We characterize gravity waves excited by convection, as described in Section 3.1.3, by spectral analyses of gravity wave properties in the stratosphere. It is assumed that perturbations in the stratosphere relate to gravity waves that were excited by convective clouds in the troposphere.
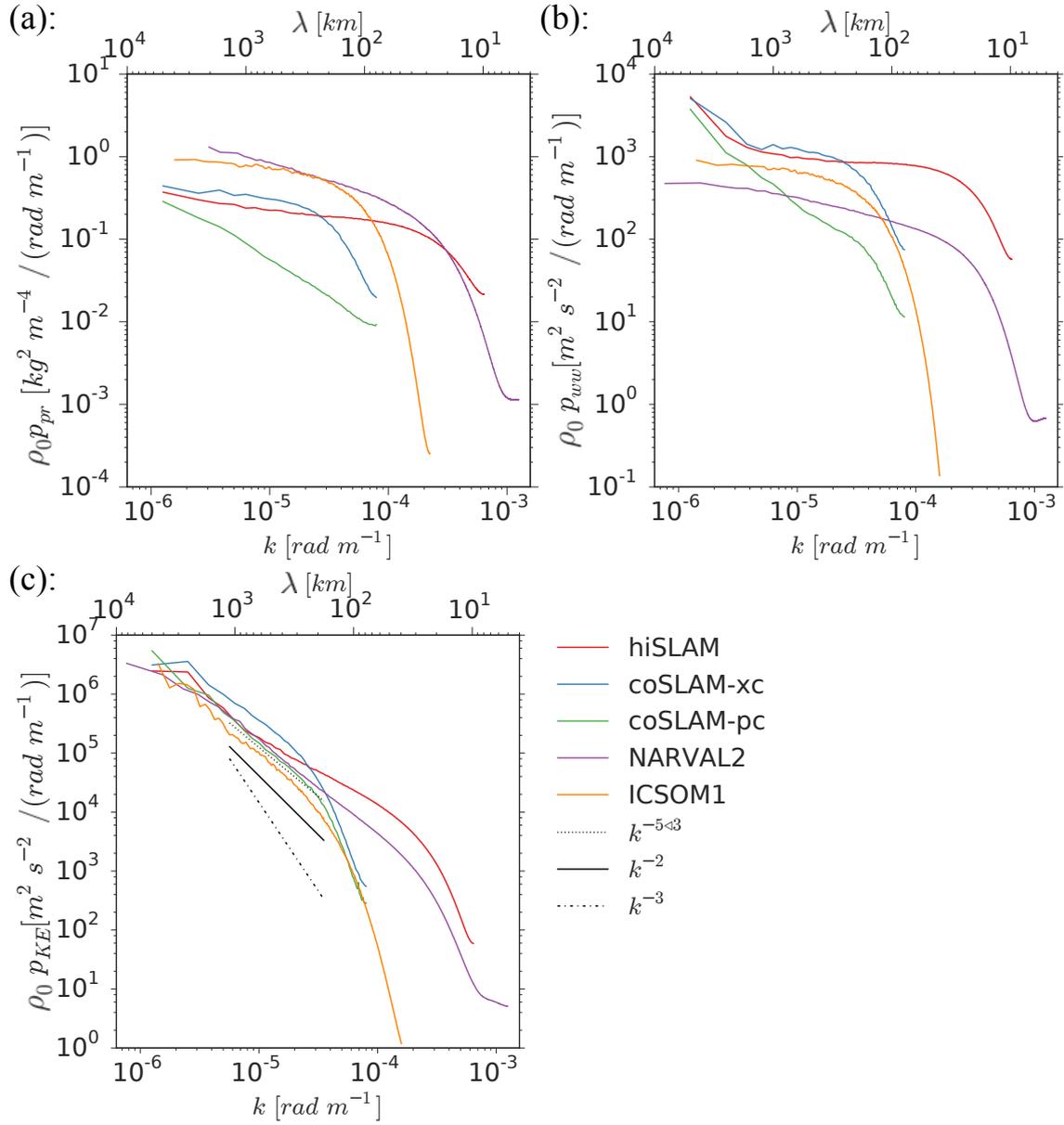
45

Figure 3.9.: Power spectral densities of (a) precipitation flux variance (b) of vertical velocity variance, ww, at ~ 9.5 km height and (c) of kinetic energy, KE, also at 9.5 km height, in zonal wavenumber space.

3.3.1. Spectra in Zonal Wavenumber and Frequency Space

Here we analyze spectra in both zonal wavenumber and frequency space, shown in Figure 3.10, of zonal momentum flux, uw, zonal velocity u and vertical velocity w in the stratosphere, that are characteristic properties of gravity waves.

Panel (a) shows the power spectral density of zonal momentum flux variance in zonal wavenumber space. At scales greater than 200 km simulations with background rotation, ICSOM1 and NARVAL2, contain more variance than SLAM models. This signal relates to equatorial waves relying on the beta effect, like Kelvin, Rossby-Gravity and inertia-gravity waves, or to baroclinic waves from midlatitudes. For scales smaller than ∼250 km, however, hiSLAM exceeds NARVAL2 in zonal momentum flux variance. The zonal momentum flux spectrum of hiSLAM flattens and becomes "white". This behavior is consistent with the results presented by Lane and Moncrieff (2008), who also find a "white" spectrum until scales at which numerical diffusion sets in. In contrast to that, for the realistic simulations, NARVAL2 and ICSOM1, and for coSLAM-xc, the zonal momentum flux spectrum has a steady slope $\sim k^{-1}$. Still a substantial amount of momentum is contained at small scales and missed by models with coarse resolution.

coSLAM-pc resolves the least zonal momentum flux of all models, also in comparison to the equivalent simulation without a parameterization of convection, coSLAM-xc. This means that a parameterization of convection affects gravity wave generation through convection and causes a reduction of momentum flux carried by CGGWs into the middle atmosphere. Zonal momentum flux controls wave mean-flow interaction in the middle atmosphere, and thus middle atmospheric circulations are expected to be affected by the use of a parameterization of convection, unless effects of parameterized convection on momentum flux are parameterized as well. A comparison to the zonal wavenumber spectra of precipitation flux, representative of net diabatic heating, and upper-tropospheric vertical velocity variance (see Figure 3.9) shows consistent correlations. It indicates that coSLAM-pc's lack in diabatic heating variance at small scales, causes not only reduced vertical velocity variance in the upper troposphere, but manifest also in the reduction of zonal momentum flux variance of gravity waves in the stratosphere.

The integration of the zonal momentum flux over zonal wavenumber space quantifies the potential forcing of the wave field onto the mean circulation. We thus in table 3.3 compare this quantity with respect to hiSLAM, for scales shorter than 1000 km. Among SLAMs we find that hiSLAM contain 10 times more absolute momentum flux than coSLAM-xc. The reduction of absolute momentum flux by a parameterization is found to be a factor of 5 when comparing coSLAM-pc to coSLAM-xc. NARVAL2 and ICSOM1 exceed hiSLAM in momentum flux at scales greater than 250 km and fall below hiSLAM at shorter scales. Thus in this analysis NARVAL2 shows slightly less and ICSOM1 more absolute momentum flux than hiSLAM.

Table 3.3.: Intercomparison of the absolute momentum flux, which is given by the integration over the zonal wavenumber space of p_{uw}. In order to neglect the influence of the large scales, we only integrate over wavelengths shorter than 1000 km. The absolute momentum flux of all simulations is divided by that of hiSLAM.

	hiSLAM	coSLAM-xc	coSLAM-pc	NARVAL2	ICSOM1
hiSLAM /	1	0.10	0.02	0.95	1.28

The frequency spectra of gravity wave momentum flux of SLAMs, shown in Figure 3.10 (b), are consistent with the zonal wavenumber spectra. The power spectral densities of coSLAM-pc are significantly weakened by its parameterization of convection. coSLAM-xc and hiSLAM show similar results down to periods of half a day. hiSLAM's spectrum is generally flat and dissipation sets in at scales shorter than an hour. The spectra of the realistic simulations, ICSOM1 and in particular NARVAL2, however do show persistent slopes, that are flatter than ω^{-1}.

In the upper troposphere the slope of zonal wavenumber spectra of horizontal velocity is proportional to $k^{-5/3}$, as shown with aircraft observations in Gage and Nastrom (1986a) and Gage and Nastrom (1986b). For the stratosphere, Gardner et al. (1993) showed, by using an analytical gravity wave model, that a wavenumber spectrum of zonal velocity is also proportional to $k^{-5/3}$ - a universal property of the gravity wave spectrum. The zonal wavenumber spectra of zonal velocity at 20 km are shown in Figure 3.10 (c). The realistic simulations, NARVAL2 and ICSOM1, as well as coSLAM-xc confirm the proposed spectral slope at all scales unaffected by numerical diffusion. For coSLAM-pc the spectrum has, as for the other spectra before, a steeper slope than $k^{-5/3}$ and is therefore unsaturated. This confirms that the forcing of CGGWs is weakened by a parameterization of convection.

For hiSLAM the spectrum has the least variance at large scales and is almost flat for scales smaller than 500 km. Lane and Moncrieff (2008) also obtained an almost flat spectrum for zonal velocity variance in zonal wavenumber space. We propose that the enhancement of small scales, as also seen in zonal momentum flux, is due to performing the spectral analysis locally above the intense and persistently organized convective system only. By that the "potential" of convection in its generation of gravity waves is revealed.

For the power spectral density of kinetic energy and zonal velocity in frequency (ω) space, associated with gravity waves, a spectral slope proportional to ω^{-2} was postulated, based upon analytical gravity wave models (Gage and Nastrom, 1985; Gardner et al., 1993). This applies for the frequency range from buoyancy frequency N to planetary rotation f. The power spectral density of zonal velocity in frequency space is shown in Figure 3.10 (d). The proposed spectral slope of ω^{-2} is reproduced well by the realistic simulations, ICSOM1 and in particular by NARVAL2. But also, for a limited part of the frequency space, the spectrum of coSLAM-xc follows this spectral slope. The spectra of hiSLAM and coSLAM-pc have again too flat and too steep slopes, respectively.

Figure 3.10 (e) shows the zonal wavenumber spectra of vertical velocity variance at 20 km. The spectra are generally flat, NARVAL2 showing an almost purely "white" wavenumber spectrum. hiSLAM even develops a peak at ∼100 km, which was also found in Lane and Moncrieff (2008). The spectrum of coSLAM-pc however has a steep slope, meaning that variance decreases towards smaller scales for the scales well-resolved. We interpret this as another manifestation of the lack of small scale variance in latent heating through convection.

The frequency spectrum of vertical velocity variance is shown in Figure 3.10 (f). The diurnal cycle and its modes can be identified clearly, in particular for coSLAM-pc. The high resolution experiments, NARVAL2 and hiSLAM, have the greatest variance here and have flat spectral slopes for the whole frequency range. However, while the variance decreases slightly towards higher frequencies for NARVAL2, it increases and develops a peak for SLAM. The coarser models show peaks in their spectra within the range of a 0.5 and 10 cpd, and are affected by numerical diffusion towards higher frequencies.

For all spectra the spatial resolution impacts not only spectra in wavenumber space but also in frequency space. This means a reduction of variance at smaller temporal scales goes along with coarsening spatial resolution and with applying a parameterization of convection.

3.3.2. Zonal Wavenumber-Frequency Spectra

Figure 3.11 shows zonal momentum flux variance in wavenumber-frequency space at a height of ∼20 km, with a decomposition of east- and westward-propagating waves, following Hayashi (1971).

hiSLAM's spectrum shows a broad and smooth lobe of slower zonal phase speeds and a sharper lobe of faster phase speeds, which both represent prevailing gravity wave modes. This shape is again consistent with the equivalent spectrum presented in Figure 8 of Lane and Moncrieff (2008). coSLAMs, limited through their coarser resolution at shorter wavelengths, are also limited in their variance at higher frequencies. This is particularly true for coSLAM-pc, a result which was found in Section 3.3.1 already. Nevertheless for both, coSLAM-xc and coSLAM-pc, two prevalent gravity wave modes can be anticipated from the spectra's two-lobe structure.

For all SLAM simulations the zonal wavenumber-frequency spectra are symmetric around the zonal mean, as expected due to the absence of a zonal circulation and vertical shear. Thus their net wave forcing on the background zonal flow is zero.

The structure of two lobes is also reproduced in ICSOM1, and the spectrum is quite symmetric with respect to eastward and westward propagating waves, similar to those of the idealized SLAM simulations. This is because the mean background zonal wind, $\bar{u}$, is weak at this altitude (~ 1.5 ms^{-1}).
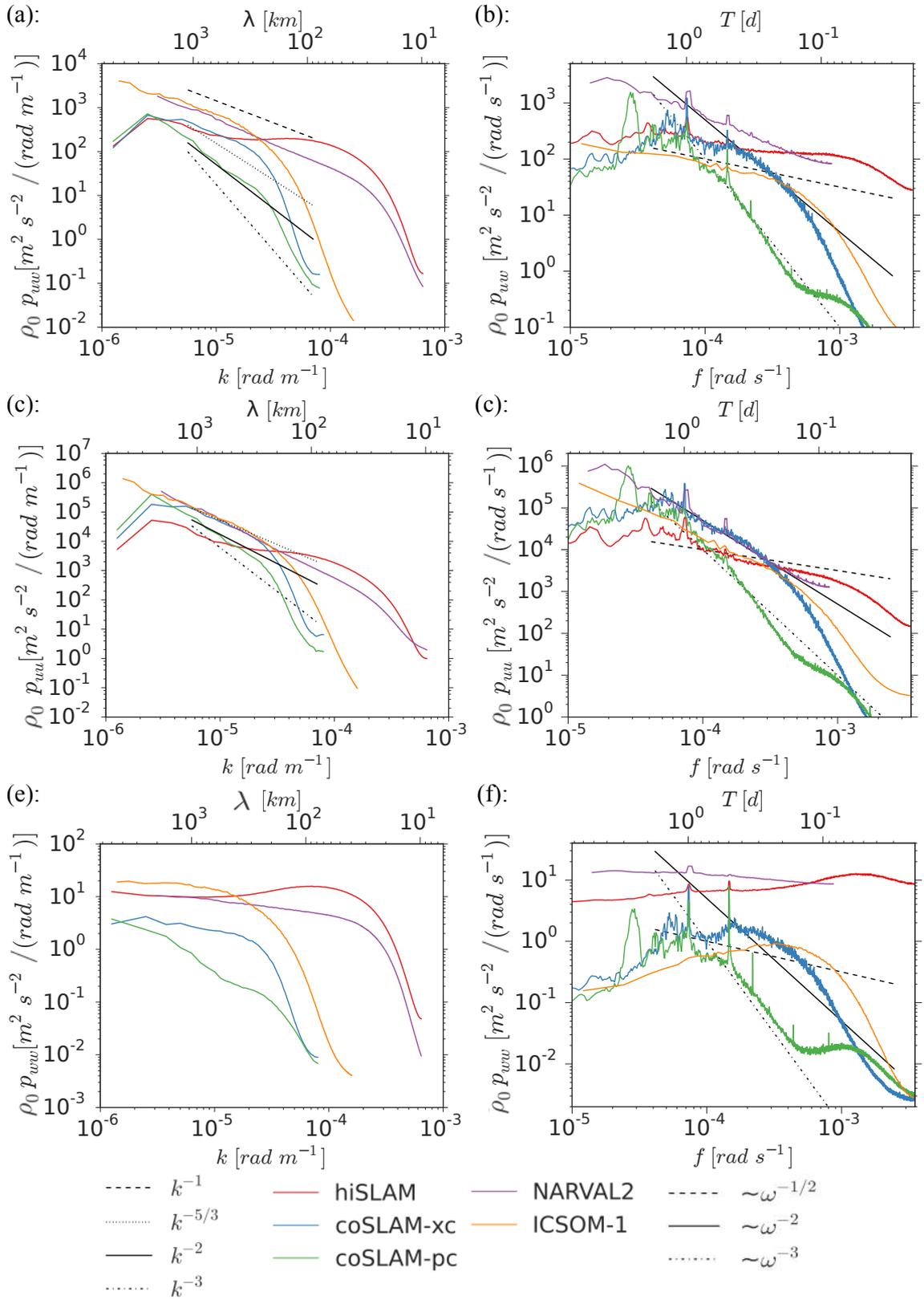
Figure 3.10.: Power spectral densities of (a and b) zonal momentum flux, uw, (c and d) zonal velocity variance, uu, and (e and f) vertical velocity variance, ww at ~ 20 km height. Panels on the left side show the spectra in zonal wavenumber space and panels on the right side in frequency space.

The spectrum of NARVAL2 however shows strong asymmetry. This indicates a zonal background flow, which is on average $\sim$-18 ms^{-1}, and which interacts with and filters the propagating waves. Only fast waves, with zonal phase speeds greater than the background flow, propagate westward. The mean background flow can be seen in Figure 3.2 (b) and layers with strong vertical shear can be identified in the lower stratosphere. The two lobes seen in all other models' spectra can not be identified.

Panel (f) in Figure 3.11 shows the variance of zonal momentum flux as a function of intrinsic zonal phase speed, $\hat{c}_p$, and vertical wavelength, λ_z, following Beres et al. (2002). Although our models are based on non-hydrostatic primitive equation, here we use the gravity wave dispersion relation in Boussinesq-Approximation, given as

$$\hat{\omega}^2 = \frac{N^2 k^2}{k^2 + m^2} \tag{3.4}$$

with a Brunt-Väisälä frequency N of 0.02 s^{-1} and k and m the horizontal and vertical wavenumbers. Assuming that $m \gg k$, Equation 3.4 simplifies to the dispersion relation for the hydrostatic case

$$\hat{\omega} = \frac{Nk}{m} \tag{3.5}$$

and c_p becomes directly proportional to λ_z and can be expressed as

$$\hat{c}_p = \frac{\hat{\omega}}{k} = \frac{N\lambda_z}{2\pi}. \tag{3.6}$$

The assumption of a Boussinesq, hydrostatic case plays a role for high-frequency gravity waves where $\omega \ll N$ and short scale gravity waves for which $m \gg k$ is not satisfied. The first relation holds as the highest resolved frequency scales with the model output frequency of 15 min. The assumption $m \gg k$ weakens the accuracy of the analysis for gravity waves of short horizontal scales. Despite compromising on accuracy we still present this analysis as it allows to identify vertical gravity wave modes. The credibility of deep modes may appear weak, as their scale approaches the distance from the tropopause up to the model top. However, we assume that there is no wave-reflection at the model top and that gravity waves are upward propagating. Further the vertical scale of gravity waves is deduced indirectly from the zonal wavenumber and frequency. With these assumption considered we expect the limited vertical domain size of the models to not play a role here.

As a result $P_{uw}(\hat{c}_p, \lambda_z)$, shown in panel (f) of Figure 3.11, exposes distinct gravity wave modes, that could also be inferred from the lobes of wavenumber-frequency spectra. All simulations show two or more vertical modes, one shallow mode with vertical scales between 3 and 6 km, and larger modes with vertical wavelengths of up to 20 km.

Salby and Garcia (1987) showed, that through the projection response, the dominant

vertical wavelength is expected to be equal to twice the vertical scale of latent heating. Figure 3.5 (b) shows the distribution of the depth of latent heating. It is computed for each column as the sum of heights of cells where $Q_{\mathrm{lat}} > 1 \times 10^{-5}\mathrm{Ks}^{-1}$. It can be seen that heating depths are mostly shallow, like the profile of cloud fraction suggests (see Figure 3.5 (a)). However, although coSLAM-pc has a great fraction of high clouds, its heating depths are limited in their vertical scale and very rarely exceed 6 km. hiSLAM and coSLAM-xc have a significant fraction of columns with deep heating (>8 km). In particular coSLAM-xc shows a peak of heating depths with a scale of ~9 km. These two characteristics, coSLAM-pc's lack of deep heating and coSLAM-xc's peak in deep heating, project onto their prevalent vertical gravity wave modes, shown in panel (f) of Figure 3.11. For coSLAM-pc a vertical mode with a peak at ~7 km is dominant, and no deeper modes exist. This corresponds well to the distribution of heating depths, with the peak at ~3 km being, as proposed by Salby and Garcia (1987), half of the vertical scale of the prevalent gravity wave mode, with a scale of ~6 km. The same relation holds for the deep mode of heating in coSLAM-xc. Its scale of ~9 km projects exactly onto a deep gravity wave mode, that can be identified as a peak at ~18 km. The distribution of heating depths of hiSLAM is more homogeneous, and thus the response in deep vertical gravity wave modes is not as pronounced as in coSLAM-xc. hiSLAM shows a particularly broad shallow mode, with a peak at a vertical wavelength of ~3 km.

For ICSOM1 we identify three dominant modes, one shallow mode at ~5, a medium mode at ~10 and a deep mode at ~19 km. Unfortunately we can not put these into relationship with heating rates.

NARVAL2 only has a shallow dominant gravity wave mode with a scale of ~4 km. This seems to be consistent with the vertical profile of cloud fraction, that shows a great amount of shallow convection and thus suggest mostly shallow latent heating.

Although the projection response of Salby and Garcia (1987) can be identified in SLAMs, it has to be considered, that Holton et al. (2002) showed, that the relation of diabatic heating and the vertical scale of the gravity wave response is dependent upon all spatial and temporal scales of the heating. We will look further into this matter by vertical wavenumber spectra, presented in the following section 3.3.3.

3.3.3. Vertical Wavenumber Spectra

Here we investigate the vertical wavenumber (m) spectra of gravity wave properties zonal velocity u, temperature anomaly T' and vertical velocity w. For horizontal velocity and temperature anomaly a spectrum proportional to m^{-3} was observed (by Tsuda et al. (1989), and recently Zhao et al. (2017), Zhang et al. (2017a), Zhang et al. (2017b)). This was explained by the saturation of gravity waves and was confirmed in simple gravity wave models that, within the scales of the saturated regime, yielded a spectrum equal to
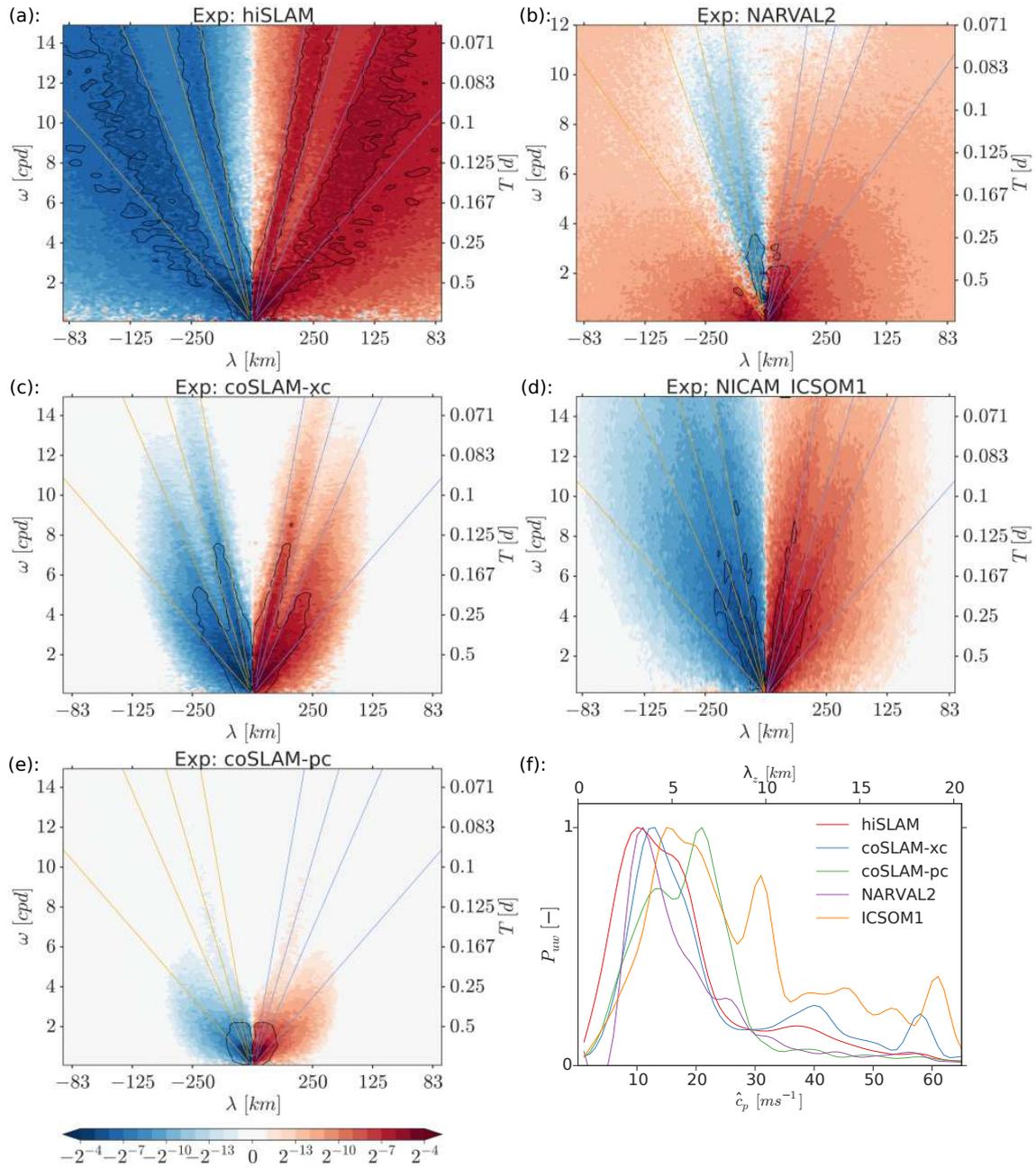
Figure 3.11.: Panels (a)-(e): Cross-spectral power of zonal momentum flux, P_{uw} $[-]$, normalized by its maximum value, in zonal wavenumber-frequency space at ~ 20 km height. Black contours in panels (a)-(e) indicate variance higher than that of a smoothed background and thus highlight gravity wave modes. Blue and orange lines display the linear gravity wave dispersion relation (see Equation 3.4) of constant horizontal phase speeds. The flattest line refers to a magnitude of 10 ms^{-1}, and the steeper lines to 20, 30 and 50 ms^{-1}. Panel (f): $P_{uw}[-]$ as a function of intrinsic zonal phase speed, $\hat{c}_p$, and vertical wavelength, λ_z.

$\frac{N^2}{6m^3}$ (Dewan and Good (1986), Weinstock (1985a), Smith et al. (1987)), with N being the buoyancy frequency. The dominant vertical mode can be identified as the wavenumber of the peak of the spectrum, separating the unsaturated from the saturated part of the spectrum. For scales smaller than the buoyancy wavenumber, the spectrum is governed by turbulence and follows a spectral slope of $m^{-5/3}$. In numerical models the vertical resolution was found to play a role in the representation of gravity waves in the middle atmosphere (Watanabe et al., 2015). For this reason the models' vertical grids, shown in Figure 3.1, have to be considered. In Figure 3.12 the vertical wavenumber spectra of zonal velocity u (panel (a)) and temperature anomaly T' (panel (b)) are shown.

For hiSLAM the expected spectrum of $p_{uu}(m) = \frac{N^2}{6m^3}$ is reproduced in the wavelength range from 2 to 5 km. coSLAMs both do not reproduce this, with too steep slopes and too little variance at short vertical scales. The same holds for the spectrum of $p_{T'T'}(m)$, with only hiSLAM reproducing a spectral slope proportional to m^{-3}. Dominant vertical gravity wave modes are expected to show up as peaks of the spectra. For hiSLAM and coSLAM-xc we here find in both spectra the dominant wavelengths at $\sim$15 km, which is the mode excited by deep convection. For coSLAM-pc the spectra have peaks at a wavelength of $\sim$5 km. Both is consistent with the dominant modes deduced from zonal wavenumber-frequency spectra in Section 3.3.2: coSLAM-xc has a deep mode, that is more pronounced than that of hiSLAM, and coSLAM-pc fails to generate a deep mode. Furthermore coSLAMs differ little in their variance at short scales. coSLAM-pc's lack in gravity wave variance, as shown in Section 3.3.1, is found in the lack of a deep gravity wave mode, and ultimately in the lack of a deep mode of latent heating. SLAM's vertical grid contains 26 levels in between 15 and 55 km, with a grid spacing ranging from 670 to 1100 m. It is the model with the highest model top and allows to robustly analyze gravity waves with scales up to $\sim$15 km by means of a spectral analysis in the vertical dimension.

ICSOM1 reproduces the spectrum $p_{uu}(m) = \frac{N^2}{6m^3}$ for vertical wavelengths from 1 to 8 km. Also for temperature anomaly variance the spectral slope is proportional to m^{-3} from 1 to 6 km. It is important to note, that ICSOM1's vertical grid has a constant spacing of 200 m between 15 and 20 km and contains 38 levels between 15 and 38 km. As such it is the model with the highest vertical resolution, allowing gravity waves with vertical scales down to $\sim$1 km to be resolved explicitly.

For NARVAL2 the expected spectrum of $p_{uu}(m) = \frac{N^2}{6m^3}$ is reproduced for vertical scales shorter than $\sim$8 km. The grid spacing ranges from 500 to 1100 m for altitudes greater than 15 km, with a model top at 30 km. As for ICSOM1, we can not identify the dominant modes deduced from zonal wavenumber-frequency Spectra (see Figure 3.11 panel (f)), due to the limited vertical extent of the model domain.

Note that the main assumption going into this analysis of vertical wavenumber spectra is that the Brunt-Väisälä frequency is constant throughout the vertical space investigated. By that that the vertical wavelength of a gravity wave would remain unaffected during
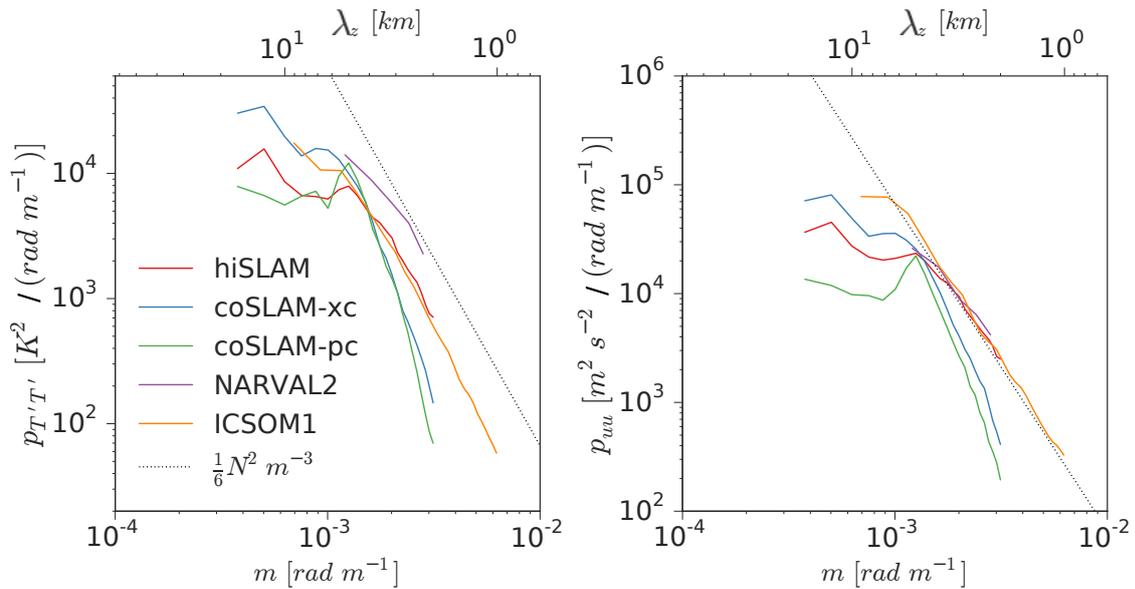
Figure 3.12.: Power spectral densities of (a) zonal velocity variance, uu, and (b) temperature anomaly variance, $T'T'$, in vertical wavenumber space.

its upward propagation. Also the effects of changing vertical grid spacing and damping layers below the model top are neglected. Still we find that the results, as indicated by the reproduction of the universal gravity wave spectrum, are robust for a limited vertical range.

3.4. Discussion

3.4.1. On modeling the universal gravity wave spectrum

Universal properties of middle atmospheric gravity waves show in one-dimensional spectral space and are summarized in Gardner et al. (1993). The saturation of the gravity wave spectrum means that, within the scales of the dominant wavenumber and buoyancy wavenumber, the power spectral density of gravity wave properties is limited by convective and shear instability criteria. In simple analytical gravity wave models, based upon only their dispersion and polarization relations, the spectral slopes were found to be proportional to power-law relations.

In table 3.4 the results of spectral analyses of our models, with respect to the reproduction of proposed spectral slopes, are summarized.

We find that the models with realistic boundary conditions, ICSOM1 and NARVAL2, yield the proposed spectral slopes in all one-dimensional spectra of gravity wave properties.

hiSLAM succeeds in producing the proposed spectra in vertical wavenumber space, where both coSLAMs appear too steep. For hiSLAM the spectral slopes, of both zonal-

Table 3.4.: Evaluation of universal spectral slopes: "v" means that the model yields the spectral slope proposed by prevalent theories. In brackets the scales of wavelengths, in units of km, are given, for which the proposed spectrum is reproduced by our models. "x-steep" and "x-flat" stand for spectral slopes steeper or flatter than the proposed spectral slope.

	$p_{KE}(k) \sim k^{-5/3}$	$p_{uu}(k) \sim k^{-5/3}$	$p_{uu}(m) \sim m^{-3}$	$p_{T'T'}(m) \sim m^{-3}$	$p_{uu}(\omega) \sim \omega^{-2}$
hiSLAM	x-flat	x-flat	v-[2;5]	v-[2;5]	x-flat
coSLAM-xc	v	v	x-steep	x-steep	v
coSLAM-pc	v	x-steep	x-steep	x-steep	x-steep
ICSOM1	v	v	v-[1;8]	v-[1;5]	v
NARVAL2	v	v	v	v	v

wavenumber and frequency spectra, are flat. We find that this result is due to applying the gravity wave analysis above the convective cluster, within +-10° latitude. It is a local and "near-field" gravity wave spectrum and thus reveals the potential of convection to generate gravity waves.

coSLAM-xc produces the proposed spectral slopes in zonal wavenumber and frequency space, for spectral scales resolved. For coSLAM-xc and coSLAM-pc the slopes in vertical wavenumber spectra are too steep, meaning that gravity waves of short vertical scale do not reach saturation. Further coSLAM-pcs spectra are generally too steep, meaning that gravity waves are weakened at short spatial and temporal scales by a parameterization of convection.

We may also note that a basic property of the analytical gravity wave model of Gardner et al. (1993) is that the spectral slopes in horizontal wavenumber space and in frequency space are proportional. This aspect we find realized in the consistently steep and flat slopes of SLAMs in zonal wavenumber and frequency space.

3.4.2. Implications of spatial resolution

The comparison of coSLAM-xc with hiSLAM allows for the investigation of the implications of increasing the grid spacing from 20 km, a grid spacing representative of a high resolution global circulation model, to 2.5km, a resolution representative of future global circulation models or current weather forecasting models. We find that the representation of convection is qualitatively consistent. In the low-resolution model (coSLAM-xc) updraft velocities lack magnitude and variance, but thermodynamically convection is very similar to the high-resolution models (hiSLAM and NARVAL2) (see Figures 3.6 and 3.7). In addition, the vertical gravity wave modes of coSLAM-xc and hiSLAM (see Figures 3.11 (f) and 3.12) have an almost equal vertical scale. The spectral analyses further show that, at the scales commonly resolved, both models have a comparable zonal momentum flux variance in the stratosphere (see Figure 3.10 (a) and (b)). However, at scales that are exclusively resolved by hiSLAM and NARVAL2, there is still a large amount of zonal

momentum flux variance; the spectral slope, as derived from NARVAL2, is almost flat ($\sim k^{-1}$) until scales at which numerical diffusion sets in. Thus, the potential gravity wave forcing still increases significantly with increasing numerical resolution. As shown in table 3.3, the absolute momentum flux of scales shorter than 1000 km is 10 times greater in hiSLAM than in coSLAM-xc. This comparison, due to the unrealistically flat slope of hiSLAM, has to be interpreted carefully. Still also NARVAL2 resolves almost an order of magnitude more absolute momentum flux and thus we conclude that the grid spacing has a great effect onto the generation of gravity waves by convection. The numerical resolution at which non-orographic gravity wave parameterizations become obsolete can not be anticipated from this work. Insight into this can be found in Preusse et al. (2008). They find that gravity waves with wavelengths shorter than 10 km are removed by vertical reflection and evanescence at their source and more prone to critical level removal. The processes of wave mean-flow interaction, such as wave breaking and dissipation, that drive circulations in the middle atmosphere involve motions of smaller scales that require even finer numerical resolution.

Still it is evident that for the representation of gravity waves in the middle atmosphere also the vertical resolution (see also Watanabe et al. (2015)) and the ratio of vertical to horizontal resolution matters. In our tests of one-dimensional spectra of zonal velocity against proposed spectra derived from analytical gravity wave models (see Figures 3.10 (c) and (d), 3.12 (a)), we for hiSLAM and coSLAM-xc find opposite results: coSLAM-xc reproduces the proposed spectral slopes for zonal wavenumber and frequency space, while hiSLAM reproduces those in vertical wavenumber space. This result suggests that the fine horizontal resolution of hiSLAM would require a greater vertical resolution. An additional experiment of hiSLAM was conducted on a vertical grid with twice the number of levels. It showed no significant differences and so we perceive hiSLAM's' vertical resolution sufficiently fine. On the other hand the vertical wavenumber spectra of hiSLAM (see Figure 3.12) show, that a high horizontal resolution helps to resolve gravity waves also with shorter vertical scales and to reach saturation for scales shorter than the dominant wavelength.

3.4.3. Implications of a parameterization of convection

The spectra of zonal momentum flux in the stratosphere, presented in Figure 3.10 (a) and (b), show that in coSLAM-pc, the only experiment using a parameterization of convection, the zonal momentum flux caused by convectively generated gravity waves is weaker by an order of magnitude at smaller wavelengths and higher frequencies than in coSLAM-xc. We find an analogy to this in a spectrum of precipitation (see Figure 3.9 (a)), representative for the latent heating and as such for the thermal forcing of gravity waves through convection. The dynamical representation of convection given through the statistics of

in-cloud vertical velocities is also inhibited and the variance of upper-tropospheric vertical velocity weakened (see Figures 3.6 (d) and 3.9 (b)). For these reasons we find that both, the thermal, and as a consequence also the dynamical forcing of gravity waves, is reduced through a parameterization of convection. As a consequence the forcing of convectively generated gravity waves onto the mean flow must be expected to be also reduced when using a parameterization of convection. We for these reasons suggest that simulations with a parameterization of convection particularly require a gravity wave drag parameterization.

In vertical wavenumber spectra of gravity wave properties, shown in Figure 3.12, we find that coSLAM-pc lacks variance at large vertical scales. This is in agreement with the distribution of heating depths, shown in Figure 3.5 (b), which shows that a deep mode in latent heating is missing for coSLAM-pc. This is true even though cloud fraction indicates the presence of deep convection, as can be seen in Figure 3.5 (a).

3.4.4. Implications of SLAMs' idealized boundary conditions

The idealizations of SLAMs are foremost the prescribed sea surface temperatures, with its steep meridional gradient, and the absence of planetary rotation. In hiSLAM (as in all SLAMs) the cloud cluster is persistently organized by the prescribed SSTs and for this reasons appears more intense than the convection within the ITCZ, as seen in NARVAL2. As shown in section 3.2.2 we find greater variability in vertical velocity and temperature anomalies at cloud tops in hiSLAM than in NARVAL2, indicating oscillations at cloud tops. Thus we propose that the flatness of hiSLAM's zonal wavenumber and frequency spectra is caused by enhanced mechanical forcing through overshooting convective updrafts.

Another factor may be planetary rotation. Horizontal wavenumber spectra in a rotating framework are generally steeper, meaning that rotation enhances the downscale cascade of energy. However, as NARVAL2 and ICSOM1 reproduce the universal gravity wave spectrum well, we find that planetary rotation in the equatorial region does hardly affect the gravity wave spectrum.

3.4.5. On convective gravity wave generation mechanisms

The generation of gravity waves through tropical convection mainly occurs as a consequence of the release of latent heat, a thermal forcing, or the vertical motion below a stably stratified fluid, a mechanical forcing.

For coSLAM-pc we see that a reduction of gravity wave momentum flux variance (compared to coSLAM-xc), occurs alongside a reduction in variance of precipitation and consequently latent heating, at the same scales. This suggests that the parameterization of convection affects gravity wave generation by misrepresenting small scale variance in latent heating. The latent heating in coSLAM-pc is also limited in its vertical scale and in

consistency with that deep modes of gravity waves are inhibited.

For the NARVAL2 and in particular for hiSLAM, we can identify oscillations at cloud tops in probability distributions of vertical velocity and temperature anomalies in clouds (Figures 3.6 and 3.7). These oscillations occur below a stably stratified layer, the tropopause, so the mechanical forcing of gravity waves is expected. Further, when looking at the zonal-wavenumber spectra of precipitation and vertical velocity, shown in Figure 3.9, we see normal behavior in precipitation, representative for the latent heating. However, we find that vertical velocity variance is flat and intense, meaning that the translation of heating into vertical motion is occurring more efficiently in hiSLAM than in other models. For that reason hiSLAM's excess of variance of gravity wave properties in the stratosphere at small scales may phenomenologically be attributed to a mechanical forcing of gravity waves.

3.5. Conclusions

In this work we present the analysis of gravity waves generated by convective clouds in several models of tropical dynamics. We show that the spectrum of stratospheric zonal momentum flux in zonal wavenumber space is almost flat, with a slope $\sim k^{-1}$, as derived from the realistic high-resolution simulation NARVAL2. The idealized model hiSLAM suggests that an even flatter spectral slope may locally be possible. In an organized convective system, the mechanical generation of gravity waves through convection is enhanced and reflected in the generation of gravity waves with relevant horizontal scales of up to 250 km. We find that only a convection-permitting resolution allows for capturing this mechanism. Thus the representation of CGGWs in atmospheric models requires either fine grid spacing or a gravity wave drag parameterization, as still a significant amount of wave forcing is contained at small scales and high frequencies.

We find that a convective parameterization inhibits gravity wave generation by convective clouds. This is found to be caused by a lack of variance in latent heating at small horizontal scales. Further, although deep convection and high clouds are present, the heating depth is generally diminished in coSLAM-pc. As a consequence no deep gravity wave mode exists and gravity wave variance is reduced for deeper vertical scales. Furthermore the mechanical generation of gravity waves appears to be inhibited. Thus the choice of a convective parameterization must be carefully considered when modeling wave-driven circulations in the middle atmosphere. For this reason we advise to turn off a parameterization of convection for simulations with grid spacings of 20km or less.

NARVAL2 and ICSOM1 show that the universal gravity wave spectrum is realized in realistic simulations of tropical dynamics, as all proposed spectral slopes of one-dimensional spectra of gravity wave properties are reproduced. The idealized models, SLAMs, also represent the universal gravity wave spectrum in several properties.

CHAPTER 4

Convective Aggregation in Idealized Simulations with SST Gradients

4.1. Introduction

Convection-permitting simulations of Radiative Convective Equilibrium (RCE) are characterized by horizontally homogeneous boundary conditions, meaning uniform sea surface temperature and insolation, and by the absence of background wind and planetary rotation. Simulations of this type have shown the emergence of a single convective cloud cluster from an initially randomly-scattered field of convective clouds, a process referred to as convective self-aggregation (e.g. Held et al., 1993; Bretherton et al., 2005; Wing et al., 2018).

Radiative feedbacks of both, the emerging dry and moist regions, were identified to be crucial for establishing and maintaining the overturning circulation that promotes and stabilizes convective self-aggregation (e.g. Coppin and Bony, 2015; Holloway and Woolnough, 2016). Through a shallow circulation, as part of the deep thermal overturning circulation associated with deep convection, convective self-aggregation is promoted (e.g. Bretherton et al., 2005; Muller and Held, 2012). This circulation was found to be driven by longwave

radiative cooling at shallow cloud tops (Muller and Bony, 2015). In general the mechanism is found to base upon an up-gradient transport of moist static energy, an advective process. However, Wing and Emanuel (2014) and Holloway and Woolnough (2016) found that the contribution of advective processes in the moist static energy budget was dependent upon the stage of the convective evolution, as to whether the aggregation was still in development or in a state of quasi-equilibrium. Of particular relevance to our study are the RCE simulations over long-channel domains (e.g. Tompkins, 2001). With such simulations multiple cloud clusters are realized and Wing and Cronin (2016) found that the domain-average moisture content, as well as that of the dry regions, was increased. They attributed advective processes, that were found to dampen moist static energy variance and by that to weaken convective self-aggregation.

We study convective aggregation in SLAMs (see Chapter 2), a convection-permitting model in RCE, under a range of different SST profiles. By using zonally symmetric but meridionally varying SSTs we aim at moving forward research on convection aggregation into both more complex and realistic conditions. Thus in our simulations boundary conditions are non-homogeneous in the meridional dimension, but they remain homogeneous in the zonal dimension. Aggregation is expected to be forced by the SST gradient in the meridional dimension, but still self-aggregation may occur in the zonal dimension, where boundary conditions are homogeneous.

This study is organized as follows. We first, in Section 4.2, introduce the models we use and motivate the SST profiles chosen. We then in Section 4.3 investigate how the SST profiles manifest in the simulations' convection evolution and in convective aggregation. In Section 4.4 we look into how, in one of our simulations with an SST gradient, a shallow circulation develops and exports moisture from the cloud cluster into originally dry regions. We then discuss the circulation in terms of its role in convective aggregation and in its relation to atmospheric rivers in Section 4.5.2. Ultimately we draw conclusions in Section 4.6.

4.2. Methods

For this study we use hiSLAM simulations, a convection-permitting model of RCE, designed for studying tropical convection, gravity waves generated by convection, and as here, the aggregation of convection. Details on the dynamical core, physical parameterizations and basic properties of the circulation and temporal evolution are given in Chapter 2. All hiSLAM simulations are conducted on the vertical grid L75T30 and on the spherical horizontal grid R2B7. The grid spacing is 2.5 km, the equatorial circumference is 5004 km and the domain area is 8 million km^2. The solar radiation incidents perpendicularly all over the domain, has a diurnal cycle and the solar constant is set to 1360.875 Wm^{-2}. The imposed solar insolation corresponds to summer conditions at the Equator. As we
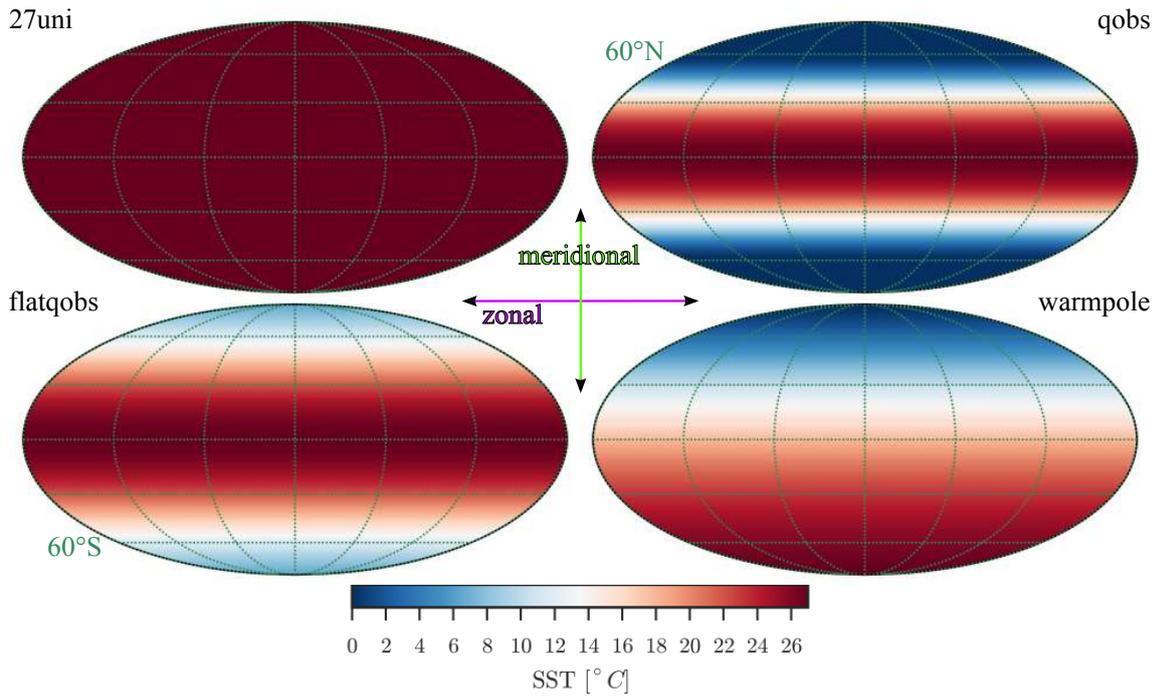
Figure 4.1.: Sea surface temperature distributions characterizing the simulations studied.

are not including oceanic heat transport, the amount of heat is larger than the one at the Equator. To obtain a realistic tropical climate, meaning radiative balance at the top of the atmosphere, the insolation would have to be reduced, like outlined in Wing et al. (2018). Since we are not interested in questions related to the equilibration of the climate, this is not an issue.

The integration period of all simulations is 120 days. Two-dimensional model output, like the vertical integrals of water vapor and cloud condensate, the surface flow and radiative fluxes, were stored hourly.

We investigated simulations with four different SST profiles, shown in Figure 4.1. Note that *qobs* was already used in simulations of Chapter 3. To understand the interplay between radiatively and SST-driven circulations we choose to study also a flatter profile referred to as *flatqobs*. These two simulations inherit an interesting geometrical composition with respect to convective aggregation. As stated previously, aggregation is expected to be forced by the SST gradient in the meridional dimension, but boundary conditions remain zonally homogeneous and thus self-aggregation may occur in the zonal dimension.

Note that we will refer to *forced aggregation* when the organization of convection is forced by the SST gradient in the meridional dimension, whereas we refer to *self-aggregation* when the organization of convection, as observed in previous RCE experiments with uniform SST, happens in the zonal dimension.

As a reference simulation in a classical radiative convective equilibrium setup, for study-

ing convective self-aggregation exclusively, we conduct an experiment with an uniform sea surface temperature of 27 °C, referred to as "27uni". Ultimately we perform an experiment with SSTs peaking with 27 °C at one pole of the sphere, referred to as "warmpole", which we introduce in appendix A.

The simulations were described regarding the temporal evolution of precipitation and domain-mean water vapor path in Section 2.4.3 (see Figure 2.5). We find that the temporal and domain-mean of precipitation are of similar magnitude for all experiments ($\sim$ 3 mm day^{-1}). Only hiSLAM-warmpole precipitates less (2.17 mm day^{-1}). For water vapor path we find that hiSLAM-27uni is moistest, with $\sim$21 mm on average. hiSLAM-qobs and hiSLAM-flatqobs are drier with $\sim$14 and $\sim$16 mm on average. Naturally the SST has a control over latent heat flux and thus over evaporation, explaining the greater moisture content of hiSLAM-27uni compared to hiSLAM-flatqobs and hiSLAM-qobs.

4.3. SST Gradient Effects in Convective Evolution and Convective Aggregation

In this part we investigate how the imposed SST profiles *qobs* and *flatqobs* affect the convective evolution and convective aggregation in our simulations.

4.3.1. Convective Evolution

We present the simulations with a focus on how the cloud and moisture fields, and the surface flow develop over time. We illustrate this in Figures 4.2, 4.3 and 4.4 by weekly snapshots of water vapor path, prw, and vertically integrated cloud condensate (cloud water plus cloud ice mass mixing ratios, q_T), along with the surface wind field.

hiSLAM-27uni

The convective evolution seen in hiSLAM-27uni (Fig. 4.2) is reminiscent to that seen in past studies of convection-permitting radiative-convective equilibrium (e.g. Bretherton et al., 2005; Hohenegger and Stevens, 2016). The evolution is summarized as the transition of a field of randomly scattered convective cells into a state of quasi-equilibrium, characterized by a a moist region hosting all convective clouds, within a larger, very dry environment. Within the dry and cloud-free area the emission of longwave radiation promotes subsidence, cooling and drying of the air, and by that convection is suppressed. In regards of convective self-aggregation this constitutes a positive radiative feedback (see e.g. Bretherton et al., 2005; Muller and Bony, 2015). Enhanced gustiness in the vicinity of the cloud cluster increases surface fluxes of heat and moisture and by that further moistens the *moist bubble*. Surface-fluxes, similar to a *WISHE*-feedback (Emanuel, 1986; Montgomery et al., 2015) in tropical cyclogenesis, constitute a positive but non-essential

feedback in convective self-aggregation (see e.g. Tompkins and Craig, 1998; Muller and Held, 2012). A deep overturning circulation establishes, similar to such illustrated in Figure 2.3: within the PBL, the flow is directed from the dry towards the moist regions (as also seen in Figure 4.2), where the air ascends in convective clouds, until it diverges below the tropopause.

The cluster, as seen here on day 57, has a circular shape and with edge-intensified deep convection. At day 85 the cluster forms a ring of deep convection and encircles a drier region. While the cluster remains aggregated for the rest of the integration period, it permanently alters in its shape, intensity and forcing of moisture convergence. The maintenance of a circular shape seems to be hindered through the large scale of the system. This finding is in line with other studies, in as far as it shows that the combination of domain size and grid spacing determines the shape and number of emerging cloud clusters (e.g. Jeevanjee and Romps, 2013; Reed and Medeiros, 2016).

hiSLAM-qobs and hiSLAM-flatqobs

Figures 4.3 and 4.4 show the temporal and spatial distribution of moisture and convection for hiSLAM-qobs and hiSLAM-flatqobs. In these simulations the SSTs peak along the equator and locally enhance surface fluxes of moisture and heat. As a consequence the low level flow converges at the Equator and near-surface moisture is advected equatorwards.

After some time though, the zonally oriented line of convection breaks up. This happens earlier in hiSLAM-flatqobs, with a breaking after around 20 days, as compared to hiSLAM-qobs. This we identify as self-aggregation, as boundary conditions are zonally homogeneous. After breaking up, the cluster rapidly contracts zonally in hiSLAM-flatqobs until it reaches an equilibrium state by around 50 days. Its zonal and meridional extents, as its intensity, vary then only slightly. The system attains a stable state, as the cloud field does not propagate and is balanced by a large-scale overturning circulation.

In hiSLAM-qobs the cluster contracts also rapidly in the zonal dimension. However, its zonal extent is greater than in hiSLAM-flatqobs and measures about the half of the length of the equator. Also the cloud field is located more closely along the equator. All of these differences can be attributed to the differently steep SST gradient.

These findings address our first research question: the meridional gradient in SSTs affects, firstly, the onset of the zonal self-aggregation: the steeper the gradient, the stronger the meridional forcing of convergence and the more persistent the convergence line. Secondly, the gradient controls the zonal and meridional extent of the cloud cluster: the steeper the gradient, the greater the zonal and the shorter the meridional extent of the cloud cluster.
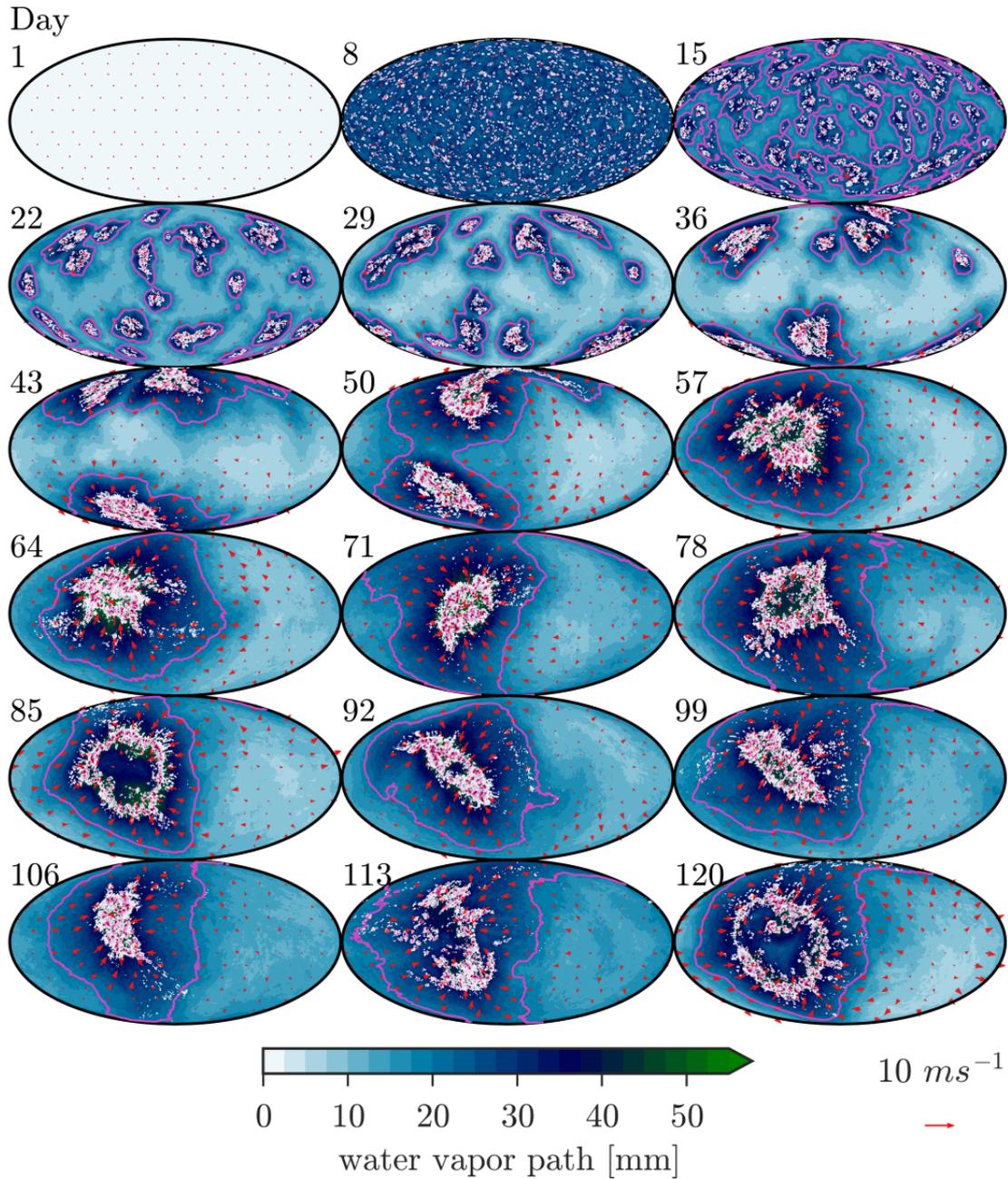
Figure 4.2.: Experiment hiSLAM-27uni: Weekly snapshots of water vapor path, in bluish shading, with a purple isoline of 20 mm, are shown. White to pink contours of vertically integrated total cloud condensate, ranging from 0.05 to 2 mm, illustrate clouds. Red arrows show the surface flow.
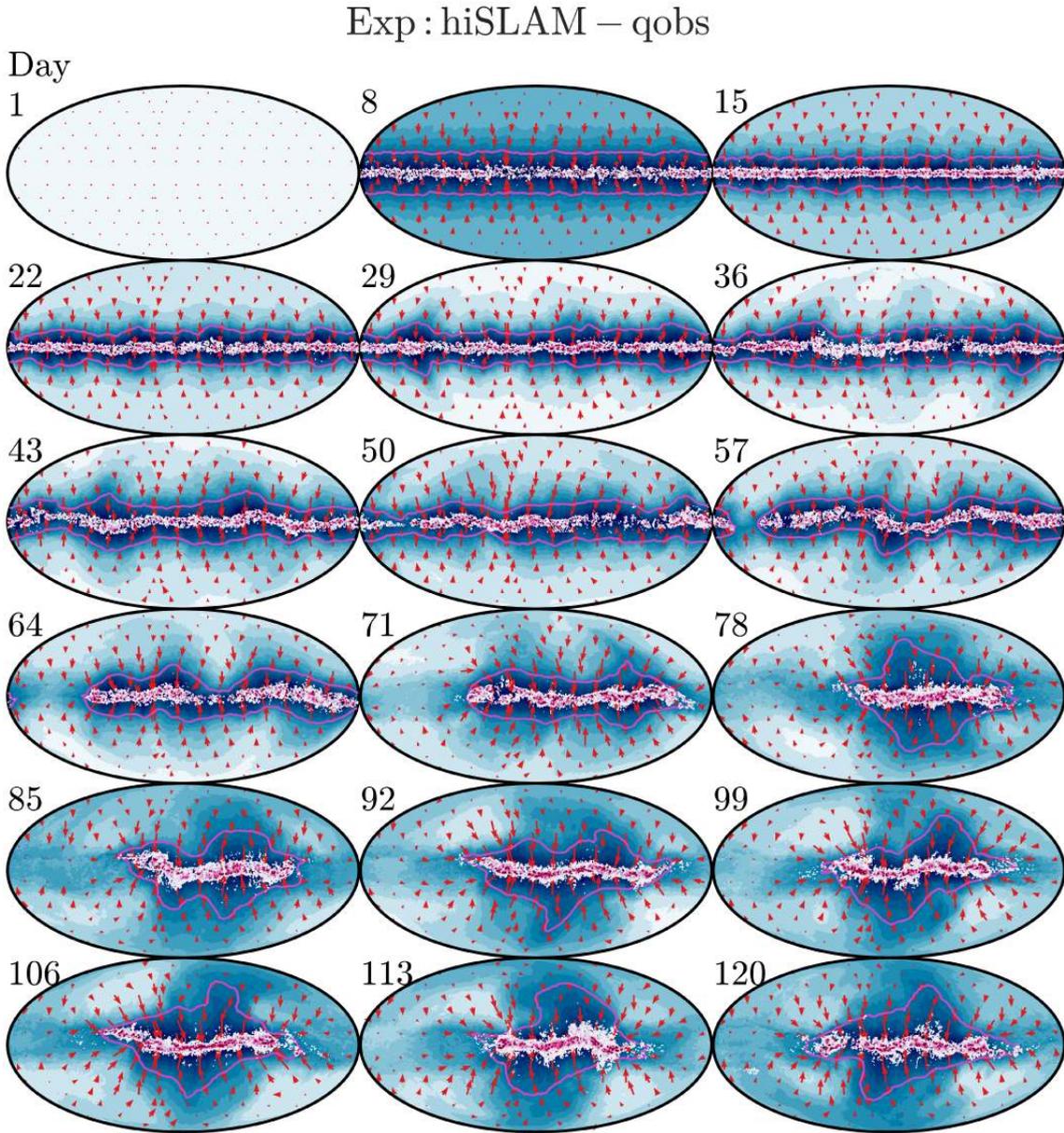
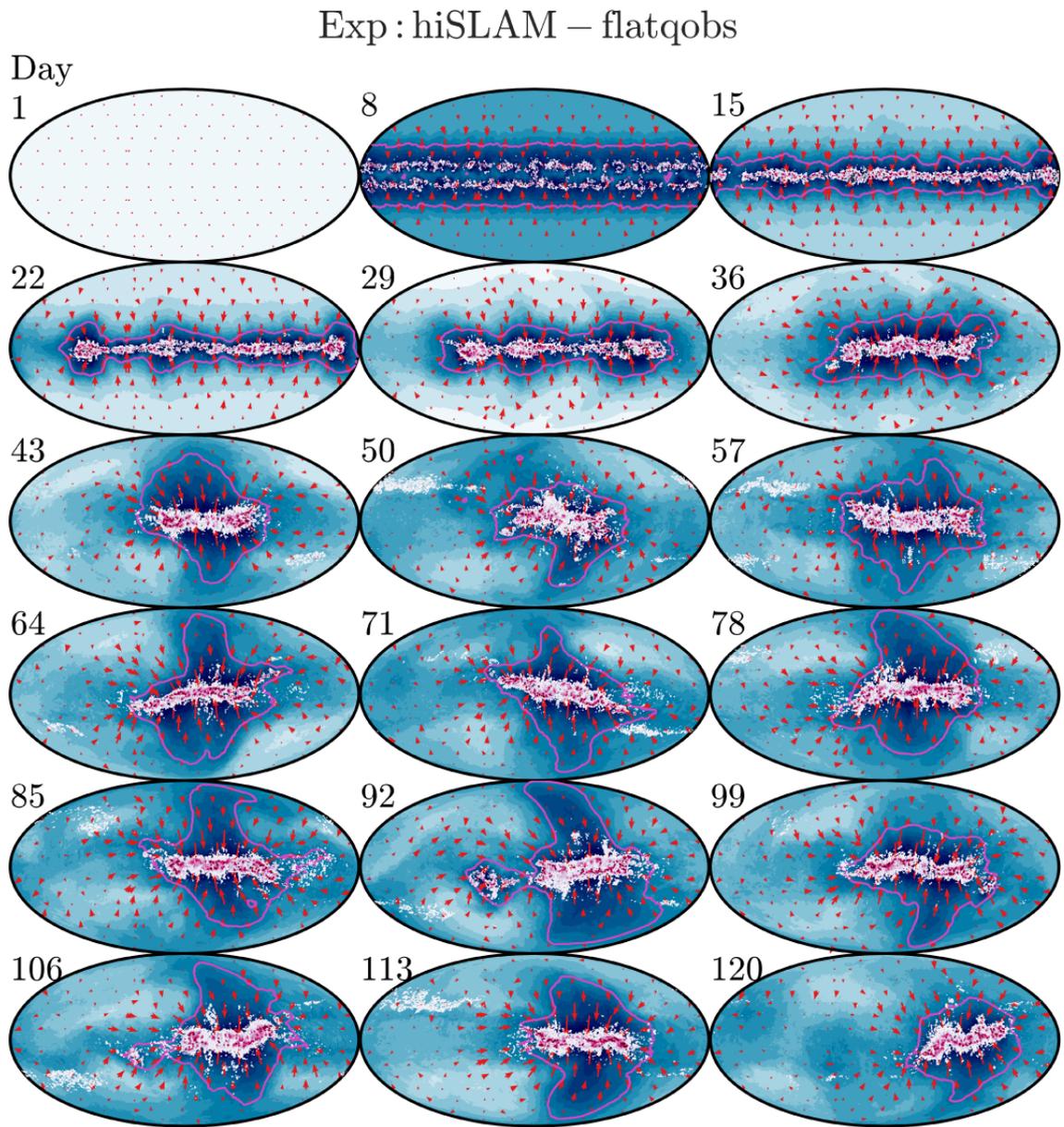**Figure 4.3.:** As Figure 4.2, but for experiment hiSLAM-qobs.

Exp : hiSLAM − flatqobs

Figure 4.4.: As Figure 4.3, but for experiment hiSLAM-flatqobs.

4.3.2. Convective Aggregation

We here discuss the temporal evolution of measures of convective aggregation, including separate measures of meridional SST driven aggregation and zonal self-aggregation. Furthermore we look into the domain-mean and spatial variance of the surface flow, and seek to find out on whether the surface flow indicates or controls convective self-aggregation.

In convection-permitting simulations of RCE, convective self-aggregation is identified as a cloud cluster located in a region of high moisture, often referred to as a "moist bubble" (e.g. Becker et al., 2018). In contrast to that, the rest of the domain, the convection-free region of large-scale subsidence, is dry. For this reason convective self-aggregation creates great spatial variance in moisture. Thus common measures of aggregation are the spatial variances of the water vapor path, of vertically integrated relative humidity and of vertically integrated moist static energy. In this study we use the inter-quartile range (IQR, 75th minus 25th percentile) of the spatial distribution of the daily mean of water vapor path. The process of convective aggregation, meaning the formation of a single cloud cluster within the model domain, can be identified as a rapid increase of moisture variance with time. Recalling that hiSLAM-flatqobs and hiSLAM-qobs allow for self-aggregation to occur only in the zonal dimension, the IQR of the meridional mean of the water vapor path ($\overline{\mathrm{prw}}^{\mathrm{merid}}$), estimates the degree of zonal self-aggregation. Likewise we expect that in the meridional dimension convective aggregation is mostly forced by the SST gradient, which is then estimated by the IQR of the zonal mean of the water vapor path ($\overline{\mathrm{prw}}^{\mathrm{zonal}}$).

Convective Aggregation in Moisture Variance

Figure 4.5 shows the temporal evolution of the IQR of the daily-mean values of prw, of $\overline{\mathrm{prw}}^{\mathrm{zonal}}$ and of $\overline{\mathrm{prw}}^{\mathrm{merid}}$.

We look at the total degree of aggregation, illustrated in panel (a) first: all experiments aggregate quickly during the first ten days. hiSLAM-flatqobs and hiSLAM-qobs reach their highest degree of aggregation already after 10 and 30 days, respectively. This is seen as a consequence of the meridional forcing through the SST gradient, forming a continuous, zonally symmetric, band of moisture and convection along the equator, that represents a high degree of aggregation. Afterwards, for hiSLAM-qobs and hiSLAM-flatqobs, total IQR steadily reduces and eventually fluctuates around a mean value of similar magnitude. Total IQR in hiSLAM-27uni increases steadily and reaches a peak after around 57 days, when a single cloud cluster has developed. The highest peak of IQR is reached after around 80 days, when the cluster forms a ring. Total IQR varies strongly as a result of the complex and ever-changing structure of the cloud cluster.

The IQR of $\overline{\mathrm{prw}}^{\mathrm{zonal}}$, shown in Figure 4.5(b), measures aggregation through the forcing of the meridional SST gradient. Both hiSLAM-flatqobs and hiSLAM-qobs aggregate immediately, as seen in an increase of the IQR of $\overline{\mathrm{prw}}^{\mathrm{zonal}}$. For hiSLAM-flatqobs it is great-
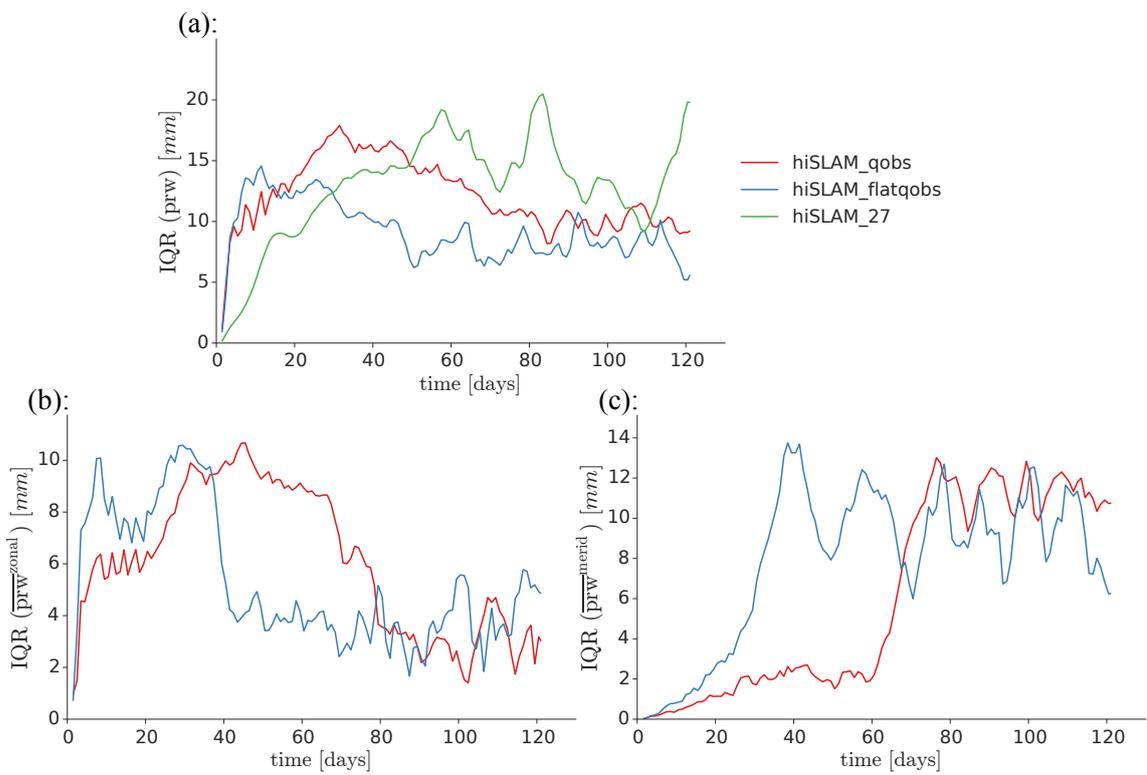
Figure 4.5.: From (a) to (c): Inter-quartile ranges of the total, and of the zonal and meridional mean of water vapor path, prw $[mm]$.

est after ∼30 days, when the convergence line along the equator has formed, but zonal self-aggregation has not taken place yet. Subsequently, when the cloud cluster contracts zonally (see Figures 4.3 and 4.4), the IQR of $\overline{\mathrm{prw}}^{\mathrm{zonal}}$ decreases rapidly. The meridional aggregation evolves equivalently for hiSLAM-qobs. A peak in SST-forced aggregation is reached after ∼45 days, followed by a period with a stable degree of aggregation. When the convergence line breaks up after ∼60 days the IQR decreases also rapidly.

The IQR of $\overline{\mathrm{prw}}^{\mathrm{merid}}$, shown in Figure 4.5(c), is a measure of convective self-aggregation in the zonal dimension. For hiSLAM-flatqobs it increases quickly from the beginning, but in particular during day 20 to 40. This indicates that the zonal self-aggregation, that can be seen as the zonal contraction of the cloud cluster in Figure 4.4, takes place rapidly after the early break-up of the convergence line. Right at the peak of the IQR of $\overline{\mathrm{prw}}^{\mathrm{merid}}$, we see that the meridional aggregation, forced by SSTs, decreases (see Figure 4.5(b)). In hiSLAM-qobs only after around 57 days the convergence line breaks up and zonal self-aggregation takes place. The degree of zonal self-aggregation varies, in particular for hiSLAM-flatqobs, strongly with periods of around ten days until the end of the simulation.

We here found a first relevant result in concerns of the effect of the SST gradient on convective evolution (research question #1): for a steeper SST gradient, the time it takes to break up the convergence line is longer as convergence and convection are forced more strongly along the equator, and by that the development of a zonal circulation, that initiates zonal self-aggregation, is suppressed.

In regards of the interplay of both forced aggregation in the meridional dimension and self-aggregation in the zonal dimension, we note that with the onset of zonal self-aggregation the meridional forced aggregation is weakened. We will look into this result in detail in section 4.4.

Convective Aggregation in the Surface Flow

For describing the circulation associated with convection and its aggregation, we assume that the surface flow is a sufficient representation of the inflow, and thus of the low-level branch of the overturning circulation. We also aim to find out whether the breaking-up of the initial convergence line in hiSLAM-qobs and -flatqobs, and the subsequent onset of zonal self-aggregation, can be identified in the surface flow. In Figure 4.6 we show the time series of daily mean and domain-mean of surface wind speed and its daily mean spatial variance, and for hiSLAM-qobs and hiSLAM-flatqobs also of the absolute values of meridional and zonal velocity.

For the surface wind speed, shown in Figure 4.6(a), we find for hiSLAM-27uni that the mean and the variance are coupled and increase slowly with time, peaking after ∼ 55 days for the first time. This peak coincides with a peak in the IQR of prw, and likewise peaks around day 80 and 120 are present in both, the IQR of prw and in the mean and variance of the surface wind speed. Thus we find that convective self-aggregation is measured in

both the mean and variance of the surface wind speed.

For hiSLAM-flatqobs and hiSLAM-qobs the surface wind speed reaches its time-mean magnitude immediately after initialization, as a result of the SST gradient forcing the meridional flow (see Figure 4.6(b)). The magnitude of the mean surface wind speed, as well as the meridional velocity, is greater for hiSLAM-qobs than for hiSLAM-flatqobs, reflecting the steeper SST gradient in hiSLAM-qobs as compared to hiSLAM-flatqobs. We find that the variance of meridional velocity is here a measure of both, meridional SST-forced aggregation, and convective self-aggregation, as it increases with the onset of convective self-aggregation.

For both hiSLAM-flatqobs and hiSLAM-qobs the evolution of the mean and variance of the zonal velocity are very similar to the evolution of IQR of $\overline{\mathrm{prw}}^{\mathrm{merid}}$ (see Figure 4.5(c)). Thus we see that, analogously to hiSLAM-27uni, the zonal convective self-aggregation is reflected in both the mean and the variance of the zonal velocity. We also find that the increase of the mean zonal velocity is concurrent with a reduction of the mean meridional velocity, reflecting the weakening of meridional forced aggregation when the cloud clusters self-aggregate zonally. Eventually the mean of meridional and zonal velocity are balanced such that the mean surface wind speed, different than in hiSLAM-27uni, remains approximately constant.

We find that surface wind speed variance is a metric of convective aggregation. This is plausible as aggregation forms large-scale regions of subsidence, where the surface flow is expected to be calm, as well as a large convective cluster, that is expected to organize and intensify its low-level inflow.

The identification of aggregation in the mean of surface wind speed is explained by the general intensification of the convective system through self-aggregation, like e.g. in terms of the amount of precipitation produced. In Figure 2.5(c) we observe that for hiSLAM-27 the peaks of precipitation occur at days $\sim$55 and $\sim$80, which match the peaks of the presented measures of its self-aggregation. The surface wind speed, in its representation of the converging low-level branch of the overturning circulation and thus of the entire circulation, is also a metric for the intensity of the system. For these reasons we find the mean surface wind speed is a measure of convective aggregation, as well as that self-aggregation intensifies the circulation and precipitation rate of a convective system.

For addressing the question on whether we find the onset of zonal self-aggregation reflected in the mean zonal circulation, we recall that we have just identified the zonal self-aggregation of hiSLAM-qobs and hiSLAM-flatqobs being measured in both the mean and the variance of the zonal velocity. This solidifies the assumption that the circulation is in fact measured by the surface wind speed, here in zonal velocity. We find that the aggregation takes place at very different times, but also that its temporal evolution is similarly rapid (as seen in the steepness of the increase of the mean zonal velocity). We also find that the process for both experiments starts when a mean zonal velocity of $\sim$0.5
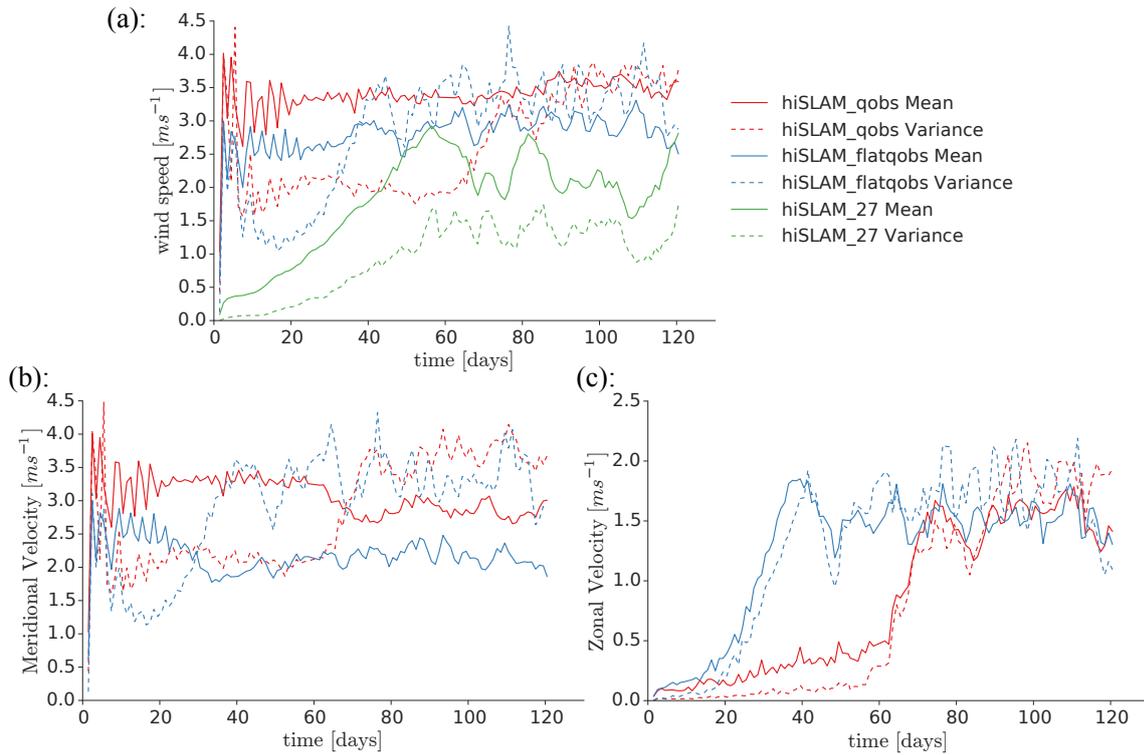
Figure 4.6.: Time series of the domain-mean (solid lines) and domain-variance (dashed lines) of the daily mean surface flow: Panel (a) wind speed, panel (b) absolute value of meridional velocity and panel (c) absolute value of zonal velocity.

m s^{-1} is reached. This suggests that for both experiments roughly the same intensity of circulation is needed to trigger zonal self-aggregation. We find that with the intensification of the zonal circulation the meridional circulation weakens only slightly. As stated before (Section 4.3.2), a strong meridional SST gradient stabilizes the convergence line and the development of a zonal circulation is hindered. Still, as soon as a strong enough zonal circulation has established, zonal self-aggregation is hardly affected by the SST gradient.

4.4. SST Gradient Effects on the Environment

It is perceived as a deficit of convection-permitting RCE simulations with uniform SSTs, that for the state of aggregation the domain-mean moisture content as well as the moisture content of the dry patch, are unrealistically low (e.g. Bretherton et al., 2005). So far only in RCE simulations on an elongated domain with multiple convective clusters (Wing and Cronin, 2016) the deficit in the domain-mean moisture content is overcome. We find that our simulations, using the SST-profiles "qobs" and "flatqobs" develop a circulation that exports moisture from the convective cluster into the dry areas at the poles, and by that increases both, the domain-mean as well as the moisture content of the clear-sky, convection-free area. In the temporal evolution of domain-mean prw, shown in Figure
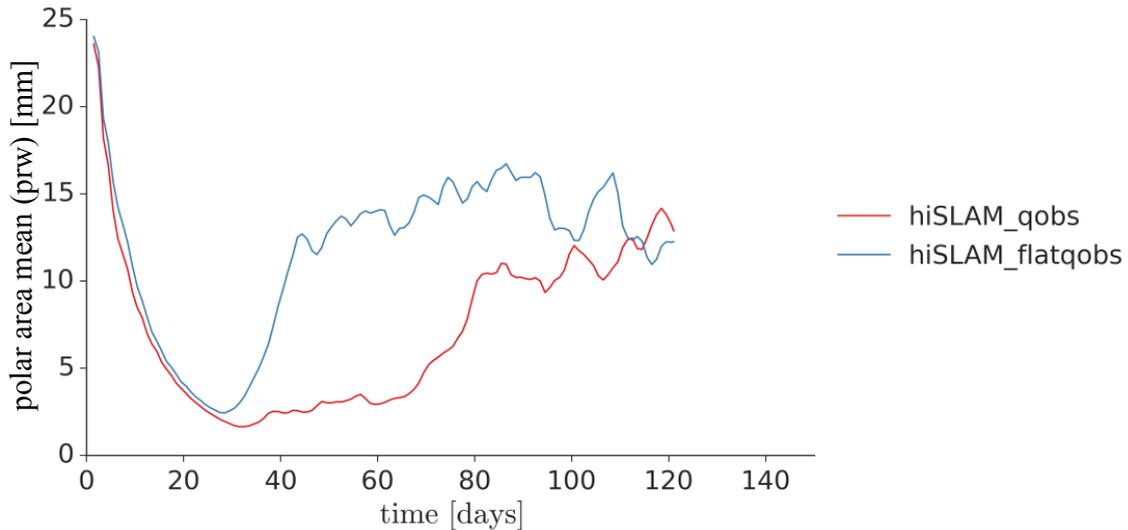
Figure 4.7.: Temporal evolution of water vapor path, prw, averaged over the polar regions, north of 60° and south of -60° latitude.

2.5 of Section 2.4.3, this signal is not clearly evident. This is because we find that the moistening of the polar regions comes at the cost of a drying of the originally moist equatorial region. In the following we investigate this feature in detail and in section 4.5.2 discuss its relation to an intriguing phenomenon of tropical dynamics, atmospheric rivers.

4.4.1. Meridional Moisture Export

The convective evolution of hiSLAM-qobs and hiSLAM-flatqobs, illustrated in Figures 4.3 and 4.4, suggests that a significant amount of moisture can be found at higher latitudes, after the zonal self-aggregation has taken place. The choice for the prw-isoline of 20 mm marks a criterion for the identification of atmospheric rivers, introduced by Ralph et al. (2004) and also used by Waliser et al. (2012), and suggests the presence of atmospheric-river-like flows in the later stages of the simulations. A quantification of the increase in moisture for the regions north of +60° and south of -60° latitude (polar regions) is given in Figure 4.7, showing the temporal evolution of the area-mean of the water vapor path, prw. We first find the drastic drying of the polar region, down to values of less than 2.5 mm, for both simulations, which comes along with the meridional aggregation forced by SSTs, that advects moisture equator-wards. Then we find that moisture increases when zonal self-aggregation takes place, which is earlier for hiSLAM-flatqobs than for hiSLAM-qobs, in agreement with the earlier zonal self-aggregation in hiSLAM-flatqobs. The origin of this polar moisture anomaly is non-trivial as the low-level flow converges at the convective systems and transports moisture equator-wards at all times.

We introduce the matter in greater detail at hands of hiSLAM-flatqobs in an comparison of an early, dry day (28) with a later, moist day (94). Figure 4.8 shows total atmospheric

water content q_{vT} ($q_{vT} = q_v + q_T$, where q_v is specific humidity and q_T total cloud condensate mixing ratio) in panel (a) at 0.4 km and 3.4 km altitude and in panel (b) as a vertical-meridional cross section along the meridian highlighted in panel (a). At 0.4 km the principle circulation pattern is unchanged from day 28 to day 94, showing convergence at the cloud cluster, which is located at the equator. However, the flow has intensified and the low levels are generally moister at day 94. At 3.4 km we find predominantly poleward-directed outflow, that exports moisture away from the convective cloud system. This circulation also appears much stronger on day 94 than on day 28. In particular a relatively narrow stream appears north of the cloud cluster on day 94, reaching the pole and crossing it back equator-wards, apparently recycling its moisture into the cluster. In the meridional-vertical cross section, panel (b) of Figure 4.8, we see that the convective clouds expand meridionally, and the associated outflow layers are also vertically deeper, reach further polewards and have greater velocities than at earlier times. Eventually the intensified meridional circulation is seen to transport more moisture in the later stage.

4.4.2. Polar Moisture Budget

In order to clarify the controls of the moisture content of the polar regions we compute its budget, following Bretherton et al. (2005). In general the amount of atmospheric water in a column is controlled by evaporation from the surface, precipitation and column-integrated divergence of atmospheric water, representing advection. For our analysis evaporation is computed as the latent heat flux, F_{lat}, divided by the enthalpy of vaporization, L_{eva} and precipitation is given by the precipitation flux (P_{re}). Thus column-integrated moisture divergence can be computed as a residual. However we see from Figure 4.8, that advection is expected to be driving the budget in the polar regions, with a particular vertical structure. Thus we seek to separate boundary layer advection from free-tropospheric advection. The moisture balance we investigate thus takes the form of:

$$\frac{\partial \langle q_{vT} \rangle_z}{\partial t} = \langle \frac{F_{lat}}{L_{eva}} \rangle - \langle F_p \rangle + \frac{1}{A_{pol}} \int_0^{TOA} \int_0^{2\pi} \rho\, v\, q_{vT}\ d\phi dz \tag{4.1}$$

$$\frac{\partial \langle q_{vT} \rangle_z}{\partial t} = E_{va} - P_{re} + \frac{1}{A_{pol}} \int_0^{1.3km} \int_0^{2\pi} \rho\, v\, q_{vT}\ d\phi dz + \frac{1}{A_{pol}} \int_{1.3km}^{TOA} \int_0^{2\pi} \rho\, v\, q_{vT}\ d\phi dz \tag{4.2}$$

$$\frac{\partial \langle q_{vT} \rangle_z}{\partial t} = E_{va} - P_{re} + A_{withinBL} + A_{aboveBL} \tag{4.3}$$
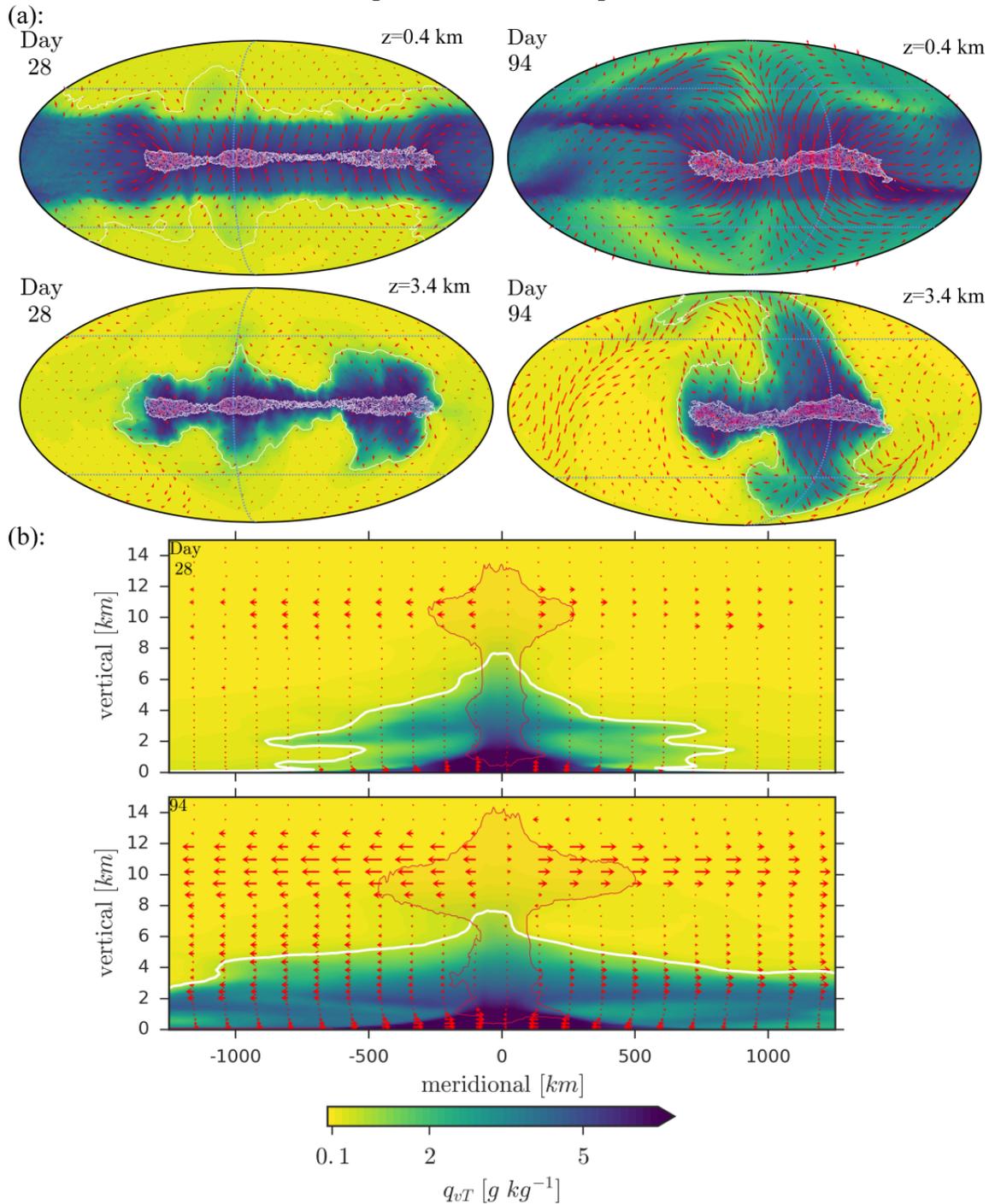
Figure 4.8.: Daily mean of the total atmospheric water content, q_{vT}, for days 28 and 94: in panel (a) for a horizontal cross section at 3.4 km and 0.4 km altitude, with wind vectors and contours of cloud condensate and in panel (b) for a vertical-meridional cross section, with an isoline of cloud condensate and wind vectors, along the meridians highlighted in panel (a). The white contour highlights the isoline of $q_{vT} = 0.1$ g/kg.

where the (northern) polar area mean, $\langle \cdot \rangle \equiv \frac{1}{A_{pol}} \int_0^{2\pi} \int_{\frac{1}{3}\pi}^{\frac{1}{2}\pi} (\cdot) \sin\theta \, d\theta d\phi$, with A_{pol} being the area of the polar region, and θ and ϕ being latitude and longitude, respectively. With the subscript z added, the polar area mean contains an integration over the vertical also: $\langle \cdot \rangle_z \equiv \int_0^{TOA} \langle \cdot \rangle \, dz$. Note that advection term is computed as the vertical integral of the moisture flux $\rho v q_{vT}$ through the parallel at 60° latitude, relative to the polar surface area. The advection term is then separated into contribution from within $A_{withinBL}$ and from above the boundary layer $A_{aboveBL}$, with the height of the boundary layer being identified at 1.3 km. We chose this altitude, as it marks the reversal of the meridional wind direction, as can be seen from Figure 4.8(b).

Figure 4.9 shows the temporal evolution of the respective terms, along with the polar area-mean of the vertically integrated total atmospheric water. From panel (a) we note the following: (1) the advection term, as computed from the 3D output, is almost equal to the advection, computed as the residual. (2) Advection controls the moisture budget in the polar regions, as it is greater than evaporation and precipitation. (3) Evaporation and precipitation both episodically and concurrently make a contribution. From panel (b), showing the separation of the advection term into contributions from within and from above the BL, we find: (4) Advection within the boundary layer exports moisture, while advection above the boundary layer imports moisture to the polar regions. (5) Advection within and above the BL are of similar magnitude and appear coupled, suggesting that they are part of the same circulation.

From this analysis we conclude that advection of moisture above the boundary layer controls the polar moisture budget and thus is responsible for the moistening of the polar regions.

In the temporal average (days 80-120) of the moisture flux through the parallel at 60°N, shown in Figure 4.10(a), it can be seen that all of the components of the circulation are quite distinct and persistent. The low level flow, advecting moisture equator-wards, is zonally located within 0 and 1500 km and spans the boundary layer, up to an altitude of around 1.3 km. Above that there is the flow that is moistening the polar region. It is narrower but thicker than the boundary layer flow and spans altitudes up to 4 km. However, it does not only import moisture into the polar region: the component of the flow at zonal = 1750 km, right above the boundary layer, must be interpreted as its continuation. As the flow crosses the pole its moisture is transported back equator-wards, and eventually, as located in a region of subsidence, the moisture is recycled into the boundary layer and eventually into the convective system. We anticipate this to be a stream like an atmospheric river, that transports moisture from the equatorial moisture pool to a remote extra-tropical system. We find that the structure of the circulation, as shown in Figure 4.10(b), is present from an early stage on, but intensifies when zonal self-aggregation takes place.
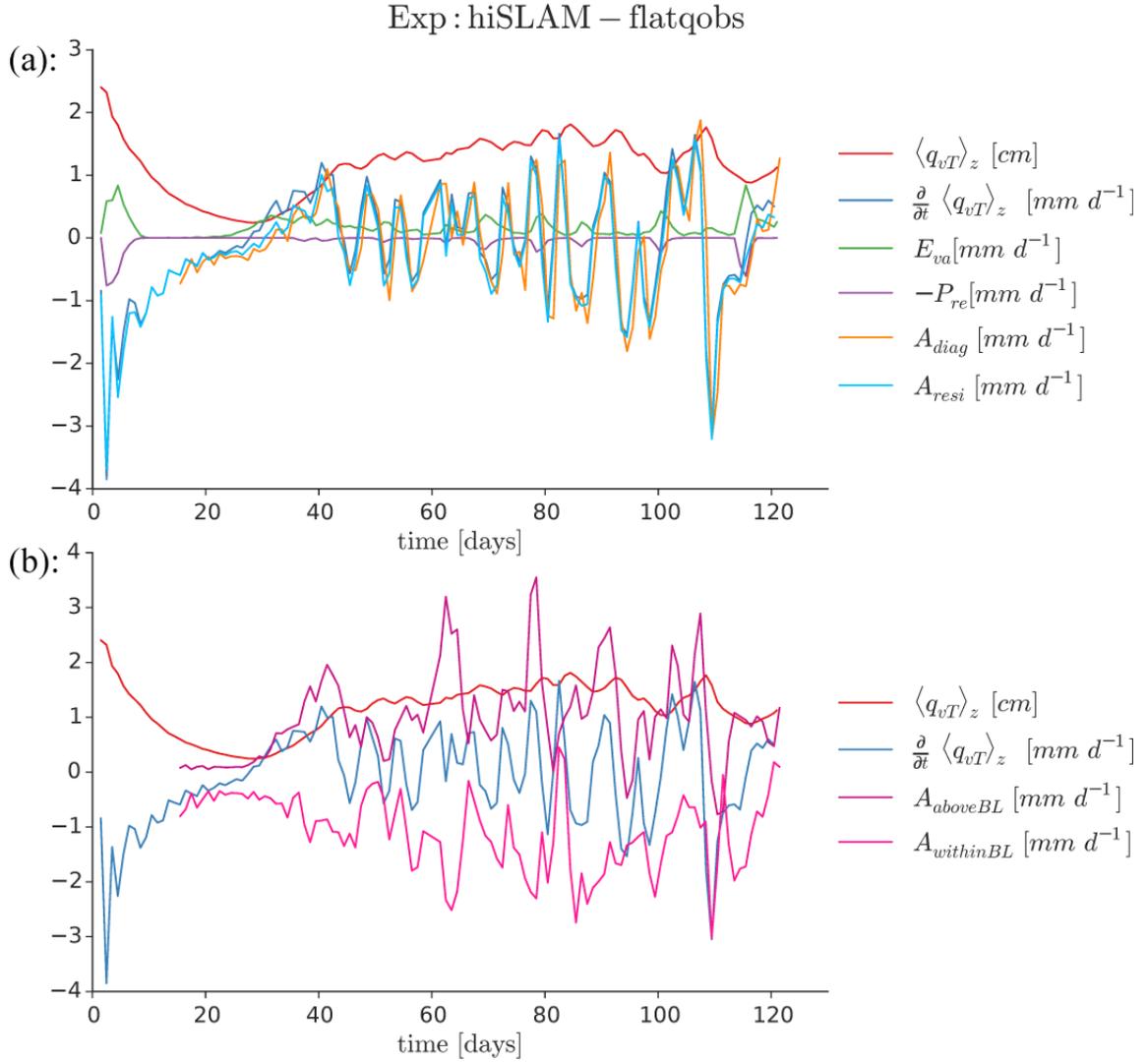
Figure 4.9.: Time series of the moisture budget for the polar regions, north of 60°. Panel (a) shows, along with the vertically integrated total atmospheric water and its time-tendency, the individual terms of the moisture budget, associated with precipitation, P_{re}, evaporation, E_{va}, and advection as computed from the 3D output, A_{diag}, and as computed as the residual, A_resi. Panel (b) shows the separation of the advection term into contributions from the flux within $A_{withinBL}$ and from above the boundary layer, defined at $z = 1.3$ km, $A_{aboveBL}$.
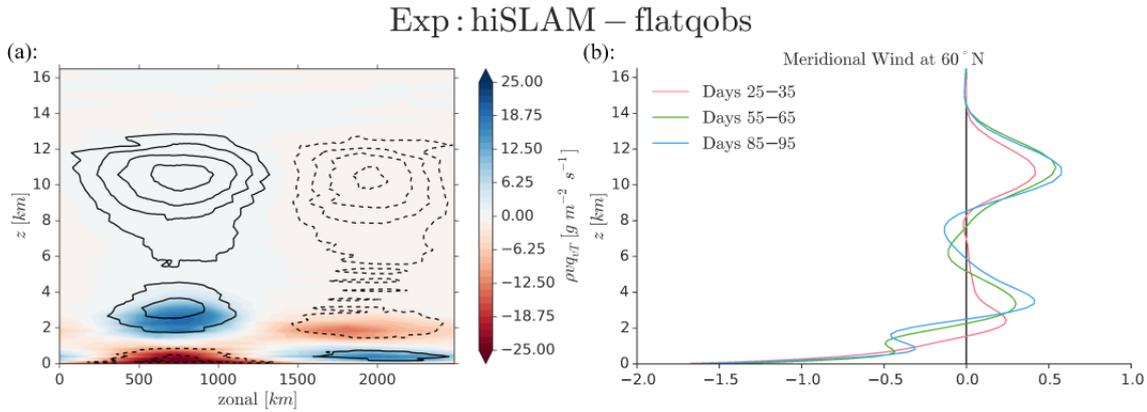
Figure 4.10.: Panel (a) shows the temporal average (days 80-120) of the total atmospheric moisture flux vq_{vT} through the parallel at 60°N, with positive values (blue shading) indicating moisture import into the polar region and negative values (red shading) moisture export equatorwards. Black contours are isolines of the meridional velocity v at intervals of $1ms^{-1}$; the $0ms^{-1}$ isoline is omitted. Panel (b) shows the vertical profiles of temporal averages of v for three periods averaged over the parallel at 60°N.

4.4.3. The Mean Circulation of hiSLAM-flatqobs

He were aim to reveal the characteristic properties of the circulation of hiSLAM-flatqobs: For this we show in Figure 4.11 the temporal average (days 80-120) of the flow and cloud condensate at different levels. In the surface level's temperature field the zonal inflow to the east and to the west of the cloud cluster is anomalously warm, as increasing wind speeds in the vicinity of the cluster enhance surface fluxes of heat. The cloud cluster's cold pool can be identified as cooler temperature within the cloud cluster and calm regions close to the poles are seen to be covered in fog. In both, the surface level flow and the flow at 1.3 km, the convergence of air mass at the cloud cluster can be seen, whereas at 1.3 km altitude the inflow is dominated by the zonal component. At 2.0 and 2.4 km altitude the meridional outflow becomes evident. At these levels we identify that the meridional outflow crosses the poles, reaches the equator and flows zonally back into the cloud cluster. The field of cloud condensate at 2.0 km shows that the meridional outflow appears to not be associated with shallow clouds. As seen before in Figure 4.8, the meridional outflow above the boundary layer, here at 2.4 at 3.4 km, is found to transport moisture from the cloud cluster exclusively polewards. The vertical velocity field at 5.8 km marks the deep convective updrafts within the cloud cluster and shows that for the rest of the domain the air mass is generally subsiding. We next aim to investigate the flow and moisture flux through the meridians and parallels marked at 5.8 km..

Figure 4.12 shows the moisture flux through the parallels at 30° latitude north and south of the cloud cluster, as well as through the meridians to east and to the west of the cloud cluster, averaged respectively. The meridional inflow is about twice as broad as the

zonal inflow, as both scale with the dimensions of the cloud cluster. We note that the zonal inflow takes place over warm SSTs, while the meridional inflow happens over colder SSTs. This difference is seen to have little effect on the temperature profile, as seen from the mean profiles in panels (b) and (d) of Figure 4.12, but is found to affect the depth of the boundary layer, if that is defined as the vertical extent of the inflow. Further, as could be anticipated from Figure 4.11, the outflow and moisture export happens exclusively in the meridional dimension. The poleward stream, measured by the 2 ms^{-1} isoline spans vertically from around 2 up to 5 km, and horizontally across around 1200 km, and by that is narrower than the low level inflow. Recalling Coppin and Bony (2015) we confirm that a shallow circulation is favored above cool SSTs. We also find that the shallow circulation does here not enhance aggregation, but weakens it by exporting moisture from the cloud cluster towards the dry areas. Cloud-radiative effects however appear not relevant for driving the shallow circulation, as we do not find shallow clouds reaching far polewards, neither in Figure 4.8 nor in Figure 4.11.

In conclusion we find that the shallow circulation presented here is persistent and well-organized. In summary the characteristic of the shallow circulation of hiSLAM-flatqobs are:

(1) zonal and meridional convergence at low-levels (z ≤ 1.3 km),

(2) exclusively meridional, moist outflow at mid-levels (z ≥ 1.3 km),

and (3) a moisture recycling flow across the poles back into the zonal low-level inflow.

4.5. Discussion

Here we discuss the shallow circulation, how it affects convective aggregation in our simulations, and how it relates to atmospheric rivers.

4.5.1. On the Role of the Shallow Circulation in Convective Aggregation

The shallow circulation is here found to be favored, on the one hand, at the elongated sides of the cloud cluster and, on the other hand, above low SSTs (consistent with (Coppin and Bony, 2015)). However, we do not find evidence for the shallow circulation being driven by cloud-radiative cooling of shallow clouds. In concerns of the drivers of the shallow circulation, particularly the observed outflow layer, also the role of water vapor needs to be addressed. The water vapor that characterizes the flow may be having, e.g. through its interaction with shortwave radiation, an effect on its propagation.

Ultimately, here the shallow circulation acts to weaken convective aggregation by its upper branch transporting substantial amounts of moisture away from the cloud cluster to dry non-convecting regions. This we saw in the measure of meridional forced aggregation (Figure 4.5(b)): it weakened through the intensification of the shallow meridional circulation. Moreover the moisture budget clearly shows that substantial amounts of moisture
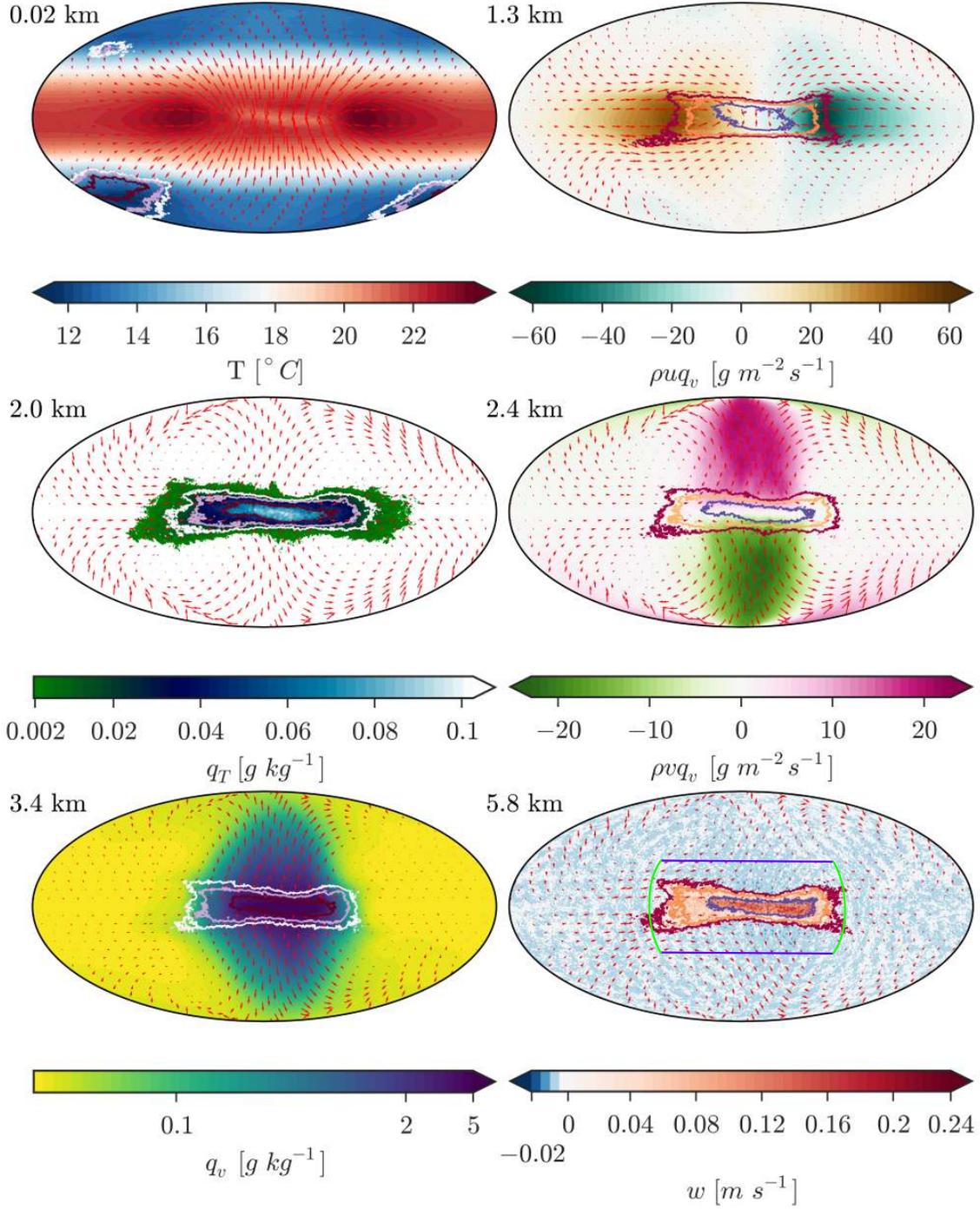
Figure 4.11.: Temporal average (days 80-120) of the flow and cloud condensate q_T (contours at the 95th,97th and 99th percentile), at 0.02 km altitude with the temperature field $T[K]$, at 1.6 km with zonal moisture flux $\rho u q_v[m s^{-1}]$, at 2.0 km with the field of cloud condensate $q_T[g/kg]$, at 2.4 km with meridional moisture flux $\rho v q_v[m s^{-1}]$, at 3.4 km with the specific humidity field $q_v[g/kg]$ and at 5.8 km with the field of vertical velocity $w[m s^{-1}]$.
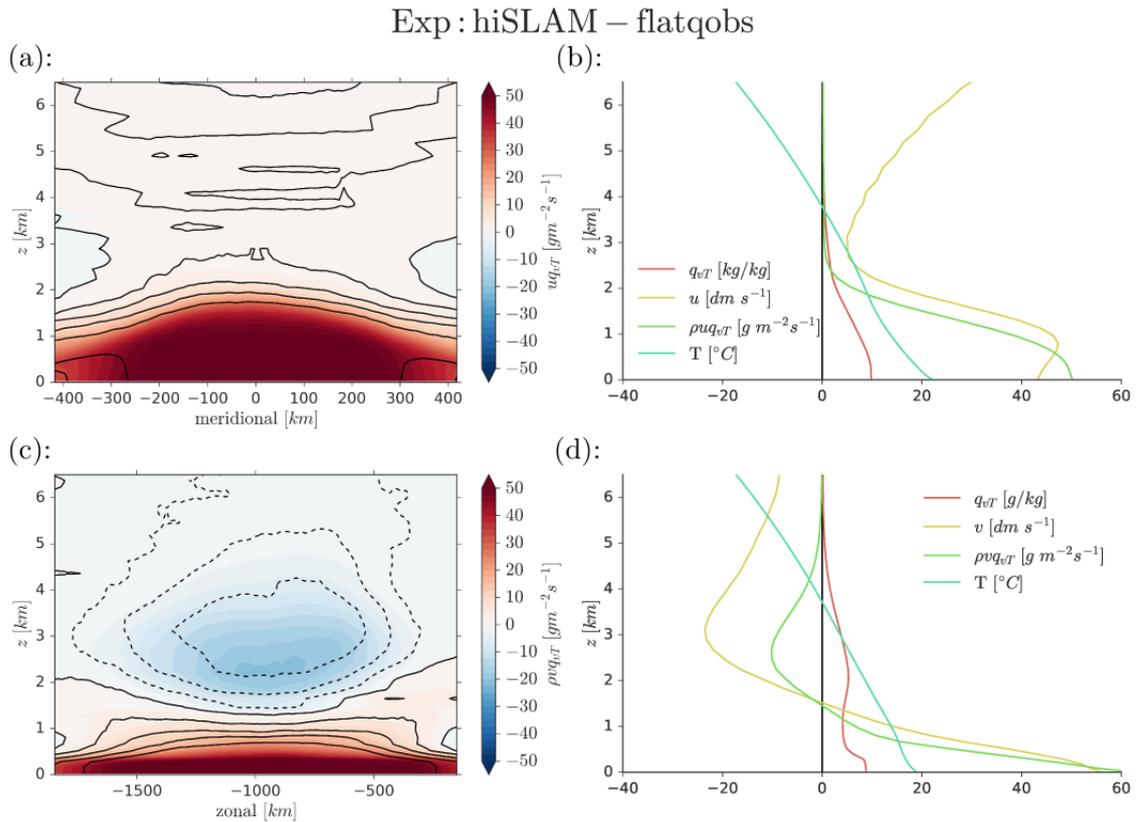
Figure 4.12.: Temporal average (days 80-120) of (a) the moisture flux, uq_{vT}, as an average of the meridians east and west of the cloud cluster, as marked in Figure 4.11 at 5.8 km, within 30°N and 30°S. Also shown are contours of the zonal velocity, accounted as relative to the cluster. Panel (b) shows mean vertical profiles of the zonal moisture flux, its components and of temperature. Panels (c) and (d) are equivalent to panels (a) and (b), but for the meridional dimension, averaged over the shortened parallels 30°N and 30°S, as marked in Figure 4.11 at 5.8 km.

are exported by the shallow circulation (see Figures 4.9 and 4.10).

4.5.2. The Shallow Circulation as an Atmospheric River

Several aspects of the moisture-rich meridional flow, as seen in experiment hiSLAM-flatqobs, suggest that it can be interpreted as an atmospheric river (introduced in Section 1.2.3).

First, the dimensions: in our simulations the flow extents from the equator, across the pole, back to the equatorial region and by that measures more than 2000 km in its length. We estimate the mean width of the flow to be around 500 to 1000 km. This means that a characteristic property of atmospheric rivers, that is their small width and large length (Guan and Waliser, 2015), is fulfilled.

Second, the flow's location just above the boundary layer, within altitudes of 1 to 5 km, resembles their characteristics as low-level jets (Ralph et al., 2010).

Third, ARs are often associated with mid-latitude storm systems, contributing large amounts of moisture to enhance precipitation (Lavers et al., 2012; Eiras-Barca et al., 2018). In analogy to that we find in our simulations that hiSLAM-flatqobs' cloud cluster is coupled to itself, as moisture, originally exported from the cluster, is eventually recycled back into the cluster.

Ralph et al. (2010) showed the multi-scale complexity of the environment that atmospheric rivers appear in, involving frontal systems and synoptic scale wave patterns. In contrast to that we find the occurrence of the moisture-rich flow of our simulations to occur in a basically unperturbed environment. In that sense the environment is characterized by low moisture content and large-scale subsidence and thus resembles typical subtropical conditions. Still the authors also find the coupling of atmospheric rivers to Kelvin waves, to which we find an analogy in our simulations. The flow pattern of Kelvin waves is characterized by pure zonal convergence (see Figure 3(f) Kiladis et al. (2009)) and by that resembles the zonal self-aggregation found in hiSLAM-flatqobs and hiSLAM-qobs. We identify the zonal self-aggregation and its associated zonal convergence to precede the development of the meridional moisture-rich circulation. In this we find another analogy to atmospheric rivers.

4.6. Conclusions

In studying this set of convection-permitting idealized simulations, we revealed the effects of a SST gradient on the convective evolution and convective aggregation, as well as on the environment of the emerging cloud cluster. By that we study convective aggregation in novel, not purely homogeneous boundary conditions.

The SST gradient was seen to immediately force a convergence line and convection along the equator. The steeper the SST gradient the longer it took to break up this structure and

to develop a strong enough zonal circulation for zonal self-aggregation to set in. Neither the required strength of the circulation nor the rapidity of zonal self-aggregation were seen affected by differences in the steepness of the SST gradient. However, the zonal and meridional extents of the cloud cluster were found to be controlled by the SST gradient.

The effect on the environment of the cloud cluster in hiSLAM-flatqobs was seen to be controlled by advective processes associated with its shallow circulation. We showed how it exports moisture from the cloud cluster polewards. By that originally dry regions were moistened and a deficit of traditional RCE studies of convective self-aggregation, too dry non-convecting regions, overcome. We found that this circulation was occurring on the elongated side of the cloud cluster and above cool SSTs.

The analogies we draw to atmospheric rivers show the potential added value of developing idealized modeling frameworks towards more complex conditions: relating phenomena found in a complex idealization to those of the real atmosphere is possible.

SUMMARY AND CONCLUSIONS

I here summarize the results of the main chapters 3 and 4, answer the research questions stated in the Introduction (Section 1) and then integrate my study in a broader scientific context.

In Chapter 3 of this dissertation I studied *Convectively Generated Gravity Waves in high-resolution models of tropical dynamics*. I began with introducing general properties of the circulation and tropical convection, as realized in the simulations. While the mean circulation was seen unaffected by numerical resolution and the representation of convection (SLAMs), the full complexity models (NARVAL2 and ICSOM1) showed zonal circulations, like the trade winds and in the stratosphere winds of the QBO, and an asymmetrical meridional circulation (see Figure 3.2). For SLAMs the differences in their model setup revealed in the cloud field, where we saw that zonal self-aggregation occurred in SLAMs with an explicit representation of convection (hiSLAM and coSLAM-xc), but was inhibited by a parameterization of convection (see Figure 3.3). Then I presented statistical properties of the clouds' vertical velocity, temperature anomalies and heating rates, that are expected to matter for the generation of gravity waves (Figures 3.6,3.7 and 3.8). It became evident that higher resolution manifests in a greater mean and greater variance of updraft velocities. The vertical velocities in clouds, when using a parameterization of con-

vection, are weak and fail to realize a dynamical overshooting at cloud tops. This feature we find realized in all other simulations representing convection explicitly, particularly in hiSLAM, along with oscillations around the level of neutral buoyancy. This process is expected to relate to the mechanical generation of gravity waves. Further characterization of the gravity wave generation was given through the statistics of the latent heating and its vertical scale, as well as through the spectral analysis of precipitation and upper tropospheric vertical velocity (Figure 3.9).

In the following Section 3.3 we analyzed zonal wavenumber and frequency spectra of gravity wave properties (zonal momentum flux, zonal and vertical velocity variance) in the stratosphere (Figure 3.10), and in these we find spectral properties of precipitation and vertical velocity in the troposphere reflected. This constitutes the main part of the study: in spectral space we compare the simulations among each other to gain insight into the effect of specific model properties. The spectral slope of gravity wave momentum flux in the lower stratosphere is relatively flat ($\sim k^{-1}$, e.g. NARVAL2) and may be even flatter locally above intense convection (hiSLAM). In vertical wavenumber spectra we identified the modes and dominant vertical wavenumber, and find the universal properties of gravity waves reproduced as well as the vertical scales for which the gravity waves are saturated (see Figures 3.11 and 3.12).

In Chapter 4 I studied *Convective Aggregation in idealized simulations with SST gradients*. In Section 4.2 I introduced the numerical simulations and motivated their different SST profiles (Figure 4.1). Then, in Section 4.3, I presented and discussed the temporal evolution of the convective cloud field (see Figures 4.2, 4.3 and 4.4), as well as the development of convective aggregation. It became clear how convective aggregation differs, when occurring in an environment characterized by a SST gradient, from pure self-aggregation in homogeneous boundary conditions. The SST gradient immediately forces aggregation in form of a convergence line along the equator, where SSTs peak. The convergence line is seen to break up sooner or later, for a flatter or steeper gradient in SST. Then zonal self-aggregation sets in and the cloud cluster contracts rapidly. The measure of convective aggregation we used, the Inter-quartile range of the water vapor path and its zonal and meridional mean (Figure 4.5), confirmed what we had seen in the convective evolution. However, it was also revealed that the zonal self-aggregation seen in simulations with a SST gradient, came along with a weakening of meridional forced aggregation. Further, we showed that the spatial variance and domain-mean of the surface wind speed (Figure 4.6) are both measures of convective aggregation. Spatial variance works, because dry and moist regions are distinctly calm and intense in their surface flow, respectively. The domain-mean of the surface flow is a measure of the general intensity of the overturning circulation and the degree of convective aggregation is seen to be proportional to that, as well as to the domain-mean precipitation rate.

Then, in Section 4.4, I investigated the effect of the SST gradient on the environment of

the cloud cluster. I started with showing how, after zonal self-aggregation had taken place, the originally dry polar regions were moistened (Figure 4.7). I focused on hiSLAM-flatqobs and found that the meridional flow was directed polewards above the boundary layer, and that a substantial amount of atmospheric water is advected by that flow (see Figure 4.8). Analyzing the polar moisture budget (Figure 4.9) proved that advection was responsible for the moistening of the originally dry polar regions. I further investigated the properties of the mean circulation of hiSLAM-flatqobs (Figures 4.10, 4.11 and 4.12). It is shown how the shallow circulation crosses the pole and reaches the equatorial regions again, where its moisture is eventually recycled into the cloud clusters by the zonal low-level inflow. Moreover I found that the moist outflow only occurs in the meridional dimension, whereas zonally there is only inflow into the cloud cluster. The reasons are to be found in the zonally elongated shape of the cloud cluster and in the SST distribution.

In Section 4.5.2 I discussed the shallow circulation with respect to the findings of previous studies on convective self-aggregation. Then I presented properties of the circulation observed in hiSLAM-flatqobs that are reminiscent of atmospheric rivers and constitute plausible analogies to those.

I proceed with a summary of conclusions derived from the studies in Chapter 3 on *Convectively Generated Gravity Waves in high-resolution models of tropical dynamics* and Chapter 4 *Convective Aggregation in idealized simulations with SST gradients*, and give answers on the underlying research questions, posed in the Introduction Chapter 1.

5.1. Answering Research Questions on Convectively Generated Gravity Waves

1. **What are the spectral properties of gravity waves generated by a naturally evolving large-scale system of tropical convection?**

   The stratospheric zonal wavenumber spectra, derived in simulations of idealized tropical dynamics with explicit convection, hiSLAM and coSLAM-xc, show that convectively generated gravity waves contain significant wave variance at all scales ranging from their effective resolution up to scales >1000 km. In particular the spectrum of hiSLAM is flat and reveals the potential of convection in terms of the generation of gravity waves. The zonal momentum flux variance for scales shorter than ~ 250 km is enhanced. This we explain through the convection permitting resolution that allows the well-organized and intense deep convective clouds to mechanically generate gravity waves through a dynamical overshooting at cloud tops. Still we find that simulations of a realistic tropical atmosphere, NARVAL2 and ICSOM1, show steeper spectral slopes of zonal momentum flux $\sim k^{-1}$, and generally reproduce spectral slopes proposed by analytical gravity wave models. Further characteris-

tics are revealed in zonal wavenumber-frequency and vertical wavenumber spectra. The depth of latent heating reflects through the projection response on the vertical gravity wave modes and on the dominant vertical wavenumber.

2. **How are properties of CGGWs in numerical models affected by their numerical resolution, representation of convection and complexity of boundary conditions?**

   Naturally the numerical resolution of a model limits the gravity wave momentum flux to the scales that are resolved. From the comparison of hiSLAM and coSLAM-xc we find that the coarsening of the grid spacing from 2.5 to 20 km reduces the absolute momentum flux by a factor of 10 (see Table 3.3). While the two models' spectra are equivalent for the scales commonly resolved the feature of enhanced variance associated with stratospheric gravity waves at small scales is exclusive to hiSLAM (see Figure 3.10 (a)). Only the convection-permitting resolution of hiSLAM allows for oscillations at cloud tops (see Figure 3.6) and for enhanced gravity wave momentum flux above intense convection.

   We find that a convective parameterization inhibits gravity wave generation by convective clouds. This is found to be caused by a lack of variance in latent heating at small scales. Further, although deep convection and high clouds are present, the heating depth is generally diminished in coSLAM-pc. As a consequence no deep gravity wave mode exists and gravity wave variance is reduced for deeper vertical scales. Furthermore the mechanical generation of gravity waves appears to be inhibited. Thus the choice of a convective parameterization must be carefully considered when modeling wave-driven circulations in the middle atmosphere. For this reason we advise to turn off a parameterization of convection for numerical simulations of wave-driven circulations with grid spacings of 20km or less.

   In concerns of the complexity of boundary conditions we find that saturation of gravity wave spectra, as seen in a vertical wavenumber spectrum, is facilitated by the presence of a background flow. NARVAL2 and ICSOM1 also show the universal gravity wave spectrum is realized in realistic simulations of tropical dynamics, as all proposed spectral slopes of one-dimensional spectra of gravity wave properties are reproduced. However, also the idealized simulations, SLAMs, reproduce several properties of the universal spectrum. The deviations of hiSLAM from the universal spectrum - too flat spectral slopes - are attributed to the "near-field" character of the spectra, that are obtained directly over intense convection.

5.2. Answering Research Questions on Convective Aggregation in SST gradients

We presented convection-permitting RCE simulations on a spherical domain with specified SSTs, that are zonally symmetric, but that have a gradient in the meridional dimension. We find that convection aggregates as a result of both, the forcing of the SST gradient as well as through convective self-aggregation. On the one hand, we aimed at finding out about the controls of the meridional SST gradient on the zonal dimension, where convective self-aggregation may be expected to happen, as boundary conditions are zonally homogeneous. On the other hand, we wanted to reveal the effects of the cloud clusters, as emerging in our simulations with meridional SST gradients, on their environment.

1. **How does a meridional SST gradient affect the convective evolution and convective aggregation? In particular, how does it influence the zonal dimension, and does zonal convective self-aggregation occur?**
   We found that the stronger the meridional SST gradient the stronger is the meridional circulation, the more stable is the convergence line, and the longer it takes for zonal self-aggregation to occur. The evolution of zonal self-aggregation is rapid, once it started, and in this property insensitive to the steepness of the SST gradient. Also the strength of the zonal circulation required to initiate zonal self-aggregation we found to be unaffected by the SST gradient. Still the meridional gradient was found to have control over the zonal and meridional extent of the aggregated cluster, i.e. the steeper the meridional SST gradient the greater the zonal and the shorter the meridional extent. We discussed separate measures of the respective types of convective aggregation and showed how the processes affect one another, i.e. the zonal self-aggregation weakened the meridional SST-forced aggregation. This interdependence was found to base upon the intensification of the shallow meridional circulation, whose upper branch exports moisture away from the cloud cluster to the originally dry, non-convecting polar regions. This leads to research question # 2:

2. **How does the asymmetry of a cloud cluster affect the environment?**
   In experiments hiSLAM-qobs and hiSLAM-flatqobs the cloud clusters are zonally elongated. In hiSLAM-flatqobs we showed how the environment is affected through a complex shallow circulation. This circulation exports substantial amounts of moisture and in this way we find a strong effect of the SST gradient on the environment. The shallow circulation was found to weaken convective aggregation in terms of moisture variance and to moisten originally dry regions. In this way a shortcoming of traditional studies of convective self-aggregation, too dry non-convecting regions, is overcome. I have also shown that the circulation occurs only in the meridional dimension, at the elongated side of the clusters, and above cool SSTs. The latter

finding is in line with Coppin and Bony (2015); however we do not find shallow clouds associated with the circulation. Seeing an analogy of this circulation to atmospheric rivers seems reasonable. The "tapping" of moisture from the tropical moisture pool (Ralph et al., 2010) is simulated in an idealized modeling framework.

In a broader sense hiSLAM-qobs and hiSLAM-flatqobs constitute convection-permitting simulations of RCE in more complex boundary conditions. We forced aggregation through a simple change in the boundary conditions, and other scenarios may be thought of. We studied how (# 1) the SST gradient affects the convective evolution and (# 2) how the zonally elongated cloud cluster affects its environment. Such shape of a convective system appears more realistic than radial symmetry, like those seen in traditional RCE studies of convective self-aggregation, as it resembles equatorial convective systems associated with the Madden-Julian Oscillation, Kelvin Waves or the ITCZ. The simulations show that convective aggregation may, though still in fairly idealized conditions, develop complex moisture-carrying circulations and suggest that convective aggregation may serve as a prerequisite for tropical atmospheric rivers. Through this circulation the cloud cluster affects the large-scale environment, by transporting moisture to originally dry regions. Eventually, convective aggregation is more than just the formation of a moist bubble within a dry environment.

5.3. Implications and Outlook

In regards of convectively generated gravity waves the natural evolution of the experimental design, that we started with SLAMs of this study, would be to introduce a zonal circulation in the stratosphere. This would aim at mimicking a circulation as associated with the QBO. Two ways of experimental design appear sensible: first, the initialization with a zonal circulation in the stratosphere. The convection-permitting resolution of hiSLAM, along with the deep vertical domain and also the large horizontal scale, would constitute an ideal testbed for studying the effect of CGGWs on such circulation. The development of a QBO-like oscillation is then expected. Second, imposing and keeping the zonal stratospheric circulation fixed, would focus on the reverse mechanism: by that the effect of the QBO on the underlying convection may be elucidated.

The simulations of SLAMs with SST gradients have shown to constitute a sensible framework for studying convective aggregation in more complex conditions. In this study the underlying mechanisms that cause convective aggregation were not the focus of the study. Rather we took aggregation for granted, no matter whether it occurred meridionally as a result of the SST gradient's forcing or zonally from self-aggregation. With this approach we showed how breaking the strict symmetry of traditional RCE's boundary conditions, allowed for a more complex and realistic scenario. Such new models may come with the merits of solving old problems, like here the too dry non-convecting regions, and

of bringing new findings, such as here the relation of the shallow circulation to atmospheric rivers.

However, I see two issues of this work that might require greater attention: first, which effect does cloud cluster symmetry play in convective aggregation? We have seen that hiSLAM-qobs and hiSLAM-flatqobs developed complex circulations and it is clear that their zonally elongated shape is a important factor in this regard. On the other hand we have seen hiSLAM-27uni to achieve its highest degree of aggregation when forming a ring-like, radially symmetric structure, which it struggles to maintain. hiSLAM-warmpole however was forced to keep radial symmetry and a ring-like structure. I believe that with such simulations more light may be shed on the problem. Second, the role of water vapor in the shallow circulation and in atmospheric rivers is intriguing: is it just a passive tracer or may there be a mechanism by which water vapor controls the flow?

Finally I hope to inspire the community to work on developing new models, that are idealized and novel in their boundary conditions and complex in their phenomena. A new generation of convection-permitting models of realistic atmospheric conditions is about to bring an unprecedented degree of complexity with it, and their understanding may very likely benefit from new sets of idealized models, such as SLAM.

SLAM, in a configuration with uniform SSTs, is planned to participate in the RCEMIP (Wing et al., 2018).

A. On hiSLAM-warmpole

In hiSLAM-warmpole a warm SST anomaly is located at one of the poles. Figure A.1 shows the convective evolution by the water vapor path and the cloud condensate. The radially symmetric forcing of convection and convergence through the SST gradient leads to the formation of a radially symmetric cloud cluster. The cloud cluster very clearly shows an edge-intensification or a ring-like structure. This shape stays stable throughout the simulation. We note (not shown) that the cold pole, where SSTs reach $0°C$, is cooling strongly, with low level temperatures decreasing to $-30°C$.

A circular shape is the geometry with the shortest circumference at the greatest volume. For this hiSLAM-warmpole constitutes a geometrical limit of a cloud cluster to reach in a non-rotating environment. As we saw from other simulations the geometrical shape of the cluster may control the degree of aggregation, in terms of moisture variance. hiSLAM-qobs and hiSLAM-flatqobs reach their highest degree of aggregation when they form a continuous band of moisture and convection along the equator, which is a state of zonal symmetry. hiSLAM-27 is most aggregated when the cloud cluster forms a ring. For hiSLAM-warmpole the degree of aggregation, as the geometry of the cloud cluster, is very stable. Further we find that the domain-mean moisture content is lowest (see Figure 2.5). We may hypothesize that the high degree of symmetry weakens the shallow circulation and thus its effect in moisture export.
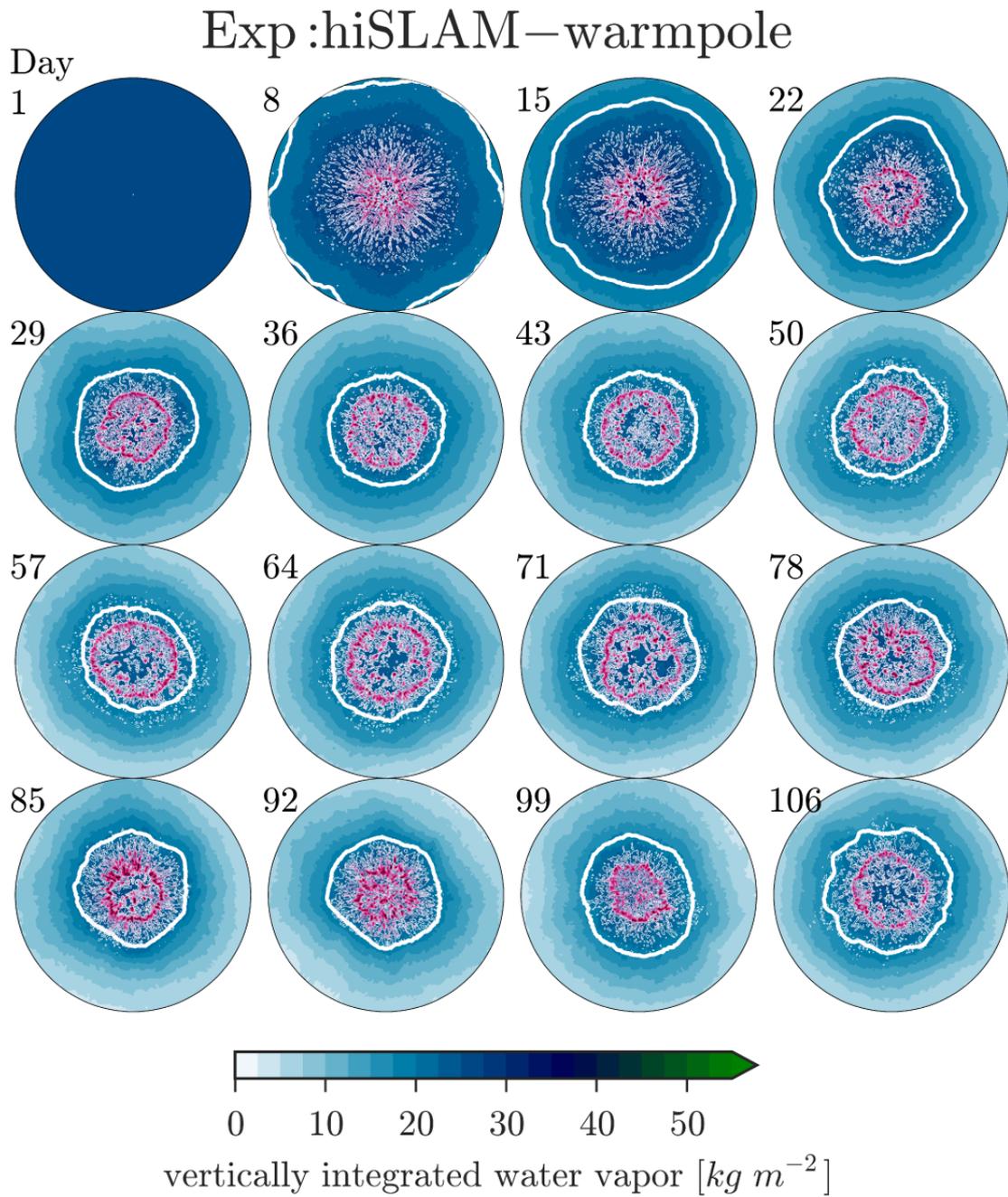
Figure A.1.: As Figure 4.2 but for experiment hiSLAM-warmpole. Shown is only the area above the warm pole, south of 45°S.

Bibliography

Alexander, M. and J. R. Holton, 1997: A model study of zonal forcing in the equatorial stratosphere by convectively induced gravity waves. *Journal of the atmospheric sciences*, **54**, 408–419.

Alexander, M., J. R. Holton, and D. R. Durran, 1995: The gravity wave response above deep convection in a squall line simulation. *Journal of the atmospheric sciences*, **52**, 2212–2226.

Angevine, W. M., H. Jiang, and T. Mauritsen, 2010: Performance of an eddy diffusivity–mass flux scheme for shallow cumulus boundary layers. *Monthly Weather Review*, **138**, 2895–2912.

Baldauf, M., A. Seifert, J. Förstner, D. Majewski, M. Raschendorfer, and T. Reinhardt, 2011: Operational convective-scale numerical weather prediction with the COSMO model: description and sensitivities. *Monthly Weather Review*, **139**, 3887–3905.

Baldwin, M., L. Gray, T. Dunkerton, K. Hamilton, P. Haynes, W. Randel, J. Holton, M. Alexander, I. Hirota, T. Horinouchi, et al., 2001: The quasi-biennial oscillation. *Reviews of Geophysics*, **39**, 179–229.

Bechtold, P., N. Semane, and S. Malardel: 2016, Convection and waves on small planets and the real Earth. *Parameterization of Atmospheric Convection: Volume 2: Current Issues and New Theories*, World Scientific, 59–73.

Becker, T., C. S. Bretherton, C. Hohenegger, and B. Stevens, 2018: Estimating bulk entrainment with unaggregated and aggregated convection. *Geophysical Research Letters*.

Bibliography

Becker, T., B. Stevens, and C. Hohenegger, 2017: Imprint of the convective parameterization and sea-surface temperature on large-scale convective self-aggregation. *Journal of Advances in Modeling Earth Systems*.

Beres, J. H., M. J. Alexander, and J. R. Holton, 2002: Effects of tropospheric wind shear on the spectrum of convectively generated gravity waves. *Journal of the atmospheric sciences*, **59**, 1805–1824.

Beres, J. H., R. R. Garcia, B. A. Boville, and F. Sassi, 2005: Implementation of a gravity wave source spectrum parameterization dependent on the properties of convection in the Whole Atmosphere Community Climate Model (WACCM). *Journal of Geophysical Research: Atmospheres*, **110**.

Blackburn, M. and B. J. Hoskins, 2013: Context and aims of the Aqua-Planet Experiment. *Journal of the Meteorological Society of Japan. Ser. II*, **91**, 1–15.

Bony, S., B. Stevens, D. Coppin, T. Becker, K. A. Reed, A. Voigt, and B. Medeiros, 2016: Thermodynamic control of anvil cloud amount. *Proceedings of the National Academy of Sciences*, **113**, 8927–8932.

Bony, S., B. Stevens, D. M. Frierson, C. Jakob, M. Kageyama, R. Pincus, T. G. Shepherd, S. C. Sherwood, A. P. Siebesma, A. H. Sobel, et al., 2015: Clouds, circulation and climate sensitivity. *Nature Geoscience*, **8**, 261.

Brayshaw, D. J., B. Hoskins, and M. Blackburn, 2008: The storm-track response to idealized SST perturbations in an aquaplanet GCM. *Journal of the Atmospheric Sciences*, **65**, 2842–2860.

Bretherton, C. S., P. N. Blossey, and M. Khairoutdinov, 2005: An energy-balance analysis of deep convective self-aggregation above uniform SST. *Journal of the atmospheric sciences*, **62**, 4273–4292.

Bretherton, C. S. and P. K. Smolarkiewicz, 1989: Gravity waves, compensating subsidence and detrainment around cumulus clouds. *Journal of the atmospheric sciences*, **46**, 740–759.

Clark, L., D. Hall, and L. Coen, 1996: Source code documentation for the Clark-Hall Cloud-scale Model Code Version G3CH01.

Clark, T. L., T. Hauf, and J. P. Kuettner, 1986: Convectively forced internal gravity waves: Results from two-dimensional numerical experiments. *Quarterly Journal of the Royal Meteorological Society*, **112**, 899–925.

Coppin, D. and S. Bony, 2015: Physical mechanisms controlling the initiation of convective self-aggregation in a General Circulation Model. *Journal of Advances in Modeling Earth Systems*, **7**, 2060–2078.

Dewan, E. and R. Good, 1986: Saturation and the "universal" spectrum for vertical profiles of horizontal scalar winds in the atmosphere. *Journal of Geophysical Research: Atmospheres*, **91**, 2742–2748.

Dipankar, A., B. Stevens, R. Heinze, C. Moseley, G. Zängl, M. Giorgetta, and S. Brdar, 2015: Large eddy simulation using the general circulation model ICON. *Journal of Advances in Modeling Earth Systems*, **7**, 963–986.

Eiras-Barca, J., A. M. Ramos, J. G. Pinto, R. M. Trigo, M. L. Liberato, and G. Miguez-Macho, 2018: The concurrence of atmospheric rivers and explosive cyclogenesis in the North Atlantic and North Pacific basins. *Earth System Dynamics*, **9**, 91–102.

Emanuel, K. A., 1986: An air-sea interaction theory for tropical cyclones. Part I: Steady-state maintenance. *Journal of the Atmospheric Sciences*, **43**, 585–605.

Emanuel, K. A., J. David Neelin, and C. S. Bretherton, 1994: On large-scale circulations in convecting atmospheres. *Quarterly Journal of the Royal Meteorological Society*, **120**, 1111–1143.

Etling, D. and R. Brown, 1993: Roll vortices in the planetary boundary layer: A review. *Boundary-Layer Meteorology*, **65**, 215–248.

Fovell, R., D. Durran, and J. Holton, 1992: Numerical simulations of convectively generated stratospheric gravity waves. *Journal of the atmospheric sciences*, **49**, 1427–1442.

Fritts, D. C. and M. J. Alexander, 2003: Gravity wave dynamics and effects in the middle atmosphere. *Reviews of geophysics*, **41**.

Gage, K. and G. Nastrom, 1985: On the spectrum of atmospheric velocity fluctuations seen by MST/ST radar and their interpretation. *Radio Science*, **20**, 1339–1347.

— 1986a: Spectrum of atmospheric vertical displacements and spectrum of conservative scalar passive additives due to quasi-horizontal atmospheric motions. *Journal of Geophysical Research: Atmospheres*, **91**, 13211–13216.

— 1986b: Theoretical interpretation of atmospheric wavenumber spectra of wind and temperature observed by commercial aircraft during GASP. *Journal of the atmospheric sciences*, **43**, 729–740.

Gardner, C. S., C. A. Hostetler, and S. J. Franke, 1993: Gravity wave models for the horizontal wave number spectra of atmospheric velocity and density fluctuations. *Journal of Geophysical Research: Atmospheres*, **98**, 1035–1049.

Garrett, C. and W. Munk, 1972: Space-time scales of internal waves. *Geophysical & Astrophysical Fluid Dynamics*, **3**, 225–264.

— 1975: Space-time scales of internal waves: A progress report. *Journal of Geophysical Research*, **80**, 291–297.

Gassmann, A. and H.-J. Herzog, 2008: Towards a consistent numerical compressible non-hydrostatic model using generalized Hamiltonian tools. *Quarterly Journal of the Royal Meteorological Society*, **134**, 1597–1613.

Giorgetta, M. et al., 2018: ICON-A, the atmospheric component of the ICON Earth System Model. Part I: Model Description .

Giorgetta, M. A., E. Roeckner, T. Mauritsen, J. Bader, T. Crueger, M. Esch, S. Rast, L. Kornblueh, H. Schmidt, S. Kinne, et al., 2013: The atmospheric general circulation model ECHAM6-model description.

Grabowski, W. W., 2003: MJO-like coherent structures: Sensitivity simulations using the cloud-resolving convection parameterization (CRCP). *Journal of the Atmospheric Sciences*, **60**, 847–864.

Guan, B. and D. E. Waliser, 2015: Detection of atmospheric rivers: Evaluation and application of an algorithm for global studies. *Journal of Geophysical Research: Atmospheres*, **120**, 12514–12535.

Hayashi, Y., 1971: A generalized method of resolving disturbances into progressive and retrogressive waves by space Fourier and time cross-spectral analyses. *J. Meteor. Soc. Japan*, **49**, 125–128.

Held, I. M., R. S. Hemler, and V. Ramaswamy, 1993: Radiative-convective equilibrium with explicit two-dimensional moist convection. *Journal of the atmospheric sciences*, **50**, 3909–3927.

Held, I. M., M. Zhao, and B. Wyman, 2007: Dynamic radiative–convective equilibria using GCM column physics. *Journal of the atmospheric sciences*, **64**, 228–238.

Hines, C. O., 1991: The saturation of gravity waves in the middle atmosphere. Part II: Development of Doppler-spread theory. *Journal of the Atmospheric Sciences*, **48**, 1361–1379.

Hohenegger, C. and B. Stevens, 2016: Coupled radiative convective equilibrium simulations with explicit and parameterized convection. *Journal of Advances in Modeling Earth Systems*, **8**, 1468–1482.

Holloway, C. E. and S. J. Woolnough, 2016: The sensitivity of convective aggregation to diabatic processes in idealized radiative-convective equilibrium simulations. *Journal of Advances in Modeling Earth Systems*.

Holt, L. A., M. J. Alexander, L. Coy, A. Molod, W. Putman, and S. Pawson, 2016: Tropical waves and the quasi-biennial oscillation in a 7-km global climate simulation. *Journal of the Atmospheric Sciences*, **73**, 3771–3783.

Holton, J., J. Beres, and X. Zhou, 2002: On the vertical scale of gravity waves excited by localized thermal forcing. *Journal of the atmospheric sciences*, **59**, 2019–2023.

Holton, J. R., 1973: On the frequency distribution of atmospheric Kelvin waves. *Journal of the Atmospheric Sciences*, **30**, 499–501.

Holton, J. R. and G. J. Hakim, 2012: *An introduction to dynamic meteorology*, volume 88. Academic press.

Houze Jr, R. A., 1977: Structure and dynamics of a tropical squall–line system. *Monthly Weather Review*, **105**, 1540–1567.

Jablonowski, C. and D. L. Williamson, 2006: A baroclinic instability test case for atmospheric model dynamical cores. *Quarterly Journal of the Royal Meteorological Society*, **132**, 2943–2975.

Jeevanjee, N. and D. M. Romps, 2013: Convective self-aggregation, cold pools, and domain size. *Geophysical Research Letters*, **40**, 994–998.

Johnson, R. H., T. M. Rickenbach, S. A. Rutledge, P. E. Ciesielski, and W. H. Schubert, 1999: Trimodal characteristics of tropical convection. *Journal of climate*, **12**, 2397–2418.

Khairoutdinov, M. F., S. K. Krueger, C.-H. Moeng, P. A. Bogenschutz, and D. A. Randall, 2009: Large-Eddy Simulation of Maritime Deep Tropical Convection. *Journal of Advances in Modeling Earth Systems*, **1**.

Kiladis, G. N., M. C. Wheeler, P. T. Haertel, K. H. Straub, and P. E. Roundy, 2009: Convectively coupled equatorial waves. *Reviews of Geophysics*, **47**.

Klemp, J., J. Dudhia, and A. Hassiotis, 2008: An upper gravity-wave absorbing layer for NWP applications. *Monthly Weather Review*, **136**, 3987–4004.

Klocke, D., M. Brueck, C. Hohenegger, and B. Stevens, 2017: Rediscovery of the doldrums in storm-resolving simulations over the tropical Atlantic. *Nature Geoscience*, **10**, 891.

Koshyk, J. N. and K. Hamilton, 2001: The horizontal kinetic energy spectrum and spectral budget simulated by a high-resolution troposphere–stratosphere–mesosphere GCM. *Journal of the atmospheric sciences*, **58**, 329–348.

Kraichnan, R. H., 1967: Inertial ranges in two-dimensional turbulence. *The Physics of Fluids*, **10**, 1417–1423.

Lane, T. P. and J. C. Knievel, 2005: Some effects of model resolution on simulated gravity waves generated by deep, mesoscale convection. *Journal of the atmospheric sciences*, **62**, 3408–3419.

Lane, T. P. and M. W. Moncrieff, 2008: Stratospheric gravity waves generated by multi-scale tropical convection. *Journal of the Atmospheric Sciences*, **65**, 2598–2614.

Lane, T. P., M. J. Reeder, and T. L. Clark, 2001: Numerical modeling of gravity wave generation by deep tropical convection. *Journal of the atmospheric sciences*, **58**, 1249–1274.

Lavers, D. A., G. Villarini, R. P. Allan, E. F. Wood, and A. J. Wade, 2012: The detection of atmospheric rivers in atmospheric reanalyses and their links to British winter floods and the large-scale climatic circulation. *Journal of Geophysical Research: Atmospheres*, **117**.

Leuenberger, D., M. Koller, O. Fuhrer, and C. Schär, 2010: A generalization of the SLEVE vertical coordinate. *Monthly weather review*, **138**, 3683–3689.

Lin, J.-L., M.-I. Lee, D. Kim, I.-S. Kang, and D. M. Frierson, 2008: The impacts of convective parameterization and moisture triggering on AGCM-simulated convectively coupled equatorial waves. *Journal of Climate*, **21**, 883–909.

Liu, H.-L., J. McInerney, S. Santos, P. Lauritzen, M. Taylor, and N. Pedatella, 2014: Gravity waves simulated by high-resolution Whole Atmosphere Community Climate Model. *Geophysical Research Letters*, **41**, 9106–9112.

Lohmann, U. and E. Roeckner, 1996: Design and performance of a new cloud microphysics scheme developed for the ECHAM general circulation model. *Climate Dynamics*, **12**, 557–572.

Lu, J., G. Chen, and D. M. Frierson, 2010: The position of the midlatitude storm track and eddy-driven westerlies in aquaplanet AGCMs. *Journal of the Atmospheric Sciences*, **67**, 3984–4000.

Manabe, S. and R. F. Strickler, 1964: Thermal equilibrium of the atmosphere with a convective adjustment. *Journal of the Atmospheric Sciences*, **21**, 361–385.

Manabe, S. and R. T. Wetherald, 1967: Thermal equilibrium of the atmosphere with a given distribution of relative humidity. *Journal of the Atmospheric Sciences*, **24**, 241–259.

Mapes, B., 2016: Gregarious convection and radiative feedbacks in idealized worlds. *Journal of Advances in Modeling Earth Systems*, **8**, 1029–1033.

Mapes, B. E., 1993: Gregarious tropical convection. *Journal of the atmospheric sciences*, **50**, 2026–2037.

Mauritsen, T. and B. Stevens, 2015: Missing iris effect as a possible cause of muted hydrological change and high climate sensitivity in models. *Nature Geoscience*, **8**, 346.

Mauritsen, T., G. Svensson, S. S. Zilitinkevich, I. Esau, L. Enger, and B. Grisogono, 2007: A total turbulent energy closure model for neutrally and stably stratified atmospheric boundary layers. *Journal of the Atmospheric Sciences*, **64**, 4113–4126.

McLandress, C., M. J. Alexander, and D. L. Wu, 2000: Microwave Limb Sounder observations of gravity waves in the stratosphere: A climatology and interpretation. *Journal of Geophysical Research: Atmospheres*, **105**, 11947–11967.

Mellor, G. L. and T. Yamada, 1982: Development of a turbulence closure model for geophysical fluid problems. *Reviews of Geophysics*, **20**, 851–875.

Montgomery, M. T., J. Persing, and R. K. Smith, 2015: Putting to rest WISHE-ful misconceptions for tropical cyclone intensification. *Journal of Advances in Modeling Earth Systems*, **7**, 92–109.

Muller, C. and S. Bony, 2015: What favors convective aggregation and why? *Geophysical Research Letters*, **42**, 5626–5634.

Muller, C. J. and I. M. Held, 2012: Detailed Investigation of the Self-Aggregation of Convection in Cloud-Resolving Simulations. *Journal of the Atmospheric Sciences*, **69**, 2551–2565, doi:10.1175/JAS-D-11-0257.1.
URL http://dx.doi.org/10.1175/JAS-D-11-0257.1

Nakanishi, M. and H. Niino, 2006: An improved Mellor–Yamada level-3 model: Its numerical stability and application to a regional prediction of advection fog. *Boundary-Layer Meteorology*, **119**, 397–407.

Nastrom, G., K. Gage, and W. Jasperson, 1984: Kinetic energy spectrum of large-and mesoscale atmospheric processes. *Nature*, **310**, 36–38.

Nasuno, T., H. Tomita, S. Iga, H. Miura, and M. Satoh, 2007: Multiscale organization of convection simulated with explicit cloud processes on an aquaplanet. *Journal of the atmospheric sciences*, **64**, 1902–1921.

Neale, R. B. and B. Hoskins, 2000a: A standard test for AGCMs including their physical parametrizations. II: Results for the Met Office Model. *Atmospheric Science Letters*, **1**, 108–114.

Neale, R. B. and B. J. Hoskins, 2000b: A standard test for AGCMs including their physical parametrizations: I: The proposal. *Atmospheric Science Letters*, **1**, 101–107.

Neiman, P. J., F. M. Ralph, G. A. Wick, J. D. Lundquist, and M. D. Dettinger, 2008: Meteorological characteristics and overland precipitation impacts of atmospheric rivers affecting the West Coast of North America based on eight years of SSM/I satellite observations. *Journal of Hydrometeorology*, **9**, 22–47.

Newell, R. E., N. E. Newell, Y. Zhu, and C. Scott, 1992: Tropospheric rivers?–A pilot study. *Geophysical research letters*, **19**, 2401–2404.

Noda, A. T., K. Oouchi, M. Satoh, H. Tomita, S.-i. Iga, and Y. Tsushima, 2010: Importance of the subgrid-scale turbulent moist process: Cloud distribution in global cloud-resolving simulations. *Atmospheric Research*, **96**, 208–217.

Nordeng, T. E., 1994: Extended versions of the convective parameterization scheme at ECMWF and their impact on the mean and transient activity of the model in the tropics. *Tech. Rep. ECMWF*, **206**.

Piani, C. and D. Durran, 2001: A numerical study of stratospheric gravity waves triggered by squall lines observed during the TOGA COARE and COPT-81 experiments. *Journal of the atmospheric sciences*, **58**, 3702–3723.

Piani, C., D. Durran, M. Alexander, and J. Holton, 2000: A numerical study of three-dimensional gravity waves triggered by deep tropical convection and their role in the dynamics of the QBO. *Journal of the atmospheric sciences*, **57**, 3689–3702.

Pincus, R. and B. Stevens, 2013: Paths to accuracy for radiation parameterizations in atmospheric models. *Journal of Advances in Modeling Earth Systems*, **5**, 225–233.

Pithan, F., W. Angevine, and T. Mauritsen, 2015: Improving a global model from the boundary layer: Total turbulent energy and the neutral limit Prandtl number. *Journal of Advances in Modeling Earth Systems*, **7**, 791–805.

Posselt, D. J., S. v. d. Heever, G. Stephens, and M. R. Igel, 2012: Changes in the interaction between tropical convection, radiation, and the large-scale circulation in a warming environment. *Journal of Climate*, **25**, 557–571.

Prein, A. F., W. Langhans, G. Fosser, A. Ferrone, N. Ban, K. Goergen, M. Keller, M. Tölle, O. Gutjahr, F. Feser, et al., 2015: A review on regional convection-permitting climate modeling: Demonstrations, prospects, and challenges. *Reviews of geophysics*, **53**, 323–361.

Preusse, P., S. D. Eckermann, and M. Ern, 2008: Transparency of the atmosphere to short horizontal wavelength gravity waves. *Journal of Geophysical Research: Atmospheres*, **113**.

Ralph, F. M., P. J. Neiman, G. N. Kiladis, K. Weickmann, and D. W. Reynolds, 2010: A multi-scale observational case study of a Pacific atmospheric river exhibiting tropical-extratropical connections and a mesoscale frontal wave. *Monthly Weather Review*.

Ralph, F. M., P. J. Neiman, and R. Rotunno, 2005: Dropsonde observations in low-level jets over the northeastern Pacific Ocean from CALJET-1998 and PACJET-2001: Mean vertical-profile and atmospheric-river characteristics. *Monthly weather review*, **133**, 889–910.

Ralph, F. M., P. J. Neiman, and G. A. Wick, 2004: Satellite and CALJET aircraft observations of atmospheric rivers over the eastern North Pacific Ocean during the winter of 1997/98. *Monthly Weather Review*, **132**, 1721–1745.

Ramanathan, V. and J. Coakley, 1978: Climate modeling through radiative-convective models. *Reviews of geophysics*, **16**, 465–489.

Reed, K. A. and B. Medeiros, 2016: A reduced complexity framework to bridge the gap between AGCMs and cloud-resolving models. *Geophysical Research Letters*, **43**, 860–866.

Richter, J. H., F. Sassi, and R. R. Garcia, 2010: Toward a physically based gravity wave source parameterization in a general circulation model. *Journal of the Atmospheric Sciences*, **67**, 136–156.

Rotunno, R., J. B. Klemp, and M. L. Weisman, 1988: A theory for strong, long-lived squall lines. *Journal of the Atmospheric Sciences*, **45**, 463–485.

Salby, M. L. and R. R. Garcia, 1987: Transient response to localized episodic heating in the tropics. Part I: Excitation and short-time near-field behavior. *Journal of the atmospheric sciences*, **44**, 458–498.

Sato, K., 1992: Vertical wind disturbances in the afternoon of mid-summer revealed by the MU radar. *Geophysical research letters*, **19**, 1943–1946.

Sato, K. and T. J. Dunkerton, 1997: Estimates of momentum flux associated with equatorial Kelvin and gravity waves. *Journal of Geophysical Research: Atmospheres*, **102**, 26247–26261.

Sato, K. and M. Yamada, 1994: Vertical structure of atmospheric gravity waves revealed by the wavelet analysis. *Journal of Geophysical Research: Atmospheres*, **99**, 20623–20631.

Satoh, M., T. Matsuno, H. Tomita, H. Miura, T. Nasuno, and S.-i. Iga, 2008: Nonhydrostatic icosahedral atmospheric model (NICAM) for global cloud resolving simulations. *Journal of Computational Physics*, **227**, 3486–3514.

Satoh, M., H. Tomita, H. Yashiro, H. Miura, C. Kodama, T. Seiki, A. T. Noda, Y. Yamada, D. Goto, M. Sawada, et al., 2014: The non-hydrostatic icosahedral atmospheric model: Description and development. *Progress in Earth and Planetary Science*, **1**, 18.

Smith, S. A., D. C. Fritts, and T. E. VanZandt, 1985: Comparison of mesospheric wind spectra with a gravity wave model. *Radio Science*, **20**, 1331–1338.

Smith, S. A., D. C. Fritts, and T. E. Vanzandt, 1987: Evidence for a saturated spectrum of atmospheric gravity waves. *Journal of the Atmospheric Sciences*, **44**, 1404–1410.

Sobel, A. H. and C. S. Bretherton, 2000: Modeling tropical precipitation in a single column. *Journal of Climate*, **13**, 4378–4392.

Sobel, A. H., J. Nilsson, and L. M. Polvani, 2001: The weak temperature gradient approximation and balanced tropical moisture waves. *Journal of the atmospheric sciences*, **58**, 3650–3665.

Song, I.-S., H.-Y. Chun, and T. P. Lane, 2003: Generation mechanisms of convectively forced internal gravity waves and their propagation to the stratosphere. *Journal of the atmospheric sciences*, **60**, 1960–1980.

Stachnik, J. P. and C. Schumacher, 2011: A comparison of the Hadley circulation in modern reanalyses. *Journal of Geophysical Research: Atmospheres*, **116**.

Staniforth, A. and J. Thuburn, 2012: Horizontal grids for global weather and climate prediction models: a review. *Quarterly Journal of the Royal Meteorological Society*, **138**, 1–26.

Stephan, C. and M. J. Alexander, 2014: Summer season squall-line simulations: Sensitivity of gravity waves to physics parameterization and implications for their Parameterization in Global Climate Models. *Journal of the Atmospheric Sciences*, **71**, 3376–3391.

Stevens, B., 2005: Atmospheric moist convection. *Annu. Rev. Earth Planet. Sci.*, **33**, 605–643.

Stevens, B., M. Giorgetta, M. Esch, T. Mauritsen, T. Crueger, S. Rast, M. Salzmann, H. Schmidt, J. Bader, K. Block, et al., 2013: Atmospheric component of the MPI-M Earth System Model: ECHAM6. *Journal of Advances in Modeling Earth Systems*, **5**, 146–172.

Tiedtke, M., 1989: A comprehensive mass flux scheme for cumulus parameterization in large-scale models. *Monthly Weather Review*, **117**, 1779–1800.

Tobin, I., S. Bony, and R. Roca, 2012: Observational evidence for relationships between the degree of aggregation of deep convection, water vapor, surface fluxes, and radiation. *Journal of Climate*, **25**, 6885–6904.

Tomita, H., 2008: New microphysical schemes with five and six categories by diagnostic generation of cloud ice. *Journal of the Meteorological Society of Japan. Ser. II*, **86**, 121–142.

Tomita, H., H. Miura, S. Iga, T. Nasuno, and M. Satoh, 2005: A global cloud-resolving simulation: Preliminary results from an aqua planet experiment. *Geophysical Research Letters*, **32**.

Tompkins, A. M., 2001: Organization of tropical convection in low vertical wind shears: The role of water vapor. *Journal of the atmospheric sciences*, **58**, 529–545.

Tompkins, A. M. and G. C. Craig, 1998: Radiative–convective equilibrium in a three-dimensional cloud-ensemble model. *Quarterly Journal of the Royal Meteorological Society*, **124**, 2073–2097.

Tompkins, A. M. and A. G. Semie, 2017: Organization of tropical convection in low vertical wind shears: role of updraft entrainment. *Journal of Advances in Modeling Earth Systems*, **9**, 1046–1068.

Tsuda, T., T. Inoue, S. Kato, S. Fukao, D. Fritts, and T. VanZandt, 1989: MST radar observations of a saturated gravity wave spectrum. *Journal of the Atmospheric Sciences*, **46**, 2440–2447.

Tsuda, T., Y. Murayama, H. Wiryosumarto, S. W. B. Harijono, and S. Kato, 1994: Radiosonde observations of equatorial atmosphere dynamics over Indonesia: 2. Characteristics of gravity waves. *Journal of Geophysical Research: Atmospheres*, **99**, 10507–10516.

Waliser, D. E., M. W. Moncrieff, D. Burridge, A. H. Fink, D. Gochis, B. Goswami, B. Guan, P. Harr, J. Heming, H.-H. Hsu, et al., 2012: The "year" of tropical convection (May 2008–April 2010): Climate variability and weather highlights. *Bulletin of the American Meteorological Society*, **93**, 1189–1218.

Bibliography

Wan, H., M. A. Giorgetta, G. Zängl, M. Restelli, D. Majewski, L. Bonaventura, K. Fröhlich, D. Reinert, P. Rípodas, L. Kornblueh, et al., 2013: The ICON-1.2 hydrostatic atmospheric dynamical core on triangular grids, Part I: formulation and performance of the baseline version. *Geoscientific Model Development*, **6**, 735–763.

Watanabe, S., K. Sato, Y. Kawatani, and M. Takahashi, 2015: Vertical resolution dependence of gravity wave momentum flux simulated by an atmospheric general circulation model. *Geoscientific Model Development*, **8**, 1637–1644.

Weinstock, J., 1985a: On the theory of temperature spectra in a stably stratified fluid. *Journal of physical oceanography*, **15**, 475–477.

— 1985b: Theoretical gravity wave spectrum in the atmosphere: Strong and weak wave interactions. *Radio Science*, **20**, 1295–1300.

Wing, A. A., S. J. Camargo, and A. H. Sobel, 2016: Role of radiative–convective feedbacks in spontaneous tropical cyclogenesis in idealized numerical simulations. *Journal of the Atmospheric Sciences*, **73**, 2633–2642.

Wing, A. A. and T. W. Cronin, 2016: Self-aggregation of convection in long channel geometry. *Quarterly Journal of the Royal Meteorological Society*, **142**, 1–15.

Wing, A. A. and K. A. Emanuel, 2014: Physical mechanisms controlling self-aggregation of convection in idealized numerical modeling simulations. *J. Adv. Model. Earth Syst*, **6**, 59–74.

Wing, A. A., K. A. Reed, M. Satoh, B. Stevens, S. Bony, and T. Ohno, 2018: Radiative–convective equilibrium model intercomparison project. *Geoscientific Model Development*, **11**, 793.

Zängl, G., D. Reinert, P. Rípodas, and M. Baldauf, 2015: The ICON (ICOsahedral Non-hydrostatic) modelling framework of DWD and MPI-M: Description of the non-hydrostatic dynamical core. *Quarterly Journal of the Royal Meteorological Society*, **141**, 563–579.

Zhang, C., 2005: Madden-julian oscillation. *Reviews of Geophysics*, **43**.

Zhang, S. D., C. M. Huang, K. M. Huang, Y. Gong, G. Chen, Q. Gan, and Y. H. Zhang, 2017a: Latitudinal and Seasonal Variations of Vertical Wave Number Spectra of Three-Dimensional Winds Revealed by Radiosonde Observations. *Journal of Geophysical Research: Atmospheres*.

Zhang, S. D., C. M. Huang, K. M. Huang, Y. H. Zhang, Y. Gong, and Q. Gan: 2017b, Vertical wavenumber spectra of three-dimensional winds revealed by radiosonde observations at midlatitude. *Annales Geophysicae*, Copernicus GmbH, volume 35, 107.

Zhao, J., X. Chu, C. Chen, X. Lu, W. Fong, Z. Yu, R. Michael Jones, B. R. Roberts, and A. Dörnbrack, 2017: Lidar observations of stratospheric gravity waves from 2011 to 2015 at McMurdo (77.84 S, 166.69 E), Antarctica: 1. Vertical wavelengths, periods, and frequency and vertical wave number spectra. *Journal of Geophysical Research: Atmospheres*, **122**, 5041–5062.

Zhu, Y. and R. E. Newell, 1998: A proposed algorithm for moisture fluxes from atmospheric rivers. *Monthly weather review*, **126**, 725–735.

CHAPTER

ACKNOWLEDGMENTS

I would like to acknowledge my main supervisor Elisa Manzini, for her constant support and scientific advice, that were essential in realizing this dissertation. I have also benefitted a lot from scientific discussions and advice of Marco Giorgetta. Further I feel very lucky for working with Cathy Hohenegger on the second part of this thesis. I would also like to acknowledge Prof. Stefan Bühler, in his role as my advisory panel's chair, for being very supportive and encouraging.

The administrative support and neutral advice provided by the people running the IMPRS-ESM, Antje Weitz, Connie Kampmann and Michi Böhm, was just great. I would like to acknowledge the PhD school in general for allowing a PhD candidate to concentrate on research, in a sensible educational framework, and within a truly diverse community.

During my research stay at the University of Tokyo I was hosted by Prof. Kaoru Sato. I would like to express my deep gratitude for her scientific support in form of discussions and teaching, and for inviting me to the group retreat in such a classic japanese environment. Of her students, I would like to thank Ryosuke-san, Arata-san and Yuji-san in particular. Precious support, in form of model output and discussions, I received of Tomoe Nasuno. Further I would like to thank Chihiro Kodama for discussions and for giving me the chance to introduce my work in a seminar at JAMSTEC institute. The Japanese culture of research is one of diligence, ambition, commitment and discipline, and this experience was inspiring and is truly precious to me.

I am thankful for learning the dynamics of tropical meteorology and for being encouraged to pursue research during my time as a MSc students in the group of Roger Smith. Now I am equally thankful for the perspective on tropical meteorology, in particular its

thermodynamics, that I was taught at MPI. Bjorn Stevens, as a visionary teacher and scientist, and friendly leader, thank you for the inspiration.

Dear Tobi, fellow group member, thank you for all the lunch times and weather briefings, for co-processing life and the meta-science!

Thanks Sally for sharing an office and literally backing me up! Thanks to my research group, as well as the whole atmosphere department, basically the whole institute, for generating such an inspired and friendly environment.

To me climbing always meant great physical activity and mental distraction. Anyone I shared climbing or slacklining with, my life's healthy and balancing activities, so thankful, most notably Beniamino, Thomas, Otso, Mona, Martin, Eason, Sebastian Milinski and many others. Thanks Katherine and Vimal for roadtrippin'! Thanks to all of my friends for being friends and for the continuous support!

For their scientific and technical support, and for proof-reading of parts of this thesis, I would like thank Sebastian Rast, Daniel Klocke, Pavan Siligam, Suvarchal Kumar, Tobias Becker and Julia Windmiller. As much as for that, as for the joyful interaction and for the coffee culture, I am grateful for pursuing this PhD alongside Guido Cioni.

Thanks to Haus Jona and its leader Peter Bachmeier, for having me as a bake caker and socializer among the homeless, and in general for balancing my pursuit of a scientific career with altruistic social work. I've received as much as I was giving.

Thanks a lot also to Amir and Ali of Bistro Arrabiata for the food and for the tea!

Vielen Dank auch an Peter Kraus für die physikalische Früherziehung!

Zu guter letzt, lieber Vater, liebe Mama, liebe Oma, liebe No, ich danke euch so sehr für eure bedingungslose Unterstützung, für den Rückhalt und die Freiheit die ihr mir gewährt, für eure Liebe und unser Zuhause.

Trivia

Dear Hamburg, what a mountain of a city you are! Coming from Bavaria, you made me realize the bavarian in my character, which expresses in more or less subtle ways. You enriched my life with cultural diversity, most of all with your vivid and alternative music scene. Getting to know your international community, as well as the one at scientific conferences, at MPI and within the IMPRS, showed me how a cultural background may be reflected in a person's character, but more importantly proved, that every human being is an individual in the very first place.

Dear atmosphere, dear weather, dear climate and climate change, you show yourselves to us scientists in fascinating phenomena, for which we adore you! You challenge us for deeper understanding, and mostly you puzzle us. We only can grasp your most basic principles, in simplified models and your real complexity remains obscure, and this we shall accept. You also frighten and torture us: this summer's heat wave, a climatic extreme, was a demanding environment to write this all up. I proved my perseverance, and still

this summer leaves me stunned through its credible display of the heaviness of climate change's future impact. In this sense, have we not yet learned enough and aren't the lessons learned too clear? Anyway, dear scientific community, be encouraged to pursue and to provide understanding. Society is in need of our expertise and interpretations, and of people of courage to speak up with credibility against mankind's misleading powers and leaders, who are putting it all at risk.

Dear newly started PhD student picking up this dissertation, dear former self! What it means to do a PhD is formally to prove your ability to conduct research independently. As such it is your emanzipation as a researcher. What goes along with this is a three-year long dedication to a certain subject. It is tried to phrase the goal and the problem already in the beginning, and this is not trivial but crucial. As of this I would like to encourage you to concentrate on understanding the problem and to question your understanding of it in as many ways as possible. Alternatively this understanding may slowly evolve as the methods and models are developed, but like that much time and frustration might be wasted. On another side, the mentality of a student is challenged. The objective is to write a dissertation until a certain point in time. At times it might seem impossible to produce the required amount of scientific material and one is challenged to keep going and believing. And then, without realizing it, the material is there, and again one is asked to understand it in order to distill the science out of it. And ultimately, it comes the time, when material and understanding are there, that it is about putting it all together. In that sense: first, understand the problem, second develop your methods and obtain results, third, overcome frustration and keep going, fourth, understand what you've been doing, fifth, make it real. Eventually you'll hopefully see, you tried really hard, despite not knowing of the outcome, and it happenend and made some great sense.

Dear Malik, dear Dr. Disko, dear Comicbüro and friends from St. Georg, you were ever an uplifting distraction, at times pushing too high and too far, but still, having been socialized in a local supporting and so tolerant community means a lot to me. Thanks to all of you!

Dear demons of mine, you and me, we tried all we could, but me and my angels, we still made it happen. "Es geht immer ums vollenden." (Der Nino aus Wien)

Dear future self, you now live in the moutains, in a hut close to the forest, remote, isolated and off grid? You made it? You happy now? Weren't you happy back in the days of your PhD? "But what does happiness even mean?" (Jeffrey Lewis) We're all just somethin', let's just try to be a good somethin'. [John Frusciante]

Aus dieser Dissertation hervorgegangene Vorveröffentlichungen
List of Publications

Müller S. K., Manzini E., Giorgetta M., Nasuno T. and Sato K. (2018): Convectively Generated Gravity Waves in High-Resolution Models of Tropical Dynamics. J. Adv. Model. Earth. Syst., in review.

Eidesstattliche Versicherung
Declaration on oath

Hiermit versichere ich an Eides statt, dass ich die vorliegende Dissertation mit dem Titel: "Convectively Generated Gravity Waves and Convective Aggregation in Numerical Models of Tropical Dynamics" selbstständig verfasst und keine anderen als die angegebenen Hilfsmittel insbesondere keine im Quellenverzeichnis nicht benannten Internet-Quellen benutzt habe. Alle Stellen, die wörtlich oder sinngemäßaus Veröffentlichungen entnommen wurden, sind als solche kenntlich gemacht. Ich versichere weiterhin, dass ich die Dissertation oder Teile davon vorher weder im In- noch im Ausland in einem anderen Prüfungsverfahren eingereicht habe und die eingereichte schriftliche Fassung der auf dem elektronischen Speichermedium entspricht.

I hereby declare, on oath, that I have written the present dissertation by myself and have not used other than the acknowledged resources and aids.

Hamburg, den 14. August 2018

Sebastian K. Müller